Cover Page

Universiteit Leiden

The handle http://hdl.handle.net/1887/18979 holds various files of this Leiden University dissertation.

Author: Usenko, Oleksandr
Title: Development and testing of the gravitational wave antenna MiniGRAIL in its full-featured configuration
Date: 2012-05-23

Development and testing of the gravitational wave antenna MiniGRAIL in its full-featured configuration

Proefschrift

ter verkrijging van
de graad van Doctor aan de Universiteit Leiden,
op gezag van de rector magnificus prof. mr. P.F van der Heijden,
volgens besluit van het College voor Promoties
te verdedigen op woensdag 23 mei 2012
klokke 16:15 uur

door

Oleksandr Usenko

geboren te Kharkiv, Oekraïne in 1980

Contents

Introduction

The weakness of gravitational interaction makes the detection of gravitational waves one of the most challenging tasks for experimental physics. While they were predicted by Einstein's Theory of General Relativity almost a century ago, they are still not measured directly, despite the dramatic improvement of the detectors sensitivity. So far, only indirect evidence of existence of gravitational waves was made by an observation of the binary pulsar $PSR1913 + 16$ made by Hulse and Taylor [1, 2]. The slowing down of the revolution period of the pulsar occurs at the exact rate predicted by general relativity for the emission of gravitational wave.

But a weak interaction with matter is what makes them so interesting for astrophysicists. Hardly absorbed by matter it allows physicists to look at events, which are not observable by electromagnetic waves detectors.

The history of gravitational wave detectors counts more than 45 years of development. Joseph Weber built the first antenna in 1965 [3] It was a 1.5 ton Aluminium bar, suspended in vacuum at room temperature. It had a resonant frequency of $1.6\,kHz$. In 1968 he built a second detector to do coincidence measurements. By using piezoelectric transducers he was able to reach a strain sensitivity $\frac{\Delta h}{h}$ in the order of 10^{-16}. Although he reported [4] measuring a coincidence signal between two detectors, the amplitude of the signal was way above the expected level for the gravitational waves and was not confirmed by the results of other groups. The current generation of detectors is approximately six orders of magnitude more sensitive, but is still not able to report a detection of a gravitational wave signal.

All currently existing gravitational wave detectors are based on two principles:

The first type are interferometric detectors: LIGO, consisting of two interferometers - LIGO Hanford and LIGO Livingston (USA)[5], VIRGO at Cascina (Italy)[6], GEO600 at Hannover (Germany)[7] and TAMA300 in Japan[8].

Another type is the resonant detector: bar detectors: AURIGA in Legnaro (Italy)[9], NAUTILUS at Frascati (Italy) and two spherical detectors: Mario Schenberg in Brasil [10] and MiniGRAIL [11] in Leiden.

This work only focuses on the latter type of detectors, and MiniGRAIL in particular. All resonant detectors are designed in a similar way. The sensitive part is the cylindrical or spherical mass with high mechanical quality factor(in the order of 10^6). It is mechanically well decoupled from the environment noise sources (seismic, acoustic, electric, etc). The intrinsic thermal noise of the detector mass is reduced by oper-

ation at cryogenic temperatures. A gravitational wave passing through a detector excites the quadrupole resonant modes of the resonant mass. To detect this motion, a secondary, much lighter, mechanical oscillator(transducer) is attached. Its resonance frequency is tuned to the one of the sensitive mode of the main resonator. This transducer is electrically coupled to the external readout circuit.

A spherical gravitational wave detector has many distinguishable features. Some of them it shares with the bar antennas (price, compactness, maintenance cost, resonance detection principle), but some are really unique: unlike the bar detectors, the sphere is equally sensitive for a gravitational wave coming from any direction. It is also capable of determining the polarization of the incident gravitational wave. One would have to construct 5 equivalent bars to obtain the same amount of information. The sphere also has a larger cross section than a bar for equal operating frequency. An overview of the properties of spherical gravitational wave detectors can be found in [12].

However, there are some practical problems in operating spherical detectors. An omnidirectional operation requires using multiple transducers, which affects the reliability of the detector. The calibration and data analysis of the spherical antenna is also more complicated. To solve this problem Johnson and Merkowitz proposed a configuration called a truncated icosahedral gravitational wave antenna (TIGA)[13]. The six transducers are placed on the 6 pentagonal faces of truncated icosahedron. High symmetry allowed developing a simple algorithm of reconstructing the gravitational signal, using fixed combinations of transducer outputs.

This thesis is focused on building the full acquisition system and preparation of MiniGRAIL for a first scientific run, with a full 6 transducer configuration at millikelvin temperatures.

The first chapter of this thesis gives a general introduction into gravitational waves and the principles of gravitational wave detection. An overview is focused on the properties of spherical resonant detectors and on the MiniGRAIL setup in particular.

Chapter 2 is focused on the development of MiniGRAIL acquisition system, Chapter 3 describes improvements in the setup that were made based on the results of preceding cool downs. In chapter 4 the results of the first calibration run of MiniGRAIL are presented. An application of a sensitive 2-stage SQUID amplifier, developed for MiniGRAIL, in magnetic resonance force microscopy (MRFM) experiment is described in chapter 5.

Chapter 1

Principles of operation of a spherical gravitational wave antenna MiniGRAIL

Introduction

The concept of a spherical gravitational wave detector was already suggested in the early seventies by [14]. Spherical detectors have a number of advantages:

- Omni-directionality. Due to its symmetric nature, a spherical detector is the only detector of gravitational waves with isotropic sky coverage and the capability of finding the location of the source. Both laser interferometers and bar detectors are unable to do this with just one detector.

- Ability to determine direction and polarization $h+$, $h\times$ of an incoming gravitational wave (in a multiple transducers configuration). A single sphere is capable of determining the source direction and polarization, because it has five degenerate modes of oscillation that interact with gravitational waves. An observatory consisting of two spherical detectors could give the exact location of the source, which makes it possible to determine the velocity of the gravitational waves and also decreases the false alarm rate.

- Large cross section compared to a bar detector. A sphere has a larger mass than a bar resonating at the same frequency and because it is equally sensitive for all directions and polarizations it has an energy cross section about 50 times larger than a bar of the same material.

- Since a spherical detector is quite compact, compared to other types of detectors, it is possible to fit it in a conventional type of cryostat. As a consequence such

a detector is relatively cheap and can be installed and operated in a typical research laboratory by a small scientific group.

- Toroidal modes of the sphere could possibly be used as vetoes for non-GW signals. Since the gravitational waves only excite the quadrupolar modes of the sphere, it is possible to use the signal from the other modes as a veto [15].

However, there are some practical problems in operating a spherical detectors. As we will describe below, the sphere has five vibrational modes that couple to gravitational waves. Hence a set of at least five(or even six, like in MiniGRAIL) mechanical resonators(transducers) followed by six low noise amplifiers is required. Six transducers, coupled to the sphere modes will result in at least 11 resonant modes which make the analysis complicated. Moreover, the advantages if the spherical detector come at a price of its reliability. A failure rate of 10% for a single read-out channel would result in only $\approx 50\%$ success rate if all six channels have to be operational. Fortunately, as we would see further in this thesis, it is possible to operate the detector with less than 6 working read-out channels without catastrophic degradation of its performance.

In this chapter we give a brief introduction into the theory, needed to understand the gravitational wave detection. A detailed description of classical theory of gravitational waves is out of scope of this thesis, but can be found for instance in [16] [17] or [18] A more specific and shorter explanation from the point of view of spherical gravitational wave detector can be found in [19, 20, 21, 22, 23].
In the second part of this chapter we will also give a description of an actual MiniGRAIL setup, detection method and expected sensitivity.

1.1   Interaction of gravitational waves with a physical body

In general relativity gravitational waves are ripples in the curvature of space-time that propagate with the speed of light. For any practical source of gravitational waves they can be described as small perturbation $h_{\mu\nu}$ of a flat space-time with a metric $\eta_{\mu\nu} = diag(-1, 1, 1, 1)$("linearized gravitational waves approximation")[17][24]:

$$g_{\mu\nu} = \eta_{\mu\nu} + h_{\mu\nu}, \text{ where } |h_{\mu\nu}| \ll 1, \tag{1.1}$$

Away from the source we can choose a gauge where gravitational wave metric perturbation $h_{\mu\nu}$ can be reduced to h_{ij}^{TT}, containing only spatial components. The superscript TT denotes a *transverse-traceless* gauge (TT gauge)[18]. A physical meaning of a TT gauge is that the gravitational wave is described as a plain wave perpendicular to propagation direction and the particle that was at rest before the wave came would remain at rest after the wave has passed.

We can further simplify the h_{ij} tensor by choosing a reference frame with the origin of coordinate system in the center of mass of the detector, and the z-axis oriented along the direction of incoming gravitational wave - a *wave-frame*. In a wave-frame, a time dependent $h_{ij}(t)$ tensor can be written as

$$h_{i'j'}(t) = \begin{bmatrix} h'_+(t) & h'_\times(t) & 0 \\ h'_\times(t) & -h'_+(t) & 0 \\ 0 & 0 & 0 \end{bmatrix} \tag{1.2}$$

where $h'_+ \equiv h_{x'x'} = -h_{y'y'}$ and $h'_\times \equiv h_{x'y'} = h_{y'x'}$ are the amplitudes of two gravitational wave polarizations, called the plus and cross polarizations. Primed indexes denote the wave-frame.

The force lines of two polarizations are shown on figure 1.1. A plus polarization would deform a ring of test masses into an ellipse with axes along with x and y directions. A cross polarization deforms a ring at $\frac{\pi}{4}$ angle to x and y directions.
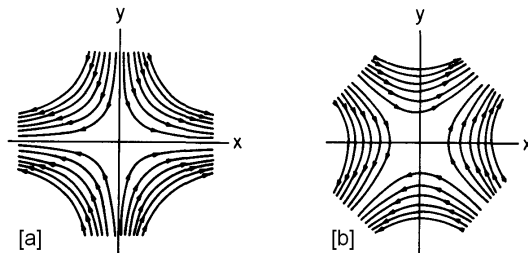
Figure 1.1: Force lines of *plus*[a] and *cross*[b] polarized gravitational wave propagating in *z-axis* direction[18]

The detector is better described in the reference frame, with the center being also located in the center of mass of the detector and the *z-axis* aligned with the local vertical, a *lab-frame* or *detector-frame*

In the lab-frame frame the physical effect of a passing gravitational wave is to produce a Newtonian force on a test particle. For a material with a density ρ at coordinate location x_i a time dependent force density $f^{GW}(x,t)$ is related to the metric perturbation by

$$f_i^{GW}(\mathbf{x}, t) = \frac{1}{2}\rho \sum_j \frac{\partial^2 h_{ij}(t)}{\partial t^2} x_j \tag{1.3}$$

This is a remarkable result, as from this point on the study of the interaction between the gravitational wave and the detector will not require involving general relativity.

1.1.1 Coupling of gravitational waves to the sphere

The equation (1.3) can be rewritten in spherical coordinates. For a spherical detector it is convenient to describe the angular part with five second order spherical harmonics $Y_{2m}(\theta, \phi)$ $(m = 1 \ldots 5)$ [20]

$$\mathbf{Y}_{2m} = \sqrt{\frac{15}{16\pi}} \begin{pmatrix} \cos 2\varphi \sin^2\theta \\ \sin 2\varphi \sin^2\theta \\ \sin\varphi \sin 2\theta \\ \cos\varphi \sin 2\theta \\ \frac{1}{\sqrt{3}}(3\cos^2\theta - 1) \end{pmatrix} \tag{1.4}$$

The resulting time dependent expansion coefficients, $h_m(t)$, are called spherical amplitudes [20]. They are a complete and orthogonal representation of the Cartesian metric tensor $h_{ij}(t)$. They only depend on the two wave-frame amplitudes and the direction of propagation.

The conversion from a *wave-frame* to a *lab-frame* can be done by applying the rotation matrix. After the rotation, the spherical amplitudes in the lab-frame can be expressed in terms of the polarization amplitudes and the source direction:

$$\mathbf{h}_m = \mathbf{T_V} \begin{pmatrix} h_+ \\ h_\times \end{pmatrix},$$

$$\mathbf{T_V} = \begin{pmatrix} \frac{1}{2}\left(1 + \cos^2\beta\right)\cos 2\gamma & \cos\beta \sin 2\gamma \\ \frac{1}{2}\left(1 + \cos^2\beta\right)\sin 2\gamma & \cos\beta \cos 2\gamma \\ \frac{1}{2}\sin 2\beta \sin\gamma & \sin\beta \cos\gamma \\ \frac{1}{2}\sin 2\beta \cos\gamma & \sin\beta \sin\gamma \\ \frac{1}{2}\sqrt{3}\sin^2\beta & 0 \end{pmatrix} \begin{pmatrix} \cos 2\alpha & \sin 2\alpha \\ -\sin 2\alpha & \cos 2\alpha \end{pmatrix}, \tag{1.5}$$

where rotation angles β, γ and α follow standard Euler angles convention(see figure 1.2) - β is the angle between z' and z axis and γ is the angle between the line of nodes N and x axis [22]. Angle α shows the rotation around the wave-frame axis z' and gives the information about the gravitational wave polarization.

1.1.2   Modes of the Uncoupled Sphere

In this section we describe the interaction of the gravitational wave with a spherical antenna. The mechanics of a spherical antenna is described by ordinary elastic theory. Force, acting on elastic body will cause a deformation of $x = x_0 + u(x,t)$, where x_0 is the equilibrium position of a volume element. The equation of motion of an elastic body is

$$\rho \frac{\partial^2 \mathbf{u}}{\partial t^2} = (\lambda + \mu)\nabla(\nabla \cdot \mathbf{u}) + \mu\nabla^2 \cdot \mathbf{u} + \mathbf{f}, \tag{1.6}$$

where ρ is the material density, $\mathbf{f}$ is an applied force density and λ, μ are Lamé coefficients, related to the stress tensor σ_{ij} by means of Hooks law for isotropic elastic body:

$$\sigma_{ij} = \lambda \operatorname{tr}(u_{ij})\delta_{ij} + 2\mu u_{ij} \tag{1.7}$$
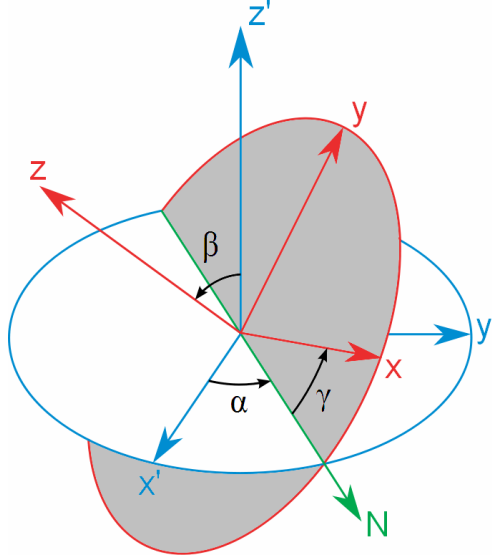
Figure 1.2: Euler angles transformation

where $u_{ij} = \frac{1}{2}(\partial_i u_j + \partial_j u_i)$ and δ_{ij} is the Kronecker delta. The equation (1.6) has a solution in a form of

$$\mathbf{u}(\mathbf{x}, t) = \sum_m a_m(t)\psi_m(\mathbf{x}), \tag{1.8}$$

where $\psi_m(\mathbf{x})$ is the spacial eigenfunction of the m_{th} normal mode of the sphere and $a_m(t)$ is a mode amplitude.

The eigenfunctions of an uncoupled sphere can be written in terms of the spherical harmonics:

$$\Psi_{nlm}(r, \theta, \phi) = (\alpha_{nl}(r)\hat{\mathbf{r}} + \beta_{nl}(r)R\nabla)Y_{lm}(\theta, \phi) \tag{1.9}$$

where index l is even. The radial eigenfunctions $\alpha_{nl}(r)$ and $\beta_{nl}(r)$ determine the motion in the radial and tangential directions respectively and depend on the radius R and the material of the sphere.

According to general relativity, only the five quadrupolar modes of the sphere will couple to the force density of a gravitational wave($l \equiv 2$ in the equation 1.9). For a ideal sphere all the modes are degenerate - they have the same frequency and are distinguished only by their orientation(Fig 1.3).

The gravitational force $F_m(t)$, acting on a fundamental quadrupolar mode m of the sphere from a gravitational wave is given by the overlap integral between the eigenfunctions of the sphere and the gravitational force:
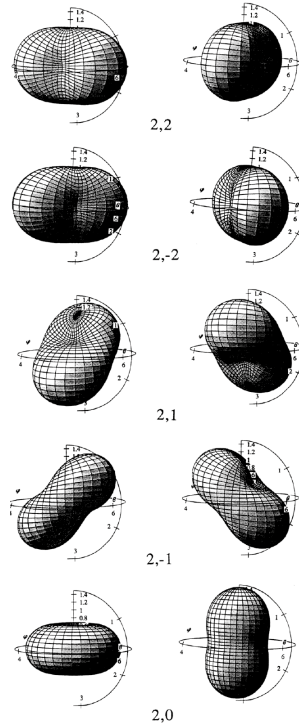
Figure 1.3: Visualization of the spheroidal quadrupolar modes of a sphere [25]

$$F_m(t) = \int \Psi_{2m}(x) \cdot f^{GW}(x,t)d^3x = \frac{1}{2}M\chi R\frac{\partial^2 h_m(t)}{\partial t^2} \qquad (1.10)$$

Each spherical component of the gravitational field determines uniquely the effective force on the corresponding mode of the sphere. We can interpret the effective force $F_m(t)$ in each mode as the product of the physical mass of the sphere M, an effective length χR (a fraction of the sphere radius), and the gravitational acceleration $\frac{1}{2}\frac{\delta^2 h_m(t)}{\delta t^2}$. The value of the coefficient χ depends on the Poisson ratio of the sphere material. For CuAl sphere it is equal to 0.327.

1.2 Operation of a Spherical Gravitational Wave Antenna

In this section we give a description of the practical implementation of a spherical gravitational waves detector equipped with single mode capacitive resonant transducers and read-out by a low noise cryogenic amplifier (a 2-stage SQUID amplifier).

1.2.1 Secondary resonators (transducers)

As shown in the previous section, by measuring the quadrupolar modes of the sphere, we can directly measure the effective force on the sphere and thus the spherical amplitudes of the gravitational wave. To improve the displacement sensitivity, the standard technique for resonant detectors is to place secondary resonators (transducers) on their surface, strongly coupled to the quadrupolar modes.

The resonant transducer is a mechanical resonator, with a resonant frequency tuned to the one of the antenna. If both the oscillators have the same resonant frequency $\omega_s = \omega_t \equiv \omega_0$, the energy E transferred from the antenna to a transducer is given by the expression

$$E = \frac{1}{2} m_s \omega_0^2 x_a^2 = \frac{1}{2} m_t \omega_0^2 x_t^2, \qquad (1.11)$$

then the displacement amplitude of the transducer is related to the sphere displacement as

$$x_t = \sqrt{\frac{m_s}{m_t}} x_a \equiv \mu^{-1} x_a, \qquad (1.12)$$

so the displacement of the much lighter mass of the transducer m_t is amplified by a factor $\mu^{-1} = \sqrt{m_s/m_t}$, where m_s is the equivalent mass of the antenna. The coupled resonances split in two normal modes by $\omega_a \cdot \mu$ and their splitting increases with the transducer mass as $\sqrt{m_t}$.

Since for an ideal sphere the quadrupolar modes are degenerate, but have a different shape, we need a set of at least five transducers to be attached to the sphere in order to acquire the individual modes amplitudes.

Let's consider a sufficient set of j transducers placed on the sphere surface at arbitrary positions (ϕ_j, θ_j). For a given mode m, we can define a set of radial displacements of the sphere surface at transducer locations - a *pattern vector*. For all quadrupolar modes these vectors form an $m \times j$ *pattern matrix* $\mathbf{B}_{mj}$, defined as [20]:

$$\mathbf{B}_{mj} = \frac{1}{\alpha} \hat{\mathbf{r}} \Psi_m(\Theta_j, \phi_j) \equiv Y_m(\Theta_j, \phi_j) \qquad (1.13)$$

Physically, the $\mathbf{B}_{mj}$ matrix converts the quadrupolar modes amplitudes $\mathbf{a}_m$ to the displacement amplitudes of the sphere surface at the transducers position $\mathbf{q}_j$.

Currently, in the MiniGRAIL operation we only use one-mode capacitive resonant transducers, so we are going to concentrate on them in the rest of the thesis. A model and a design considerations of two-mode inductive transducer, developed for MiniGRAIL is given in [25].

Capacitive resonant transducers

In a capacitive transducer, the constant electric field is stored in a flat capacitor, formed by the flat surface of the resonating mass and the electrode. The distance between two surfaces is of order $10-50$ micrometers. The electrode is rigidly connected

to the surface of the sphere and the resonator is tuned to the sphere modes. In
principle that means that the electrode is moving together with the surface of the
sphere, but since typically $\mu \sim 10^{-2}$, the motion of the electrode can be neglected.
Motion of a resonating mass modulates the charge of a capacitor. The input coil of the
dc-SQUID chip is coupled to the capacitive transducer via a high-Q superconductive
impedance matching transformer. The matching transformer is used to match the low
input impedance of the SQUID amplifier with the high impedance of the capacitor.
An electromechanical scheme of one read-out channel of MiniGRAIL is shown on
figure 1.4.
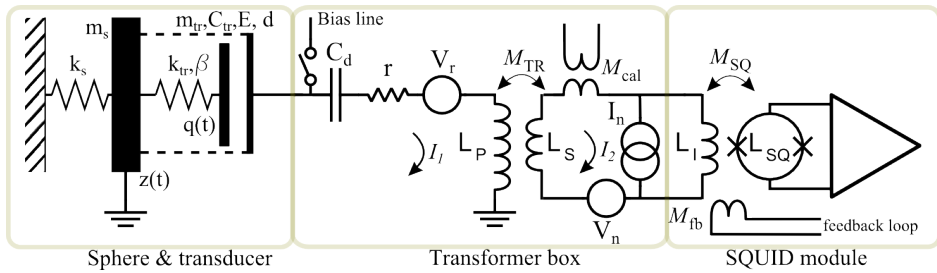
Figure 1.4: Scheme of MiniGRAIL read-out with a capacitive transducer coupled to a
SQUID amplifier by impedance matching transformer

The mechanical part of the detector can be modeled by a set of coupled harmonic
oscillators. m_s is the effective mass [1] of the sphere, m_{tr}, k_{tr}, β and are the effective
mass, spring constant and damping of the transducer respectively.

Electrically, the transducer is described as a parallel plate capacitor with capaci-
tance C_{tr} and a gap between electrodes d.

When the transducer is charged through the bias line, its motion $q(t)$ modulates
the capacitor C_{tr} resulting and ac current I_1. The current couples to the SQUID in-
put circuit through a superconducting transformer. A decoupling capacitor $C_d \gg C_{tr}$
prevents the transducer from discharging through the primary coil of the transformer.

Ideally the primary inductance of the transformer L_p should be chosen to match
the impedance of the transducer and the secondary inductance L_s to match the
SQUID input inductance. The mutual inductance of the transformer is given by
$M = k\sqrt{L_pL_s}$, where the coupling factor $k \approx 0.85 - 0.9$.

In the scope of this chapter a SQUID is modelled as a linear current amplifier with
current and voltage noise I_n and V_n respectively[26].

An electric field in the transducer gap induces a force between the capacitor plates
which modifies the mechanical spring constant of the transducer resonator. For a ca-
pacitive transducer the force is attractive so the spring constant and the resonant
frequency are reduced. The change of resonant frequency is an important property of
a transducer, indicating how efficiently a mechanical motion of the resonator is con-

---

[1]Effective mass is the fraction of the physical mass of the sphere M_s, associated with each of the
five quadrupolar modes and is equal to $m_s = 5/6\chi M_s$[23]

verted to an electrical signal. The electromechanical coupling coefficient β is defined as:

$$\beta = \frac{\omega_0^2 - \omega_t^2}{\omega_t^2} \tag{1.14}$$

where ω_0 is the resonant frequency when the transducer is not biased, and ω_t is the shifted frequency. For a capacitive transducer the coupling is [25]:

$$\beta = \frac{C}{d_0^2} \frac{V^2}{\omega^2 m_{eff}} \tag{1.15}$$

where C is the transducer capacitance, d_0 is the capacitor gap, V is the bias voltage and m_{eff} is the effective mass of the transducer.

By combining 1.14 and 1.15 we get:

$$f_t^2 = f_0^2 - \frac{C}{(2\pi)^2 m_{eff} d_0^2} V^2 \tag{1.16}$$

By measuring the voltage dependence of a resonant frequency of the modes we can measure the coupling of the transducer to the modes of the sphere and the effective mass, associated with the modes.

Mode Channels

In a real experiment we need to find a way to convert the measured transducer amplitudes $\mathbf{q_j}(t)$ to a spherical gravitational wave amplitude $h_m(t)$. Since the transducers are coupled to the motion of the surface of the sphere, even the single excited spherical mode would result in an excitation of most transducers. Merkowitz has shown [13] that is is possible to reconstruct each of the spherical amplitudes by building a linear combination of the measured amplitudes $\mathbf{q_j}(t)$. These linear combinations are called *mode channels* to indicate that each one corresponds to a single mode amplitude $a_m(t)$ and hence to a single amplitude $h_m(t)$. Since mode channels correspond to the quadrupolar modes of the sphere, they relate to the amplitudes $\mathbf{q_j}(t)$ by means of the pattern vector:

$$\mathbf{g_m}(t) = \mathbf{B_{mj}}^{-1} \mathbf{q_j}(t), \tag{1.17}$$

where $\mathbf{g_m}(t)$ is the mode channels vector.

Once we have built the mode channels, we can form a *detector response* matrix $\mathbf{A(t)}$ that in the absence of noise is equal to the Cartesian strain tensor $h_{ij}(t)$ in the lab frame[21]:

$$\mathbf{A} = \begin{bmatrix} g_1 - \frac{1}{\sqrt{3}} g_5 & g_2 & g_4 \\ g_2 & -g_1 - \frac{1}{\sqrt{3}} g_5 & g_3 \\ g_4 & g_3 & \frac{2}{\sqrt{3}} g_5 \end{bmatrix} \equiv \begin{bmatrix} h_{xx} & h_{xy} & h_{xz} \\ h_{yx} & h_{yy} & h_{yz} \\ h_{zx} & h_{zy} & h_{zz} \end{bmatrix} \tag{1.18}$$

According to the principal axis theorem the three eigenvectors of $\mathbf{A(t)}$ are parallel to the three principle axes of the deformation ellipsoid, and the corresponding eigenvalues show the radial deviations. To determine the direction of the incoming gravitational wave we need to know the shape and the orientation of the ellipsoid it produces. For a transverse wave, one of the eigenvalues is equal to zero, but its eigenvector will point in the direction of the incident gravitational wave. The position determination is only unique within a hemisphere - sources in opposite directions are indistinguishable.

1.2.2   Model of the sphere with capacitive transducers

Let us look at the equation of motion of a single transducer, mounted on the sphere. If we define the radial motion of the sphere at transducer position as $z(t)$ and relative distance between the resonator and the sphere surface as $q(t)$ then the inertial displacement of the resonator mass is $q + z$ and the equation of motion of the resonator is[19]

$$m_{tr}(\ddot{q}(t) + \ddot{z}(t)) + k_{tr}q(t) = f, \tag{1.19}$$

where f is the force acting between the sphere and the resonator. If we now consider a set of J transducers, and take into account that the normal mode amplitudes are related to the sphere displacement by means of the pattern matrix $\mathbf{B}_{mj}$, then for each resonator the equation of motion is:

$$m_{tr_j}\ddot{q}_j(t) + m_{tr_j}\sum_m \alpha\mathbf{B}_{mj}\ddot{a}_m(t) + k_{tr}q_j(t) = f_j. \tag{1.20}$$

The equation of motion of the sphere modes is given by[19]:

$$m_s\ddot{a}_m(t) + k_s a_m(t) = \sum_j \alpha\mathbf{B}_{mj}[k_{tr}q_j(t) - f_j(t)] + F_m(t), \tag{1.21}$$

By combining equation (1.20) and equation (1.21) we can write down the coupled equation of motion of system in a matrix form

$$\begin{bmatrix} \mathbf{m_s} & \mathbf{0} \\ \alpha\mathbf{m_{tr}B}^T & \mathbf{m_{tr}} \end{bmatrix} \begin{bmatrix} \ddot{\mathbf{a}}(t) \\ \ddot{\mathbf{q}}(t) \end{bmatrix} + \begin{bmatrix} \mathbf{k_s} & -\alpha\mathbf{Bk_{tr}} \\ \mathbf{0} & \mathbf{k_{tr}} \end{bmatrix} \begin{bmatrix} \mathbf{a}(t) \\ \mathbf{q}(t) \end{bmatrix}$$
$$= \begin{bmatrix} \mathbf{I} & -\alpha\mathbf{B} \\ \mathbf{0} & \mathbf{I} \end{bmatrix} \begin{bmatrix} \mathbf{F}(t) \\ \mathbf{f}(t) \end{bmatrix}, \tag{1.22}$$

where $\mathbf{m_s}$, $\mathbf{k_s}$ are the diagonal matrices of effective masses and spring constants of each mode and $\mathbf{m_{tr}}$, $\mathbf{k_{tr}}$ are the diagonal matrices of masses and spring constants of each transducer.

The equation of motion does not include any deviations of quadrupole modes shape due to the attached transducers and the suspension hole. It has been shown both by finite element analysis and experimentally that for a sphere with a hole

and transducers with mass less then 1% of the sphere mass, mode shapes change is negligible. [27, 19, 12]

It is possible to simplify the equation (1.22) to $5 + J$ decoupled harmonic oscillator equations by transforming it to a normal coordinate system [21]

After applying Fourier transformation we get [23]

$$[-\omega^2 \mathbf{M} + \mathbf{K}] \left[\begin{array}{c} \mathbf{a}(\omega) \\ \mathbf{q}(\omega) \end{array} \right] = \mathbf{A} \left[\begin{array}{c} \mathbf{F}(\omega) \\ \mathbf{f}(\omega) \end{array} \right], \tag{1.23}$$

where we have defined mass $\mathbf{M}$, elastic $\mathbf{K}$ and coupling $\mathbf{A}$ matrices

$$\mathbf{M} \equiv \left[\begin{array}{cc} \mathbf{m_s} & \mathbf{0} \\ \alpha \mathbf{m_{tr}} \mathbf{B}^T & \mathbf{m_{tr}} \end{array} \right]$$

$$\mathbf{K} \equiv \left[\begin{array}{cc} \mathbf{k_s} & -\alpha \mathbf{B} \mathbf{k_{tr}} \\ \mathbf{0} & \mathbf{k_{tr}} \end{array} \right] \tag{1.24}$$

$$\mathbf{A} \equiv \left[\begin{array}{cc} \mathbf{I} & -\alpha \mathbf{B} \\ \mathbf{0} & \mathbf{I} \end{array} \right]$$

If we also include the electric circuit, the final equation of motion of entire detector becomes [23]

$$\underbrace{\left[\begin{array}{ccc} \mathcal{M} & \mathbf{Z_{BA}} & \mathbf{0} \\ \mathbf{0} & \mathbf{E} & \\ \mathbf{0} & \mathbf{0} & \mathbf{Z} \end{array} \right]}_{\mathcal{Z}} \left[\begin{array}{c} \mathbf{a}(\omega) \\ \mathbf{q}(\omega) \\ \mathbf{I_1}(\omega) \\ \mathbf{I_2}(\omega) \end{array} \right] = \mathbf{A}' \left[\begin{array}{c} \mathbf{F}(\omega) \\ \mathbf{f}(\omega) \\ \mathbf{V_r}(\omega) \\ \mathbf{V_n}(\omega) \end{array} \right], \tag{1.25}$$

where $\mathcal{M} = -\omega^2 \mathbf{M} + \mathbf{K}$, $\mathbf{E}$ is a diagonal matrix of electric fields in transducers gap, $\mathbf{Z}$ is the $2J \times 2J$ impedance matrix, defined as

$$\mathbf{Z} = \left[\begin{array}{cc} \mathbf{Z_{11}} & \mathbf{Z_{12}} \\ \mathbf{Z_{21}} & \mathbf{Z_{22}} \end{array} \right],$$

where each component $\mathbf{Z_{ij}}$ is a diagonal matrix of $J \times J$ elements with diagonal components equal to

$$\begin{aligned} \mathbf{Z_{11}}^j &= r^j + i\omega L_p^j + \frac{1}{i\omega C_{tr}^j}, \\ \mathbf{Z_{12}}^j &= -i\omega M_{TR}^j, \\ \mathbf{Z_{21}}^j &= -i\omega M_{TR}^j, \\ \mathbf{Z_{22}}^j &= i\omega(L_s{}^j + L_I{}^j). \end{aligned} \tag{1.27}$$

$\mathbf{Z_{BA}} = \begin{bmatrix} -\alpha\mathbf{B} \\ \mathbf{I} \end{bmatrix} \frac{\mathbf{E}}{i\omega}$ is the $(5+J) \times J$ back action matrix, which represents the effect of the current I_p on the mechanical system, and $\mathbf{A}' = \begin{bmatrix} \mathbf{A} & \mathbf{0} \\ \mathbf{0} & \mathbf{I} \end{bmatrix}$

We can invert the $\mathcal{Z}$ matrix and rewrite the equation (1.25) in the form

$$\begin{bmatrix} \mathbf{a}(\omega) \\ \mathbf{q}(\omega) \\ \mathbf{I_1}(\omega) \\ \mathbf{I_2}(\omega) \end{bmatrix} = \mathcal{Z}^{-1}\mathbf{A}' \begin{bmatrix} \mathbf{F}(\omega) \\ \mathbf{f}(\omega) \\ \mathbf{V_r}(\omega) \\ \mathbf{V_n}(\omega) \end{bmatrix} \equiv \mathbf{G} \begin{bmatrix} \mathbf{F}(\omega) \\ \mathbf{f}(\omega) \\ \mathbf{V_r}(\omega) \\ \mathbf{V_n}(\omega) \end{bmatrix}. \tag{1.28}$$

Equation (1.28) gives us the relation between the forces generated in the system and the amplitudes of the sphere modes, transducers displacements and the currents in the electrical read-out circuits. In practice the only values we can measure experimentally are the currents in the input coils of the SQUIDs $\mathbf{I_2}$, so we are only interested in J last rows of $\mathbf{G}$ matrix, denoted by $\mathbf{G_I}$. The current at the SQUID input also includes the contribution of the current noise from the SQUID itself:

$$\mathbf{I}(\omega) = \mathbf{G_I} \begin{bmatrix} \mathbf{F}(\omega) \\ \mathbf{f}(\omega) \\ \mathbf{V_r}(\omega) \\ \mathbf{V_n}(\omega) \end{bmatrix} + \mathbf{I_n}(\omega) \equiv \mathbf{G_I}\mathcal{F}(\omega) + \mathbf{I_n}(\omega) \tag{1.29}$$

We can compute a noise spectral density matrix $\mathbf{S_I}$ defined as

$$\mathbf{S_I} = \mathbf{I}(\omega)\mathbf{I}^*(\omega) = \mathbf{G_I}\mathcal{F}\mathcal{F}^*\mathbf{G_I^*} + \mathbf{G_I}\mathcal{F}\mathbf{I_n^*} + \mathbf{I_n}\mathcal{F}^*\mathbf{G_I^*} + \mathbf{I_n}\mathbf{I_n^*} \tag{1.30}$$

The SQUID noise is not correlated with other noise sources in the system, so the terms $\mathbf{FI_n^*}$ and $\mathbf{I_nF^*}$ cancel out, moreover the the noises of different SQUIDs are also uncorrelated, so $\mathbf{I_nI_n^*}$ contains only autocorrelation terms, or in other words the matrix $\mathbf{S_{I_n}} = \mathbf{I_nI_n^*}$ is diagonal. As a result the noise spectral density matrix in the equation (1.30) is reduced to

$$\mathbf{S_I} = \mathbf{G_I}\mathcal{F}\mathcal{F}^*\mathbf{G_I}^* + \mathbf{S_{I_n}} \tag{1.31}$$

Generally, a transducer does not couple only to a single sphere mode, but to a set of modes. This means that different transducers couple through the sphere modes and the noise spectra of transducers are correlated, so $\mathbf{S_I}$ matrix is not diagonal. Further we will discuss a way to combine the transducer outputs to build the uncorrelated channels.

We limit the analysis to the case where in the absence of gravitational waves signal the forces generated in the system are due to the thermal noise. The noise spectral density of a mechanical oscillators is given by [28]

$$\begin{aligned} S_F &= 4k_BT\frac{m_s\omega_s}{Q_s} \\ S_f &= 4k_BT\frac{m_{tr}\omega_{tr}}{Q_{tr}} \end{aligned} \tag{1.32}$$

Electric noise due to the losses in the capacitor, denoted by r, is

$$S_{V_r} = 4k_B T r \tag{1.33}$$

Voltage and current noises of the SQUID amplifier, according to Clarke-Teshe model [26], are

$$
\begin{aligned}
S_{V_n} &= 11 \frac{k_B T}{R_s} M_{SQ}^2 \omega^2 \\
S_{I_n} &= 16 \left(\frac{L_{SQ}}{M_{SQ}} \right)^2 \frac{k_B T}{R_s},
\end{aligned}
\tag{1.34}
$$

where R_s is the shunt resistance of the SQUID.

1.2.3 Detector sensitivity

Strain sensitivity

The performance of a gravitational waves detector is characterised by the ratio of the output signal due to the gravitational waves to the one due to intrinsic noise of the detector.

We can write down the equation (1.10) in a frequency domain [20]

$$\mathbf{F}^{GW} = -\frac{1}{2} M \chi R \omega^2 \mathbf{h_m} = -\frac{1}{2} M \chi R \omega^2 \mathbf{T_V} \begin{pmatrix} h_+ \\ h_\times \end{pmatrix}, \tag{1.35}$$

then in the absence of noise the output signal of the detector is

$$\mathbf{I}^{GW}(\omega) \equiv \mathbf{G_I} \begin{bmatrix} \mathbf{F}^{GW}(\omega) \\ \mathbf{0} \\ \mathbf{0} \\ \mathbf{0} \end{bmatrix} = \hat{\mathbf{G}}_\mathbf{I} \mathbf{F}^{GW}(\omega) = -\frac{1}{2} M \chi R \omega^2 \hat{\mathbf{G}}_\mathbf{I} \mathbf{T_V} \begin{pmatrix} h_+ \\ h_\times \end{pmatrix}, \tag{1.36}$$

where $\hat{\mathbf{G}}_\mathbf{I}$ is a submatrix of $\mathbf{G_I}$ containing only the first row of 5 elements.
In the presence of noise the signal-to-noise ratio for a gravitational wave signal of amplitude $\mathbf{h} = \begin{pmatrix} h_+ \\ h_\times \end{pmatrix}$ is given by [29]

$$SNR^2 = \int_{-\infty}^{\infty} \sigma(w) \frac{d\omega}{2\pi}, \tag{1.37}$$

where the integrand

$$\sigma(\omega) = \mathbf{I}^{*GW}(\omega) \mathbf{S_I}^{-1} \mathbf{I}^{GW}(\omega) = \frac{(M \chi R)^2 \omega^4}{4} \mathbf{h}^* \mathbf{T_V^*} \hat{\mathbf{G}}_\mathbf{I}^* \mathbf{S_I}^{-1} \hat{\mathbf{G}}_\mathbf{I} \mathbf{T_V} \mathbf{h}, \tag{1.38}$$

gives the available SNR power density per unit bandwidth.

At a sensitivity limit $SNR = 1$ and since we have no information about the polarization of the incident wave we can set $h_\times \equiv 0$, $h_+ \equiv h$, so $\mathbf{h}^*\mathbf{h} = h^2$. We can now solve the equation (1.38) for h

$$h(\omega) = \left(\frac{4}{(M\chi R)^2 \omega^4} \frac{\mathbf{S_I}}{\mathbf{T_V^* \hat{G}_I^* \hat{G}_I T_V}} \right)^{1/2} \equiv \left(\frac{4}{(M\chi R)^2 \omega^4} \frac{\mathbf{S_I}}{\mathbf{Tf}} \right)^{1/2}, \qquad (1.39)$$

where $\mathbf{Tf} = \mathbf{T_V^* \hat{G}_I^* \hat{G}_I T_V}$ is the transfer matrix between the gravitational wave force and the current spectral density at the input of the SQUIDs. Note that the transfer matrix includes an angular dependent $\mathbf{T_V}$ component and thus is direction dependent. By averaging over all directions we get the expression for the average sky sensitivity of the detector [28]

$$\langle h(\omega) \rangle = \frac{2\sqrt{5}}{M\chi R\omega^2 \sqrt{\mathrm{trace}(\hat{G}_I^* S_I^{-1} \hat{G}_I)}}. \qquad (1.40)$$

The amplitude of a gravitational wave, resulting in a $SNR = 1$ is called the strain sensitivity and is conventionally referred to as $S_{hh}(\omega) \equiv h(\omega)^2$.

Directional sensitivity

From the equations in the previous chapter we can conclude that in the absence of noise the spherical detector is able to locate the exact direction of the gravitational waves source. If the noise contribution is not negligible, the angular resolution is degraded. We define the angular resolution as

$$\Delta\Omega = \pi((\theta - \theta_0)^2 + \sin^2\theta_0(\phi - \phi_0)^2), \qquad (1.41)$$

where (ϕ_0, θ_0) is the actual direction of the source and (ϕ, θ) is the calculated direction. Physically, $\Delta\Omega$ is the area of a circle on the unit sphere with a center at (ϕ_0, θ_0) and a radius showing the difference between a real and a calculated direction. It can be shown [30] that $\Delta\Omega$ depends on the SNR as

$$\Delta\Omega = \frac{2\pi}{SNR}. \qquad (1.42)$$

A result of 200 Monte Carlo simulations for different signal-to-noise ratios reported in [30] is shown on figure 1.5. The simulated signal was a linearly polarised gravitational wave propagating in the direction $\phi_0 = 2\,rad$, $\theta_0 = 1\,rad$. For $SNR = 1$ the points are distributed almost uniformly over the sky, and the direction estimation is not possible. For the $SNR = 10$, the distribution of trials starts to converge on the vicinity of the true wave direction. From these simulations the minimum SNR required for direction reconstruction is approximately 10 for a spherical detector.
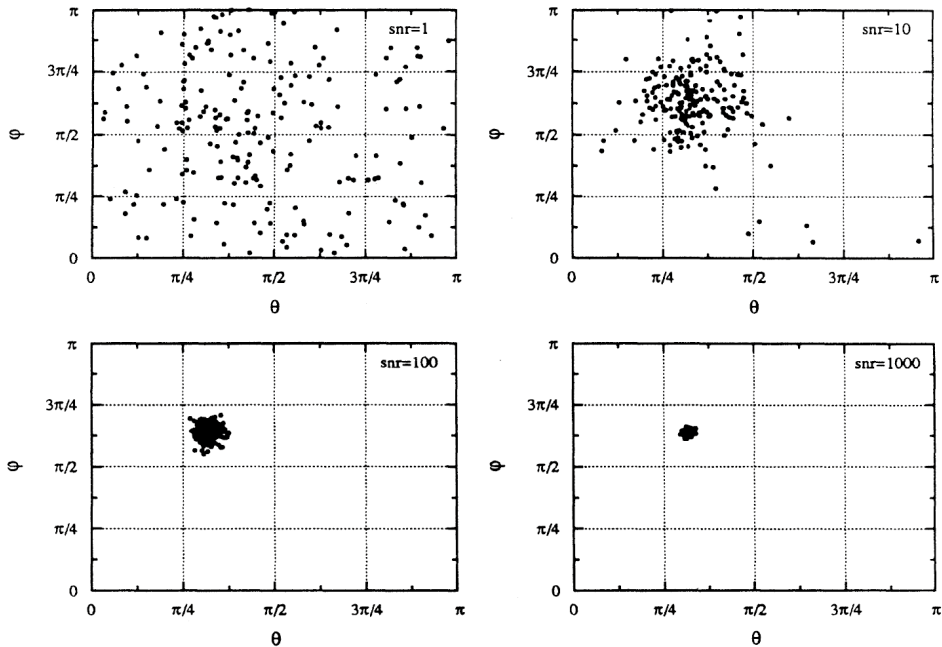
Figure 1.5: Calculated wave direction for 200 simulations each for various values of the signal- to-noise ratio. The simulated wave signal was a linearly polarised gravitational wave propagating in the direction $\phi_0 = 2\,rad$, $\theta_0 = 1\,rad$. Figure is taken from [30]

1.2.4   Measuring strain sensitivity of a real detector

In a real experiment the signal we are measuring is a voltage at the output of the SQUID electronics. The voltage can easily be converted to the current at the input of the SQUIDs $\mathbf{I}(\omega)$ and if we preserved the phase information we can build the noise spectral density matrix $\mathbf{S_I}$ from equation (1.30). In order to calculate the sensitivity we also need to evaluate the transfer matrix $\mathbf{Tf}$. It can either be calculated analytically, as described in [31, 32], or measured experimentally as we do in this work. The main disadvantage of the calculated transfer matrix, besides the system's complexity, is that we need to model the real system as precisely as possible, otherwise the inconsistency between the transfer matrix and the measured noise spectra would produce artifacts on a strain sensitivity curve. Purely theoretical works, as the ones listed above, obviously do not have this problem, as they use the same set of system parameters to generate the noisy detector output and to build the transfer matrix.

In particular, we only have to measure the admittance submatrix $\hat{\mathbf{G}}_\mathbf{I}$ as $\mathbf{T_V}$ is a purely geometric factor depending on the detector's reference frame orientation. From the equation (1.36) we see that if we can find the way to apply a known force to the normal modes of the sphere and measure the output current we can easily build

the $\hat{\mathbf{G}}_{\mathbf{I}}$ matrix. A force applied to the surface of the sphere excites a combination of the normal modes, defined by the pattern vector. For a set of calibrators, radially exciting the sphere, the forces, acting on the modes are

$$\mathbf{F_m}(\omega) = \alpha \mathbf{B_c} \mathbf{F_c}(\omega), \tag{1.43}$$

where $\mathbf{B_c}$ is the pattern matrix for calibrators positions and $\mathbf{F_c}$ are the forces applied to the sphere surface by calibrators. By generating a proper linear combination of calibrators forces we can simulate the effect of gravitational wave coming from any direction. We suggest using a set of at least 5 mass-loaded PZT calibrators, as they are very compact and give more flexibility than a single detuned capacitive calibrator used in the previous runs [25]. In chapter 4 we will also discuss the way of measuring the force that calibrators apply to the sphere.

It is convenient to convert the current at transducers output into 5 equivalent mode channel currents, as they correspond to spherical components of the gravitational wave as described in section 1.2.1. The mode channel current vector construction is straightforward

$$\mathbf{I_m}(\omega) = \mathbf{B}\mathbf{I}(\omega) = \alpha \mathbf{B}\hat{\mathbf{G}}_{\mathbf{I}}\mathbf{B_c}\mathbf{F_c}(\omega). \tag{1.44}$$

Because the mode channels are statistically independent, their current spectral density matrix $\mathbf{S_{I_m}}(\omega) = \mathbf{I_m}(\omega)\mathbf{I_m^*}(\omega)$ is diagonal and we can treat a 5-channel spherical detector as a set of 5 independent single-channel detectors, applying much simpler data analysis and filtering algorithms developed for the bars.

From equation (1.44) we see that in order to calculate the $\hat{\mathbf{G}}_{\mathbf{I}}$ matrix from known $\mathbf{F_c}(\omega)$ and measured $\mathbf{I}(\omega)$ we need to invert the pattern matrix $\mathbf{B}$. The solution of the problem depends on the number and the position of transducers. If we have less than five transducers - the system is underdetermined, and the mode channels cannot be built.

Since five quadrupolar modes of the sphere contain complete information about the spherical amplitudes of a gravitational wave, it would be natural choice to try the configuration with 5 transducers tuned to the sphere modes. However Johnson and Merkowitz have discovered that for every arrangement of five transducers they tried the transducer-mode coupling was always non optimal [20]. They achieved the best results with a special 6-transducer arrangement called *Truncated Icosahedral Gravitational Wave Antenna* (TIGA).

Special transducers arrangement - TIGA

TIGA consists of a set of six transducers placed on pentagonal faces of a Truncated Icosahedron (TI). The resonators arrangement for TIGA is shown on figure 1.6. The transducers are placed at two polar angles, $\theta = 37.3773^o$ and 79.1876^o. Their azimuthal angles are multiple of 60°.

The high symmetry of the TI arrangement affects its pattern matrix. Each pattern vector is orthogonal to the others and has the same magnitude $\sqrt{\frac{3}{2\pi}}$:
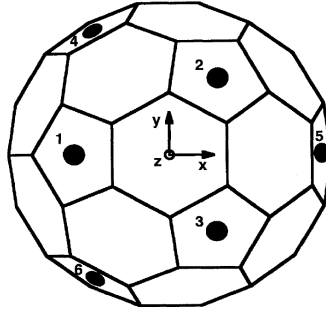
Figure 1.6: The truncated icosahedral gravitational wave antenna (TIGA) with secondary resonator locations indicated. The numbering of the transducers positions corresponds to the ordering used in the rest of this thesis. Figure is taken from [19].

$$\mathbf{BB}^* = \frac{3}{2\pi}\mathbf{I}, \tag{1.45}$$

where $\mathbf{I}$ is the 5×5 identity matrix. This property means that the pattern matrix for TIGA transducer arrangement is a unitary matrix, and we can substitute the inversion, which is not possible for rectangular 5×6 $\mathbf{B}$ matrix, with a transpose. It also shows that there is indeed no cross-correlation between the modes and the sphere modes are a direct measurement of the gravitational spherical amplitudes.

In addition to orthogonality, the sum of the components of each pattern vector is zero.

$$\mathbf{B1} = \mathbf{0}, \tag{1.46}$$

where $\mathbf{1}$ is a 6×1 column vector of ones and $\mathbf{0}$ is a 5×1 column vector of zeroes.

A practical advantage of the TIGA configuration is that it only involves the use of equal mass radial transducers similar to the ones developed for other resonant detectors.

A disadvantage of the TIGA configuration is that we use 6 transducers outputs to reconstruct 5 mode channels, so the system is overdetermined. In case of a real detector in the presence of significant noise and system asymmetry the reconstruction of mode channels is not trivial.

Another approach to B matrix reversal

In this work we use another way of inverting the pattern matrix, that does not involve relying on any particular transducer placement symmetry. The same approach is used when building a numerical model of the sphere in [32]. Besides the 5 quadrupole modes, coupled to the gravitational waves, we also include a monopole mode, so the equation (1.13) becomes

$$\mathbf{B}_{mj} = Y_{1..5}(\theta_j, \phi_j) + \frac{\mathbf{I}_6}{\sqrt{4\pi}}. \qquad (1.47)$$

We have included a 6-th column to the matrix $\mathbf{B}$ so it becomes 6×6 invertible matrix. In principle, we could have included any of the sphere modes into the analysis, but the advantage of the monopole mode is that it is orthogonal to the quadrupole modes, so the mode channels are still uncorrelated. The frequency of the monopole mode is roughly twice the frequency of the first quadrupole modes, so its coupling to the transducers is very weak. But it does not matter since we do not actually use the monopole mode in the detector's data analysis, as it is only included to make the pattern matrix invertible and is excluded in the further calculations. However, it can be potentially used to test the alternative theories of gravity [22].

Noise temperature of the detector

The performance of resonant gravitational wave detectors is often compared by their sensitivity to the burst gravitational wave signal. For a given strain amplitude of a gravitational wave $h(\omega)$, the energy deposited to the resonator is [23]

$$E^{GW} = \frac{c^3}{16\pi G}\omega^2 |h(\omega)|^2 \Sigma, \qquad (1.48)$$

where G is the gravitational constant, c is the speed of light and Σ is the energy cross section of the detector Σ given by

$$\Sigma = \frac{G\rho V_S^5}{c^3 f_0^3}\Pi, \qquad (1.49)$$

where , ρ and V_S^5 are the density and the sound velocity of the detector material. Π is the reduced energy cross section which depends on the geometry of the detector and the Poisson ratio of its material. For MiniGRAIL $\Pi = 0.215$.

   If E^{GW} is the energy deposited by gravitational wave, then we can express the signal-to-noise ratio of a single-channel detector as [30]

$$SNR = \frac{E^{GW}}{k_B T_n}, \qquad (1.50)$$

where T_n is the detector noise temperature for pulse detection. A spherical detector has five independent mode channels and the total SNR of a spherical detector is a sum of the SNR of the mode channels

$$SNR = \sum_{m=1}^{5} SNR_m = \frac{E_{tot}^{GW}}{k_B T_n}, \qquad (1.51)$$

where E_{GW}^{tot} is the total energy deposited in the sphere. Here we assume that he noise temperature of the mode channels is equal.

It can be shown that for the same noise temperature the spherical detector has a sky averaged signal-to-noise ratio about 40-50 times higher than a bar of equivalent size [30, 13].

Simulated sphere response to calibration excitation

An experimental way of measuring a transfer function in section 1.2.4 relies on the assumption that the real sphere behaviour is the same as the one of an ideal sphere and we can use the spherical harmonics model described in section 1.1.2. A good way to test the validity of the model is to try to solve the inverse problem of direction reconstruction.

Since there are no known sources of gravitational waves, we have to use the calibrators to excite the sphere. Once again, we can convert the signal from the transducers to the mode channels and build the response matrix $\mathbf{A}$. To estimate the direction of the excitation we calculate the eigenvectors and eigenvalues of $\mathbf{A}$. Depending on the number of calibrators installed we can either use a set of calibrators to simulate the gravitational wave excitation or use a single calibrator to apply a radial impulse excitation on the surface of the antenna.

The major difference of the impulse excitation from a gravitational wave excitation is the shape of the deformation ellipsoid.

The calibration impulse will excite the set of a spherical harmonics defined by a pattern vector at the calibrator's position

$$\mathbf{a} \propto \mathbf{Y}(\phi_c, \theta_c)\mathbf{F_c}, \tag{1.52}$$

where $\mathbf{F_c}$ is the force that calibrator applies on the surface of the sphere. The "calibration" deformation ellipsoid has maximum radial deviation at the location of the impulse, and two radial deviations in the orthogonal directions having opposite sign and half amplitude. Therefore, the location of the impulse is given by the eigenvector with the largest eigenvalue.

For the gravitational wave coming from the same direction the amplitudes of the spherical harmonics are related to the gravitational wave strain amplitudes by means of $\mathbf{T_V}$ matrix

$$\mathbf{a} \propto \mathbf{h_m} \propto \mathbf{T_V} \begin{pmatrix} h_+ \\ h_\times \end{pmatrix} \tag{1.53}$$

Since gravitational wave strain field is orthogonal to the propagation direction, the resulting deformation ellipsoid will have a zero amplitude in the wave direction and equal nonzero amplitudes in the orthogonal directions.

We have performed the tests both on a simulated and on the real MiniGRAIL sphere. To see if the suspension influences the shape of the quadrupolar modes, we have simulated the behaviour of both ideal and suspended spheres. First we have performed the simulation by Finite Element Analysis (FEA) software Pro/ENGINEER Mechanica [33]. The elastic properties of the sphere were set to match the properties of $CuAl6\%$ alloy.

As we already mentioned in section 1.1.2 the quadrupolar modes of an ideal sphere are degenerate. This is also true for simulation of an ideal sphere, but for a sphere with a hole they are not degenerate, but are grouped in into two doublets and a singlet. First doublet ($2973.58\,Hz$, $2973.71\,Hz$) corresponds to modes Y_1, Y_2, second ($2990.77\,Hz$, $2990.85\,Hz$) to Y_3, Y_4 and the singlet ($3006.00\,Hz$) corresponds to Y_5 mode. This results agree very well with the results obtained on a real TIGA prototype [19].

In the simulation we did a series of tests where we applied the radial force at different points of the sphere surface and recorded the surface displacement at transducers position. First two tests were made on a model of an ideal sphere with TIGA and MiniGRAIL (see section 1.3.2) transducers layout. The third test was performed on a suspended sphere with TIGA transducers arrangement.

Figure 1.7: Calculated locations of the excitation points for an ideal sphere and a sphere with the suspension hole.

Recorded time series were further processed with Matlab [34] scripts. For inversion of the pattern matrix in TIGA arrangement we used the corresponding model described in section 1.2.4. For MiniGRAIL layout we used an approach from section 1.2.4

From equation (1.4) we can see that some spherical harmonics might have a zero amplitude for a particular excitation direction. For instance, the excitation from the top of the sphere ($\phi = 0^o$, $\theta = 180^o$) will only excite Y_5 mode. We have performed

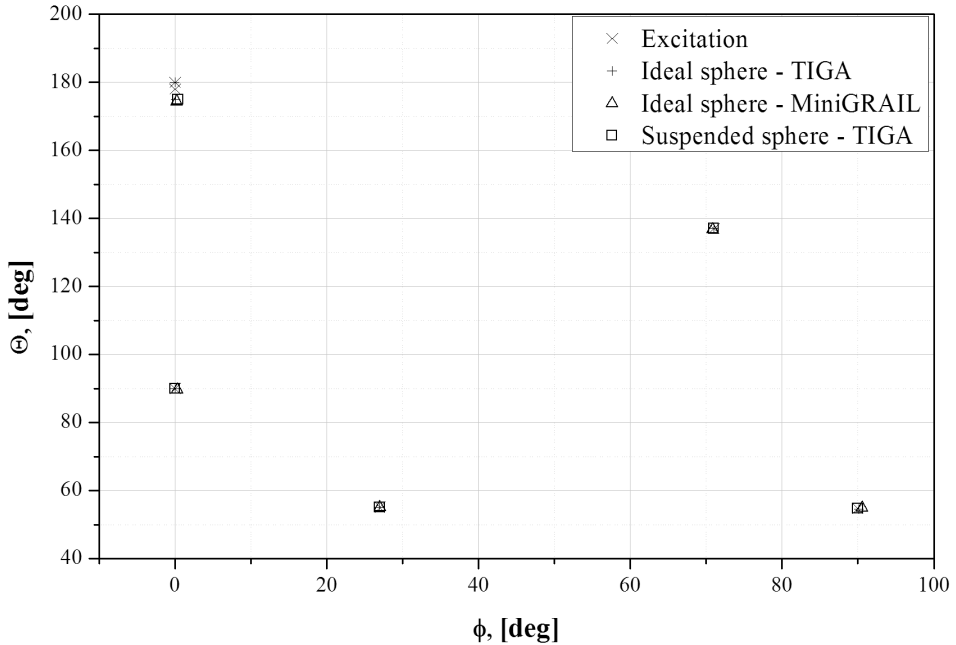|	Excitation		Ideal sphere TIGA		Ideal sphere MiniGRAIL		Suspended sphere TIGA	
#	ϕ	θ	ϕ	θ	ϕ	θ	ϕ	θ
1	0	180	0	179,9658	0	179.9573	-	-
2	0	90	0,0342	89,9306	0,0221	89,9687	0,318	89,6016
3	90	54,74	90,1441	54,5145	90,0095	54,7612	90,564	54,8575
4	0	178	0,1188	175,001	0,4401	174,9991	0,2395	174,3737
5	27	55	26,9986	55,0003	26,998	54,9991	27,0093	55,0869
6	71	137	70,9883	137,0039	70,9907	137,0021	70,8528	136,7879

Table 1.1: Calculated locations of the excitation points for an ideal sphere and a sphere with the suspension hole.

a simulation for a total of 6 points, with 4 of them only exciting only a subset of 5 quadrupolar modes and 2 arbitrary points exciting all the modes. The result of the direction reconstruction for 6 excitation points is shown on figure 1.7 and table 1.1.

The expected and calculated values of the spherical harmonics amplitudes are shown in table 1.2. The amplitudes of the modes are normalized so that the highest amplitude is set to 1.

As we can see from the simulations, the direction reconstruction algorithms, that rely on the model of the ideal sphere are also working perfectly for the suspended sphere. As for the real MiniGRAIL setup we have discovered that its behaviour is substantially different from the theoretical model. However with some modifications we were able to calculate the direction of the calibration pulse. We will discuss the results in the chapter 4.

1.3 MiniGRAIL

In the rest of this chapter we will focus on the actual design of the MiniGRAIL detector.

From equation (1.49) we see that the energy cross section of the detector is proportional to ρV_S^5, so it can be improved by using high-density, high-sound-velocity materials. After considering many possibilities [35] we have chosen a $CuAl6\%$ alloy because of its high mechanical quality factor ($Q \sim 10^7$ at low temperature) and a high sound velocity ($V_S \simeq 4100$ m/s). Unlike aluminium alloys which yield even higher Q, $CuAl$ does not become superconducting and demonstrates a good thermal conductivity at low temperature, allowing to cool a sphere below 100 mK [36]. It is also not toxic like Be alloys.

The sphere has a diameter of 68 cm, a mass of about 1.4 ton and the frequencies of spheroidal quadrupolar modes around 2980 Hz at 4.2 K. The general scheme of a MiniGRAIL setup is shown on figure 1.8.

The goal of the project is to operate MiniGRAIL at a thermodynamic temperature of 20 mK, equipped with six transducers coupled to nearly quantum limited double-

	Y1	Y2	Y3	Y4	Y5
1. $\phi = 0$, $\theta = 180$					
a.	0	0	0	0	1
b.	2.0E-4	-6.0E-4	-5.0E-4	9.0E-4	1
c.	1.0E-4	4.0E-4	1.3E-3	3.0E-4	1
d.	–	–	–	–	–
2. $\phi = 0$, $\theta = 90$					
a.	1	0	0	0	$-\frac{1}{\sqrt{3}} \approx -0.5774$
b.	1	0.0012	-0.0038	-0.0024	-0.5774
c.	1	0.0008	0.0032	0.0011	-0.5774
d.	1	0.0111	4.0E-4	0.014	-0.5833
3. $\phi = 90$, $\theta = 54.7356$					
a.	$-\frac{1}{\sqrt{2}} \approx -0.7071$	0	1	0	0
b.	-0.7065	-2.4E-3	1	-4.1E-3	9.7E-3
c.	-0.7069	-1.0E-3	1	1.0E-3	-1.3E-3
d.	-0.7126	-1.2E-2	1	-1.3E-3	-2.3E-3
4. $\phi = 0$, $\theta = 178$					
a.	1.1E-3	0	0	-0.0605	1
b.	6.7E-3	1.3E-3	-2.0E-4	-0.1521	1
c.	6.6E-3	5.0E-4	1.2E-3	-0.1521	1
d.	2.6E-2	1.0E-3	-6.0E-4	-0.1697	1
5. $\phi = 27$, $\theta = 55$					
a.	0.4711	0.6484	0.5095	1	-0.009
b.	0.4711	0.6483	0.5095	1	-0.009
c.	0.4711	0.6482	0.5095	1	-0.009
d.	0.4757	0.6510	0.5137	1	-0.011
6. $\phi = 71$, $\theta = 137$					
a.	-0.3886	0.3036	-1	-0.3443	0.3701
b.	-0.3884	0.3037	-1	-0.3445	0.3702
c.	-0.3884	0.3037	-1	-0.3445	0.3702
d.	-0.3940	0.3102	-1	-0.3479	0.3659

Table 1.2: Spherical harmonics amplitudes. a - calculated form the elastic model of an ideal sphere, b,c - from FEA of ideal sphere, d - from FEA of the sphere with hole

stage SQUID amplifiers [37].

1.3.1   Mechanical vibration insulation system and cryogenics

The sphere is suspended from the center with a 20 mm gold-plated copper rod. The rod is connected to the last mass of the mechanical vibration isolation system which consists of seven mass-spring stages suspended from the top of the Dewar. The first four masses are made of $CuAl6\%$ hanging from three steel ring springs. The lower three masses are made of copper, and are connected with gold-plated copper rods. Each stage acts as a mechanical low pass filter with cut-off frequency around 120 Hz and a resulting attenuation at the resonance frequency of the sphere of about 50 dB
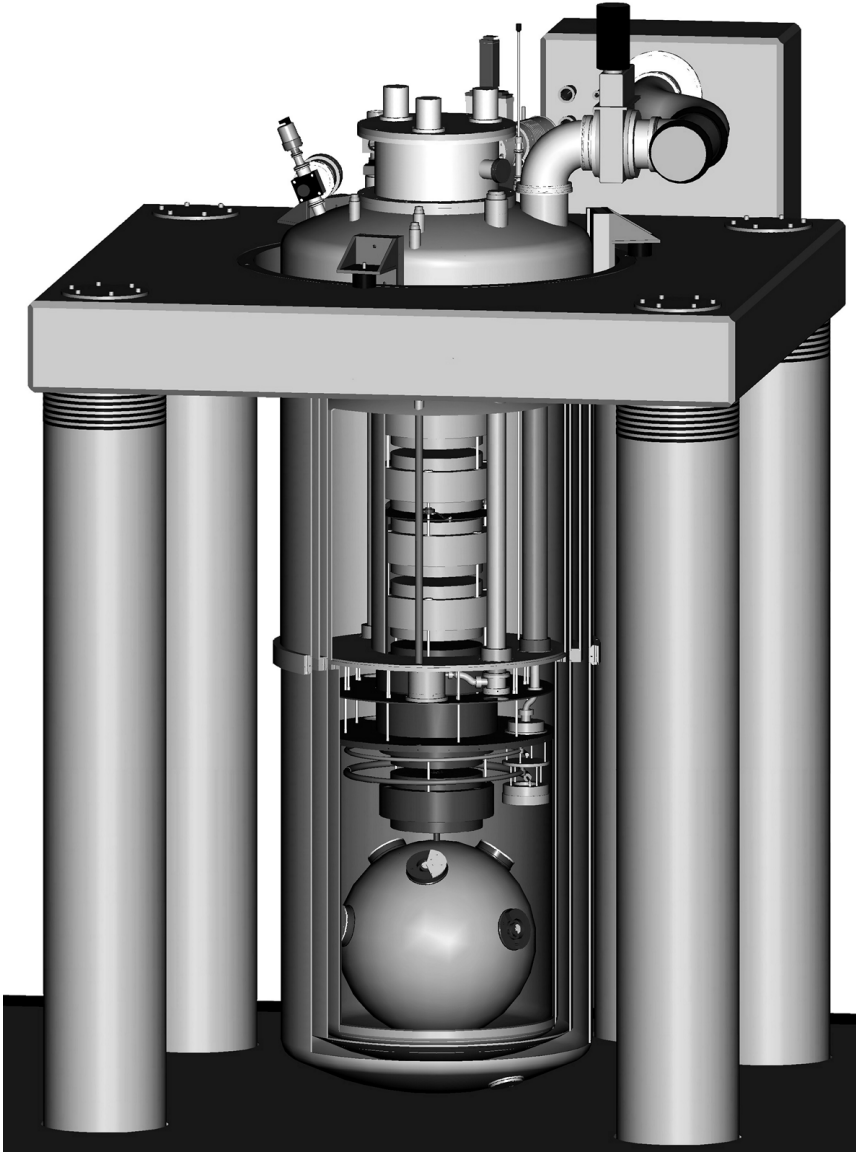
Figure 1.8: Schematic picture of the MiniGRAIL set up. The sphere is suspended from a vibration insulation stack consisting of a seven mass-spring stages. A dilution refrigerator is installed for cooling the sphere to cryogenic temperatures. Six resonant transducers are placed on the sphere.

per stage [38], [39]. The overall attenuation is estimated to be over 350 dB.

The sphere with the vibration insulation system is suspended in vacuum inside the cryogenic Dewar. 340 L liquid helium and 200 L nitrogen baths are located in the upper part of a Dewar. The lower part has no cryogenic liquids, and contains radiation shields, attached to nitrogen, helium baths and to Still and 50 mK plates. The Dewar is installed on a platform placed on a concrete island which is mechanically decoupled from the laboratory building.

A dilution refrigerator is used to cool the sphere below 4.2 K. The last three copper masses are thermally coupled to a mixing chamber. Is is naturally very important to have a very good thermal link between the mixing chamber and the sphere in order to reach the lowest temperatures. On the other hand is is also important to maintain a low mechanical coupling, so that the low thermal noise of the sphere would not be spoiled by the mechanical vibrations coming from the dilution refrigerator. We have made a very soft annealed copper "Jellyfish" link(see figure 1.9(b)), that connects the mixing chamber to a suspension mass 5. Three stages of suspension and a soft thermal link effectively decouple the sphere from vibrations of the dilution refrigerator.

The two upper CuAl masses 4 and 3 are coupled to 50 mK and Still plates respectively by means of the similar soft thermal links.

During the previous runs the minimal reached temperature of the sphere was 67 mK with a temperature gradient between the mixing chamber and the sphere of about 20 mK. With a new, more powerful dilution refrigerator unit installed recently we expect reaching even lower temperatures.
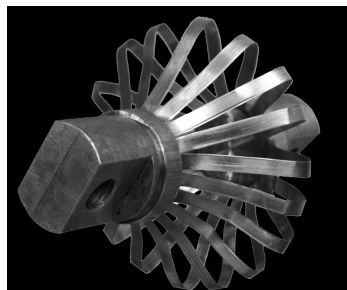
1.3.2   Transducers

The picture of the MiniGRAIL sphere with transducers and calibrators mounted are shown on figure 1.10. Because of the limited spacing inside the Dewar the three lowest transducers were placed at polar angle of 67.8^o - higher than TIGA's 79.1876^o. the upper transducers are placed at a proper TIGA angle of $\theta = 37.3773^o$. The azimuthal angles are the ones of TIGA arrangement. The difference in the inclination angle is certainly above the tolerance of a TIGA model [21], so in all future calculations we will use a 6×6 pattern matrix with included monopole mode. We have also placed 6 mass-loaded PZT calibrators at the same θ angles as transducers but shifted by 60° in azimuthal angles. The seventh calibrator is placed at an arbitrarily selected position of $\phi = 33^o$, $\theta = 51^o$ and is used to test the direction reconstruction algorithms. The shiny cylindrical boxes attached to the last suspension mass are housings for the superconducting transformers and SQUID modules. They are made from led-plated copper and covered with cryoperm foil for electromagnetic protection.

1.3.3   Strain Sensitivity

MiniGRAIL strain sensitivity measured with one transducer during run 6 (first sensitivity run) is shown on figure 1.11. The transducer was charged to 200 Volt and the sphere thermodynamic temperature was about 5 K.
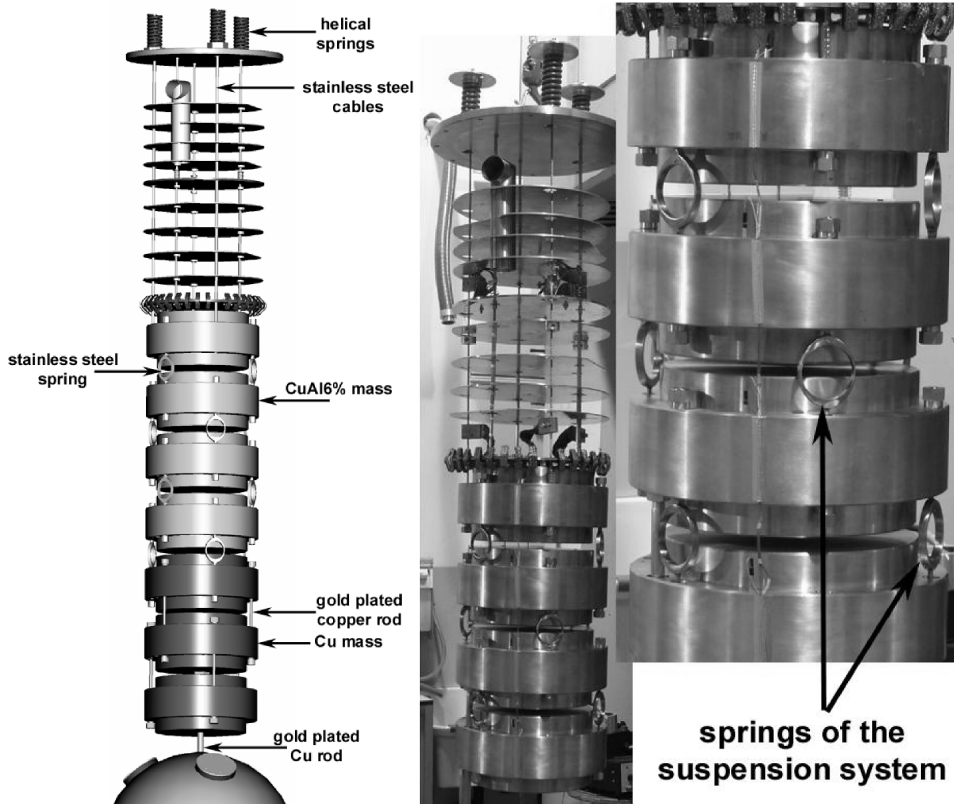
(a)

(b)

Figure 1.9: (a) - MiniGRAIL vibration insulation system.(b)- a soft "Jelly-fish" link used to thermally couple the sphere to the dilution refrigerator.
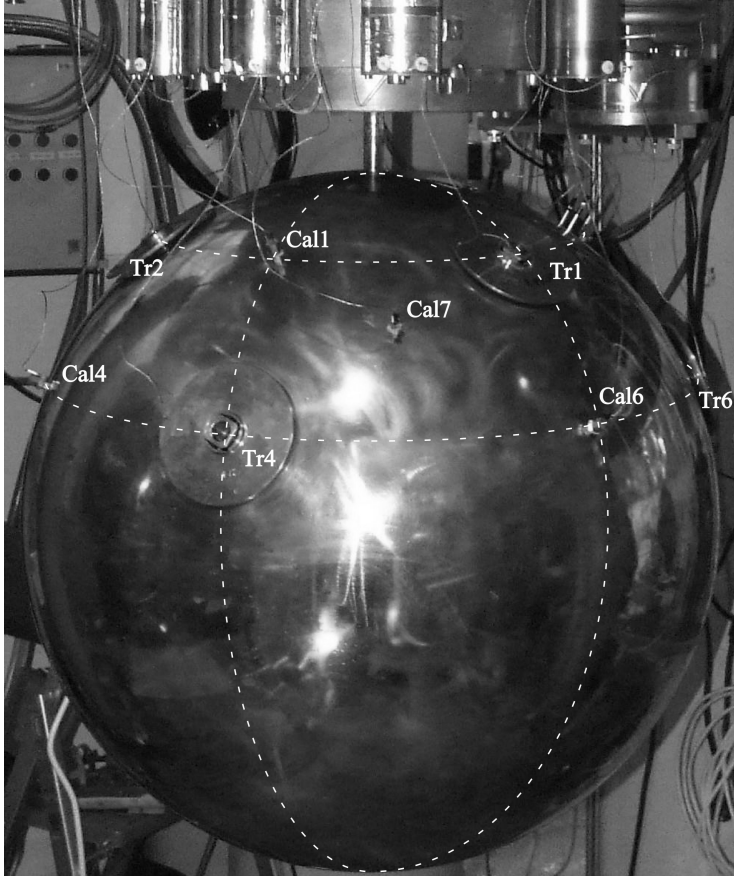
Figure 1.10: MiniGRAIL sphere with all transducers and calibrators installed. Transducers are placed in TIGA configuration and 6 calibrators are are placed at the same polar angles as transducers but shifted by 60° in azimuthal angles. Calibrator 7 is installed at ($\phi = 33^o$, $\theta = 51^o$)

We reached a peak strain sensitivity of $(1.5 \pm 0.6) \cdot 10^{-20} Hz^{-1/2}$ at $2942.9\,Hz$ and a strain sensitivity of about $5 \cdot 10^{-20} Hz^{-1/2}$ over a bandwidth of $30\,Hz$. This correspond to a strain amplitude of $h \simeq 2.5 \cdot 10^{-18}$ at $3\,kHz$ for a burst signal of $1\,ms$ [12]. For a sphere of $68\,cm$ in diameter like the one of MiniGRAIL, it is equivalent to a displacement sensitivity, at $3\,kHz$, of $1.6 \cdot 10^{-19}\,m$. From equation (1.50) we estimate that the detector is sensitive to a burst signal with an impulse energy of about $T_N \sim 50\,mK$. This sensitivity would be enough to detect supernova explosions in our galaxy. The expected event rate, however, is only a few per century. To increase the event rate to at least several per year, it is necessary to improve the sensitivity to $S_{hh_{min}} \leq 10^{21}$ and reach the Virgo cluster of galaxies, which is at a distance of
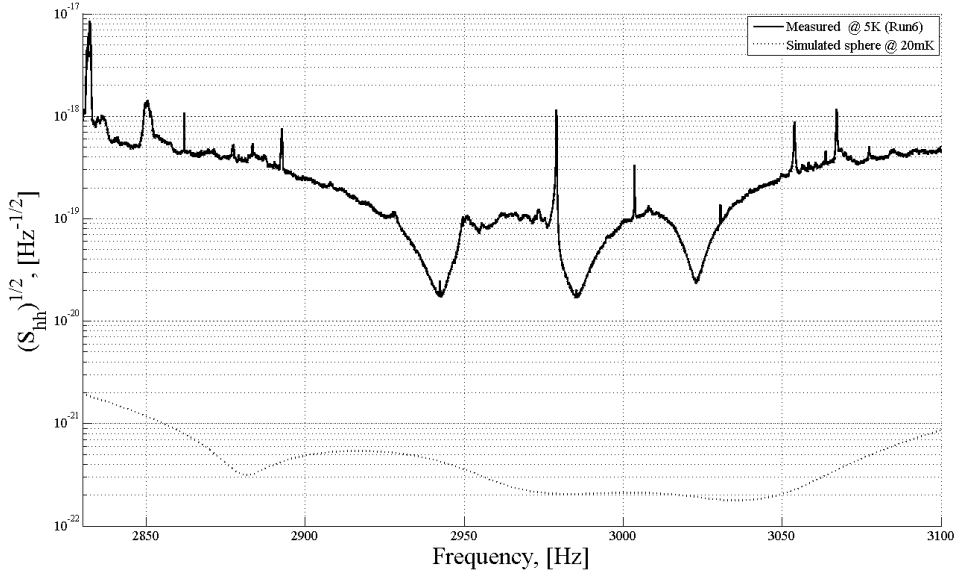
Figure 1.11: MiniGRAIL strain sensitivity measured at sphere temperature of 5K during cool-down in 2005 [25](solid line) and estimated average sky sensitivity using the model of the sphere with 6 transducers at temperature of 20 mK [40](dotted line)

$\sim 15 Mpc$ (1 parsec $= 3.09 \times 10^{13}$ km). The estimated sensitivity for the next run on figure 1.11 is able to reach the desired level. The sensitivity is calculated using the model of the sphere presented in section 1.2.2.The model assumes that 6 transducers are placed in TIGA configuration and read out by 2-stage SQUID amplifier. The properties of the readout chain components were taken close to the realistic ones as for the status of MiniGRAIL in 2009 [32]. The thermodynamic temperature of the sphere was set to 20 mK.

Chapter 2

MiniGRAIL data acquisition system

Introduction

In the previous chapter we have shown that for full omnidirectional operation of MiniGRAIL a simultaneous data from 6 transducers has to be acquired. In the current chapter we describe the acquisition system that was developed for a full featured MiniGRAIL operation.

We have set up the 8-channel acquisition system using a PC with 24-bit National Instruments NI 4472-PCI analog-digital converter(ADC) card. The acquired data is saved over the network to a 4TB RAID5 storage system. A GPS clock is used for precise timing of the acquisition.

The acquisition libraries are written in c/c++ and user interface modules are written in c#. Software to monitor the the dilution refrigerator operation and less important auxiliary acquisition modules are made in LabView [41]. The preprocessing of the acquired data is done in Matlab [34]. The full data processing pipeline is being developed by a group in the university of Geneva[31]. We have also developed scripts that allow the synchronization of the acquired data with the university of Geneva.

A summary of key acquisition system parameters is given below:

- 6 capacitive transducers, read out by 6 double stage SQUIDs are installed on the sphere for omnidirectional data analysis.

- SQUIDS are controlled by commercial 8-channel SQUID electronics [42]

- 24 bit 8 channel analog-digital converter (NI 4472-PCI)(one channel is reserved for GPS timing) is used to digitize the data.

- Timing is done with a GPS system: Trimble Accutime 2000 ($\pm 25\,ppm$ accuracy)

- Acquisition frequency: $\approx 20\,kHz$

- Data rate is 80 KB/s ($\approx 275\,MB/h$) per channel

If we are doing a full seven channel acquisition, the amount of data acquired per day is approximately $45\,GB$. This would probably not impress the high energy physicists and astronomers, but for a laboratory scale experiment it is not usual. We have set up a $4\,TB$ RAID5 NAS (Network Attached Storage) to store the data. With the current capacity it is enough to store about 3 months of MiniGRAIL data.

To maintain the stability of the main (fast) acquisition system we do not perform any tasks on the acquisition PC, but we have set up a second acquisition PC with a 16-bit National Instruments NI PCI-6034E ADC card which used to monitor the SQUIDs noise and working point and for calibration purposes.

Since cosmic rays can also excite the MiniGRAIL sphere, a cosmic ray detector, which is a part of HiSparc [43] project, is installed on the laboratory roof above MiniGRAIL. The data from the detector is also recorded with precise GPS timing and can be combined with MiniGRAIL data for vetoing the cosmic rays events. As we already know, the unique property of MiniGRAIL is that unlike the bar detectors, the spherical detector reacts differently to the gravitational waves and cosmic rays, so it is possible to distinguish these perturbation by looking at different sphere modes [15].

2.1   Data acquisition

2.1.1   Hardware

The general scheme of the acquisition system is shown on fig. 2.1 To improve the reliability the acquisition system is split into few independent parts each of them running on separate PC's

Further in this chapter we will take a closer look at each component of the system.

SQUID amplifier

Even amplified by the resonant transducer, the signal coming from the sphere is very weak. This puts very high requirements on the amplifiers we need to use. It should have very low intrinsic noise and be placed as close to the transducer as possible. A dc SQUID amplifier is likely an ideal solution - it is one of the most sensitive magnetic flux-to-voltage converters and it works the best at ultracryogenic temperatures. Operation principle and design of the dc SQUIDs are widely described in literature, so we will only give here a short introduction.

SQUID operation is based on the effect of tunnelling of Cooper pairs through an insulating barrier (a junction) between two superconductors, which was predicted by B. Josephson in 1962 [44]. Josephson showed that the current I flowing through a junction is given by
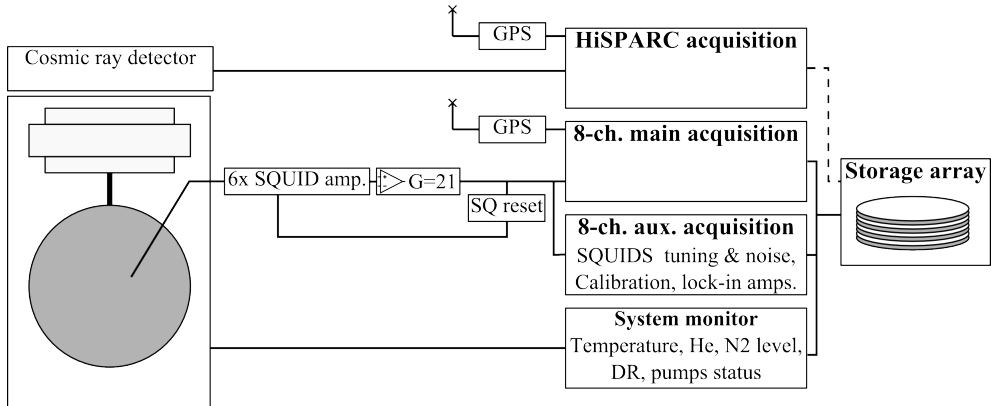
$$I = I_0 \sin(\delta) \tag{2.1}$$

Figure 2.1: Acquisition system of MiniGRAIL. Besides the main acquisition system which is used to digitize and store the signal from 6 transducers we have set up an auxiliary acquisition used to do the SQUIDS monitoring and calibration without disturbing the main system. A separate PC is used to monitor system parameters like temperature, dilution refrigerator operation, etc. The data of MiniGRAIL and HiSparc can be synchronized by using a GPS timing

where $\delta = \phi_1 - \phi_2$ is the difference between the phases ϕ_1 and ϕ_2 of the condensates in the two superconducting electrodes and I_0 is the maximal supercurrent (critical current) through a junction. If a voltage V is applied between the superconducting electrodes, the phase difference evolves in time as

$$\frac{d\delta}{dt} = \frac{2\pi}{\Phi_0}V = 2\pi f_J, \tag{2.2}$$

where $\phi_0 = h/2e = 2.07 \times 10^{-15}$ Wb is the magnetic flux quantum and $f_J = \frac{V}{\Phi_0} = 483\frac{MHz}{\mu V}V$ is called the Josephson frequency. From equations (2.1) and (2.2) we see that in zero voltage state the phase difference is constant in time and the current through the junction can not exceed I_0. If $V > 0$ the current starts oscillating with the Josephson frequency. A high-quality tunnel junction has a hysteretic current-voltage characteristics. As the current through the junction (a bias current) is increased from zero, the voltage switches to a non-zero value when I_b exceeds I_0, but returns to zero only when the current is reduced to a value much less than I_0. This hysteresis can be eliminated by shunting the junction with an external shunt resistance. The current-voltage characteristics of such junctions is well explained by the resistively- and capacitively-shunted junction (RCSJ) model [45].

A SQUID amplifier consists of two Josephson junctions connected in parallel and forming a superconducting loop. A schematic of a dc SQUID is shown on figure 2.2. A junction is conventionally represented on schemes with a cross symbol. An insulating barrier between the superconductors forms a capacitance C parallel to the junction.
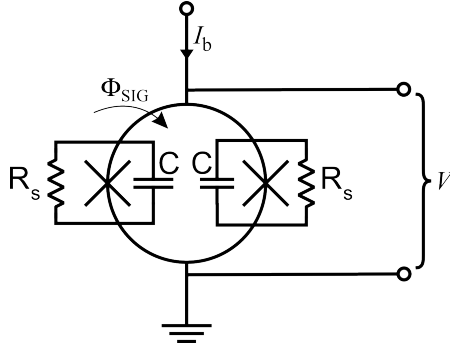
Figure 2.2: Scheme of a dc SQUID. The crosses represent the Josephson junctions of capacitance C. Shunt resistors R_s across the junctions are used to remove hysteresis.

Shunt resistor R_s are added to remove the junction hysteresis. The hysteretic behaviour of the junction is characterized by McCumber parameter $\beta_c = \omega_J R_s C$. If $\beta_c < 1$, the I-V characteristic of the Josephson junction is non-hysteretic and if $\beta_c > 1$, the junction shows hysteretic behavior. For the SQUIDs we use, β_c is always less then one.

The change of flux through the SQUID loop modulates its critical current with a period of Φ_0. The two extremal I-V curves are shown on figure 2.3(a). The modulation depth of the critical current is given by

$$\Delta I_c \approx \frac{1}{1 + \beta_L} 2I_0, \tag{2.3}$$

where the screening parameter β_L is

$$\beta_L = \frac{2I_0 L_{SQ}}{\Phi_0} \sim 1. \tag{2.4}$$

If we bias a SQUID with a constant current $I_b > 2I_0$, the resulting voltage V across a dc SQUID will be a periodic function of external magnetic flux Φ_{sig} as shown on figure 2.3(b).

The maximum gain of the SQUID $V_{\Phi_{max}}$ is estimated as

$$V_{\Phi_{max}} \equiv \frac{\partial V_{max}}{\partial \Phi} = \frac{2\beta_L}{1 + \beta_L} \frac{R}{L_{SQ}}. \tag{2.5}$$

Noise of a SQUID amplifier

In chapter 1 we have already introduced the noise of a SQUID amplifier. Its origin is the Johnson noise of the shunt resistor given as

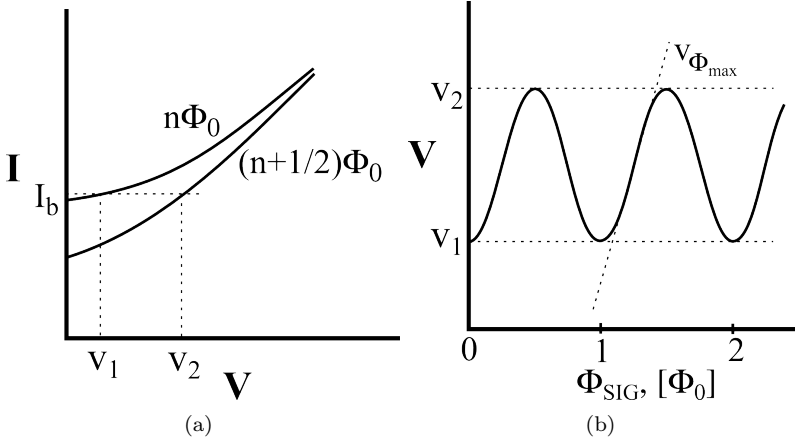$$S_V(\omega) = 4k_B T R_s \tag{2.6}$$

Figure 2.3: $I - V$(a) and $V - \Phi$(b) characteristics of a dc SQUID.

The spectral density of a voltage noise at the output of a dc SQUID is given by

$$S_{VV} = \gamma 2 S_I R_{dyn}{}^2 \sim \gamma_{VV} k_B T R_s, \tag{2.7}$$

where $R_{dyn} \sim R_s/2$ is the dynamic resistance of the SQUID. The resistors also generate a circulating current noise in the SQUID that induces noise into any input circuit coupled to it. Its spectral density is given by

$$S_{JJ} = \gamma_{JJ} \frac{k_B T}{R_s}. \tag{2.8}$$

A cross correlation between voltage and current noise contributes as well to the total noise in the SQUID with a spectral density of

$$S_{JV} = \gamma_{JV} k_B T. \tag{2.9}$$

The coefficients $\gamma_{VV}, \gamma_{JJ}, \gamma_{JV}$ arise from the fact that Johnson noise is generated at frequencies around the Josephson frequency f_J is mixed down to the measurement frequency by the Josephson oscillations and the inherent non-linearity of the junctions. These can be numerically evaluated as $\gamma_{VV} \sim 16$, $\gamma_{JJ} \sim 11$, $\gamma_{JV} \sim 12$ [26].

For uncoupled SQUID only the the S_{VV} term gives noticeable contribution to the noise. If the SQUID is connected to the input circuit, both current and voltage terms couple back to the input coil as described in equation (1.34) of section 1.2.2.

Using equation (2.5) and equation (2.7), the flux noise spectral density at the input of the SQUID can be calculated as

$$S_\Phi = \frac{S_{VV}}{V_{\Phi_{max}}^2} \sim \gamma_{VV} \frac{k_B T L_{sq}{}^2}{R_s} \left(\frac{1 + \beta_L}{2\beta_L}\right)^2. \tag{2.10}$$

This equation is valid for $\beta_L \sim 1$.

A convenient way to compare the sensitivity of different SQUIDs is in terms of the noise energy per unit bandwidth or energy resolution:

$$\epsilon = \frac{S_\Phi}{2L_{sq}} = \gamma_{VV} \frac{k_B T L_{sq}}{2R_s} \left(\frac{1+\beta_L}{2\beta_L}\right)^2 \tag{2.11}$$

According to equation (2.11), the energy resolution can be improved by decreasing the SQUID inductance L_{sq} and/or the operating temperature T. The limit in decreasing L_{sq} is given by the increasing of the impedance mismatch to a conventional signal source, which might have a few μH of internal inductance. Moreover, the intrinsic energy sensitivity of a dc SQUID is inversely proportional to the critical current density of the junctions if the parameters β_L and β_C are about 1. When $\beta_L \sim 1$, the energy resolution becomes $\epsilon = \gamma_{VV} k_B T \Phi_0 / 4R_s I_0$. This means that increasing the critical current, while keeping $\beta_L, \beta_C \sim 1$ is another procedure to minimize the dc SQUID intrinsic noise [46].

SQUID readout

While being one of the most sensitive magnetic flux-to voltage converters, the SQUID amplifiers do not have a very high gain. Given typical parameters of resistively shunted dc SQUID, the resulting flux to voltage transfer is of the order of $\frac{\partial V}{\partial \Phi} = 100\,\mu V/\Phi_0$ and the voltage swing is $2\delta V = V_1 - V_2 \sim 30\,\mu V$. The wideband flux noise of the dc SQUID is typically around $1 - 2\mu\Phi_0/\sqrt{Hz}$. This corresponds to an output voltage noise of $0.1\,nV/\sqrt{Hz}$, which is about one order of magnitude smaller than the input voltage noise of typical low-noise room temperature preamplifiers. This problem can be solved by using a two stage SQUID system, when a second SQUID amplifies the sensor dc SQUID [47]. A scheme of 2-stage SQUID amplifier with a readout electronics is shown on figure 2.4.

Let us first look at the 2-stage SQUID configuration. A first (sensor) SQUID is biased at a constant voltage by sending a bias current I_{b1} through a small resistance $R_b \ll R_{dyn1}$ in parallel to the SQUID. In this mode, the SQUID acts as a flux-to-current converter, so the signal flux generated by current I_1 in the input coil is converted to a current I_2 in the input coil of the second (amplifier) SQUID. The flux gain G_Φ of 2-stage SQUID is given by

$$G_\Phi = \frac{\partial \Phi_1}{\partial \Phi_2} = \frac{M_2}{M_{dyn1} + R_b/V_\Phi}, \tag{2.12}$$

where $M_{dyn} = R_{dyn1}/V_\Phi$ is the intrinsic current sensitivity of the sensor SQUID. The flux gain should be sufficiently high, so the amplified flux noise of the sensor SQUID is larger than the noise contributions of the second stage and the room temperature readout electronics. Hence, in a well-designed two-stage SQUID system, the overall system noise is determined by the sensor SQUID.

Another problem it that since the flux-to-voltage characteristic of the SQUID is periodic, we can only operate the amplifier in a small dynamic range around the

steepest part of $V - \Phi$ curve where the voltage response is almost linear. For a dc SQUID the linear range is taken as $\frac{1}{4}\Phi_0$ [45]. By introducing the second stage SQUID we have further reduced the dynamic range of the amplifier by a factor of G_Φ. This limitation can be overcome by using a SQUID amplifier with a negative feedback (a flux locked loop). The voltage signal from the SQUID is amplified, integrated and sent to a feedback coil, coupled to the SQUID loop. A feedback resistor R_{fb} is used to convert the voltage at the output of the integrator to the current in the feedback coil. As a result the total flux through the SQUID $\Phi_1 + \Phi_{fb}$ is constant. By adjusting the bias voltage V_b we can change the dc flux in the feedback loop and tune the working point of the SQUID.
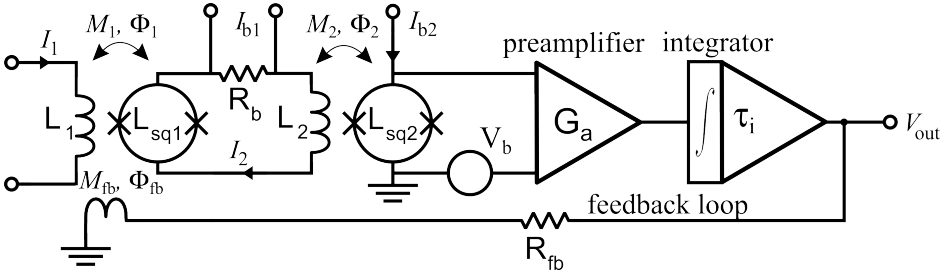

Figure 2.4: Scheme of 2-stage SQUID amplifier with a flux-locked loop circuit.

The voltage signal V_{out} at the output of the electronics is related to the signal flux as

$$V_{out} = \frac{G(\omega)}{1 + G(\omega)} \frac{R_{fb}}{M_{fb}} \Phi_1, \tag{2.13}$$

where $G(\omega)$ is called the open loop gain. For 2-stage SQUID it is

$$G(\omega) = G_\Phi V_\Phi G_a(\omega) \frac{M_{fb}}{R_{fb}}. \tag{2.14}$$

Since the open loop gain is high but finite, the flux through the SQUID is not really constant, but also includes some error ac flux $\Phi_{err} = \Phi_1 - \Phi_{fb}$. If Φ_{err} exceeds the linear range, the flux locked loop unlocks. A maximal slew rate (a speed of a flux change) that does not lead to SQUID unlocking is given by [48]

$$\frac{\partial \Phi_{SIG}}{\partial t} = \frac{\partial V G_a M_{fb}}{\tau_i R_{fb}}. \tag{2.15}$$

Preamplifier and automatic FLL reset circuit

Even after the room temperature electronics, the flux gain of the SQUID is in the order of $V_\Phi = 0.1 - 1\,V/\Phi_0$. Given that the SQUID noise spectral density at mK

temperatures $S_V < 1\,\mu\Phi0/\sqrt{Hz}$, the voltage noise spectral density at the output of the SQUID electronics can be well below $1\,\mu V/\sqrt{Hz}$. Typical commercial ADC converters, like the one used for MiniGRAIL, have an input noise spectral density of $\sim 100 nV/\sqrt{Hz}$, comparable with the signal from the SQUID. To eliminate the contribution of the converter noise we use a custom made 8-channel low-noise preamplifier with a fixed gain $G = 21$ and bandwidth $f_{-3dB} \approx 250$ kHz (figure 2.5(a)). We have measured the input noise of $\leq 6\,nV/\sqrt{Hz}$ for each preamp channel which is low enough not to introduce any noticeable extra noise in acquired data.

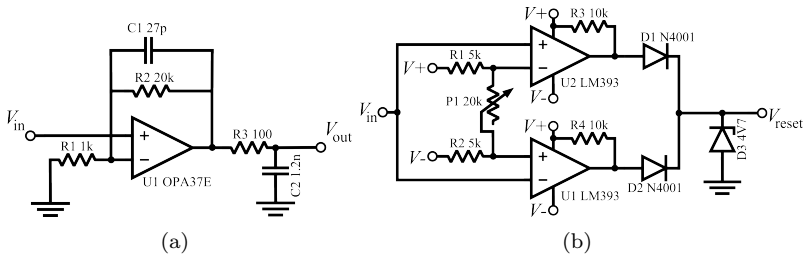(a)   (b)

Figure 2.5: Preamplifier (a) and SQUID electronics reset (b) circuits.

If the flux locked loop is working properly (SQUID is locked) the integrator in the feedback loop keeps the SQUID at zero flux, so the DC level at SQUID electronics output is close to zero. If the FLL fails, the negative feedback does not compensate the signal flux in the SQUID anymore and the integrator quickly saturates resulting in a high voltage signal at the output of the electronics. Often it is enough to reset the integrator to restore the FLL operation. The SQUID electronics we are using [42] is not able to detect the overload condition and do a self reset, but it has an external TTL reset input for each channel.

We have developed a simple circuit (figure 2.5(b)) which monitors the output voltage of the SQUID electronics(V_{in} on the schematics) and if its absolute value exceeds a threshold voltage (set by $P1$) the comparators $U1$ and $U2$ should set V_{reset} output to high level. Because a Zener diode $D3$ limits the output voltage to TTL compatible level, the supply voltage can vary in a range of $5 - 15$ V.

Digitizing the acquired data

Because the ADC input is an analog signal with an infinite number of possible states, and the output is a digital discrete signal, the digitized data is distorted compared to the measured analog signal. This error is called quantization noise and limits the maximal signal to noise ratio (SNR) of an ADC converter. For N-bit ADC the expression for SNR is well known [49]

$$SNR = 6.02N + 1.76\,dB. \tag{2.16}$$

The quantization noise is uniformly spread in the spectra up to the Nyquist frequency $f_{sampl}/2$. So there are two obvious ways to increase the SNR - increasing the resolution or increasing the sampling frequency. From eq. 2.16 we note that a factor of 4 oversampling is equivalent to increase of ADC resolution by only one bit, so the oversampling by itself is not very efficient technique. However there is a class of ADC converters which offers high resolution and SNR by using a low cost low resolution ADC and a smart oversampling technique - the sigma-delta converters [49]. The high oversampling rate of such converters comes at the cost of low sampling rate(typically in order of $100 - 200\,kS/s$), but for digitizing wide dynamic range low bandwidth signals, like MiniGRAIL acquisition data, the sigma-delta converters seems to be an ideal solution.

Sigma-delta ADCs have a number of unique features:

- Oversampling: Sampling the input signal at a frequency that is much higher then the Nyquist frequency simplifies the acquisition chain, because there is no need for using low pass filters on each channel to suppress aliasing. It also distributes the quantization noise over a higher bandwidth, improving the signal to noise ratio.

- Noise shaping: Noise shaping filter acts as a low-pass filter to the input signal and a high-pass filter to the quantization noise. Thus, most of the quantization noise is pushed into higher frequencies which are filtered out at the output thus improving the SNR.

- Digital filtering: Integrated digital filters are used to attenuate the signal outside the band of interest.

- Decimation filtering: The output of the sigma-delta converter is a 1-bit data stream at the oversampling rate. The purpose of the decimation filter is to extract information from this data stream and reduce the data rate to a more useful value.

For MiniGRAIL we use 8 channel 24 bit NI 4472-PCI Sigma Delta ADC available from National Instruments. The disadvantage of this particular ADC card is that it has no external clock input, so it is clocked by less accurate PC clock generator. To overcome this problem we acquire the signal from a stable GPS clock system and do the timing afterwards in software.

The digitized data is saved in a file together with a header, which provides the information about timing, acquisition and system parameters. The header is written in a plain text as *Parameter Name: Value* pair. The ADC data is converted to voltage and saved in a 32 bit floating point format. The file structure is shown on figure 2.6.

Storage system

A NAS system used to store MiniGRAIL data is a 64-bit Linux PC with a 4 TB RAID5 attached to it. RAID system consists of 12 400 GB hard disks. 10 of them are
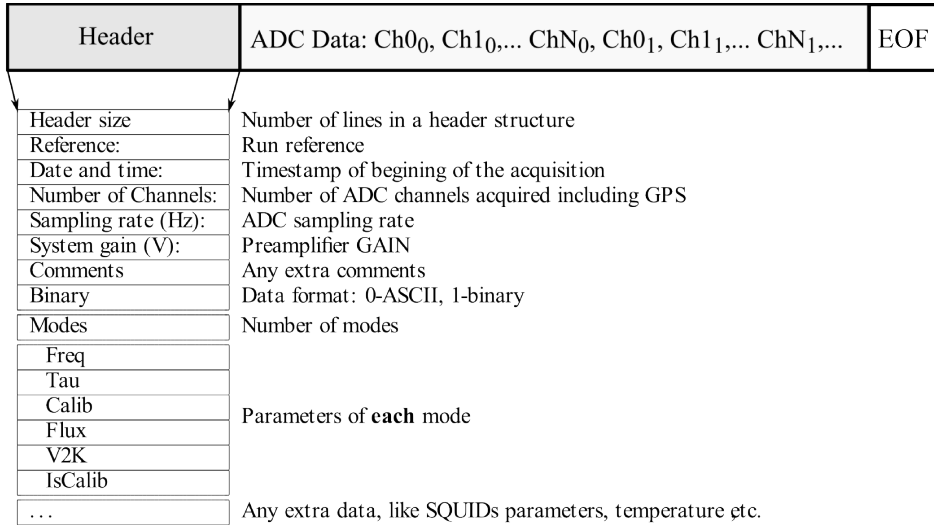
Header	ADC Data: $Ch0_0$, $Ch1_0$,... ChN_0, $Ch0_1$, $Ch1_1$,... ChN_1,...	EOF

Header size	Number of lines in a header structure
Reference:	Run reference
Date and time:	Timestamp of begining of the acquisition
Number of Channels:	Number of ADC channels acquired including GPS
Sampling rate (Hz):	ADC sampling rate
System gain (V):	Preamplifier GAIN
Comments	Any extra comments
Binary	Data format: 0-ASCII, 1-binary
Modes	Number of modes
Freq	
Tau	
Calib	
Flux	Parameters of **each** mode
V2K	
IsCalib	
. . .	Any extra data, like SQUIDs parameters, temperature etc.

Figure 2.6: MiniGRAIL data acquisition file structure

used to store the data and 2 are reserved for redundancy, resulting in a total storage capacity of 4TB. With constantly growing hard disk capacity and decreasing price the size of the array can be tripled for a total price of less than 1000 euros.

2.1.2   Software

The acquisition software consists of two modules. The acquisition module communicates with the hardware (acquisition card, GPS,data storage systems) and the second module provides user interface functionality, allowing to set the acquisition settings and view current system parameters.

Acquisition module

The acquisition module is written in C/C++ using National Instruments NI-DAQ libraries to communicate with the acquisition card and "NMEA 0183" protocol to read data from GPS receiver.

The acquisition is done using double buffering technique to protect data integrity - the data is stored in memory in a circular buffer, which is divided in two halves. The hardware is writing data in one half of the buffer while the software reads it from the other half. This technique introduces a delay in acquisition equal to $\Delta\tau_{acq} = L_{buf}/2f_{sampl}$, where L_{buf} is the size of a circular buffer in samples. But since all current MiniGRAIL data analysis routines are offline, this time delay is not an issue. The driver monitors the integrity of the buffer and generates an event on error. The

software handles this events and can restart the acquisition if an unrecoverable error occurs.

Since the acquisition system does not support external frequency generator input and the internal PC clock generator might not be accurate enough - one of the acquisition channels is always connected to GPS system PPS (Pulse Per Second) signal output. This is a high precision timed delta-like signal generated every second by GPS hardware.

When the acquisition is started it is initialized as follows:

1. Reading acquisition settings from use interface (UI) module

2. Initializing ADC card. Set buffer size, acquisition frequency, time, etc.

3. Get time stamp from GPS clock.

4. Start acquisition.

5. If data in the acquisition buffer is ready, read it.

6. Find the first PPS signal and start saving the data after that point

7. Correct the acquisition timing to account the skipped data

By using PPS as a trigger, the time of the acquisition start is defined and the timing of any data sample can be calculated from it. This is very important for later data analysis. In step 4 there is always a delay between the software command to start the acquisition and the hardware response. It depends a lot on the operation system and is not constant. It is possible to estimate it by measuring the time difference between just before the step 4 and after step 5.By subtracting the length of acquired data we can calculate the initialization delay. The measured value was stable around $150\,ms$ when the computer was only busy running the acquisition, but was very unstable, sometimes reaching more then one second delay, when the PC was under stress load.

Thus, we can state the delay to be always much less than one second, in normal operating conditions, so it is enough to discard the data before the second PPS signal and increase the time stamp, received from GPS by 1 second.

UI module

The user interface module is written in C# and provides a user friendly way to set acquisition parameters and current system properties. It allows to set the following acquisition parameters:

- Acquisition frequency.

- Acquisition buffer size.

- Acquisition time for one file

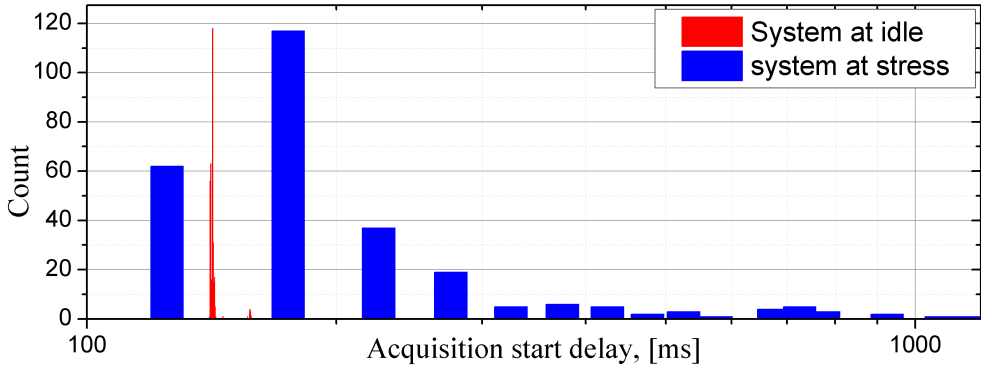- Total acquisition time or continuous mode.

Figure 2.7: Acquisition initialization delay for PC running only acquisition and under stress testing
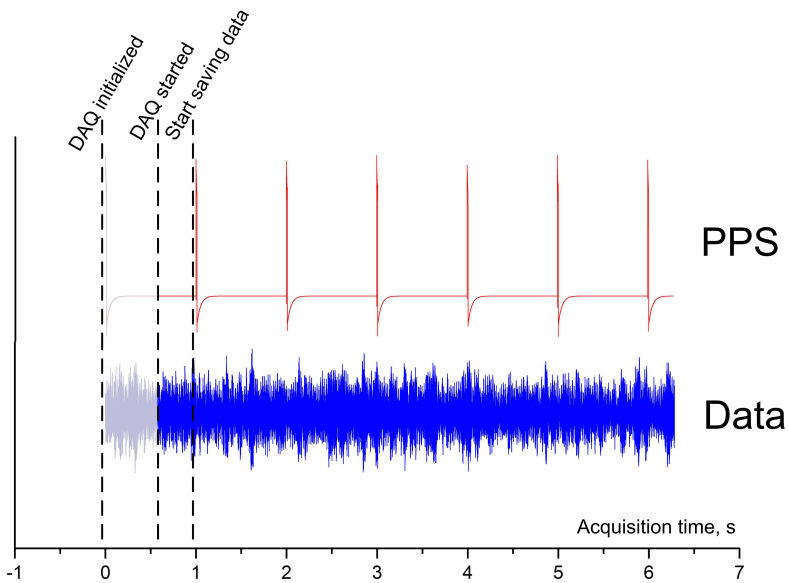

Figure 2.8: Acquisition system delay elimination

- Properties of the visible modes: frequency, quality factor, calibration constants.

- Properties of the read-out chain: SQUID parameters, preamp gain.

Module also displays the acquisition and error logs. The software also reacts to the error events generated by the ADC driver and can reinitialize the system and restart the acquisition.
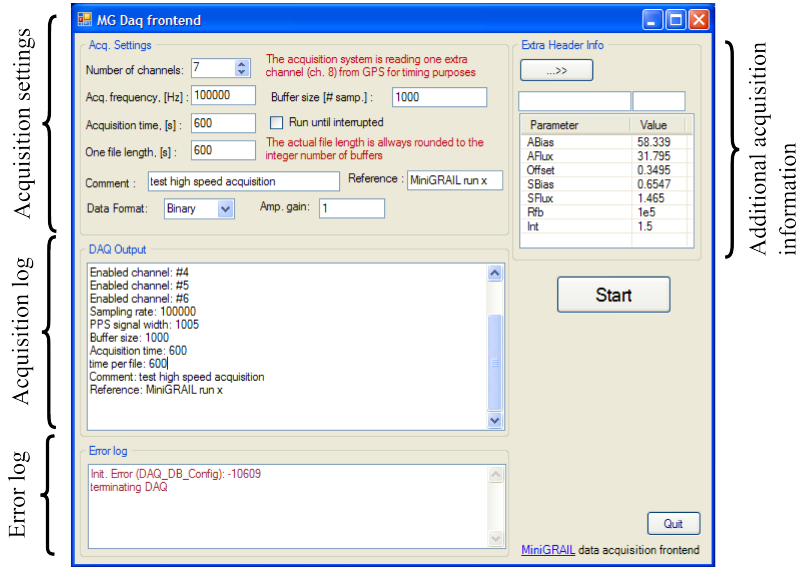
Figure 2.9: DAQ front end user interface

2.2   Data preprocessing

The data processing software is used to prepare the raw acquired data for data analysis. It can perform the following tasks:

- Filter out bad data. The filtering script scans through the acquisition files and calculates signal to noise ratio (SNR) of the resonant modes. If the SNR is below a certain threshold then the file is marked as bad data and not used in further data processing procedures.

- Calculate the precise acquisition frequency. Saving GPS PPS signal together with the MiniGRAIL data allows to calculate the accurate value of the acquisition frequency.

- Do decimation to reduce a data stream. To reduce the data processing time only the data in the band of interest can be extracted from the raw data set. For acquisition system sampling frequency of 18.6 KHz, according to Nyquist-Shannon sampling theorem the signal with frequencies up to 9.3 kHz can be reconstructed. But most of the time we are only interested in a few hundred Hz band around 3 kHz, where all the normal modes are located.
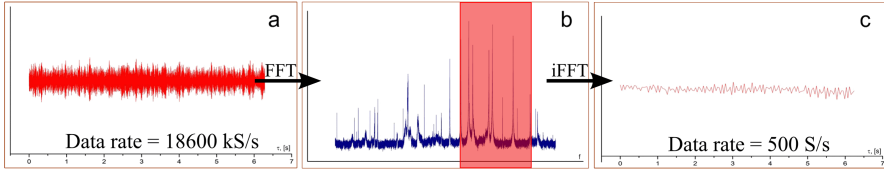
Figure 2.10: Data subsampling

2.3   Data transfer

Once available, the data from MiniGRAIL will be transferred to Theoretical Physics Department of University of Geneva for data analysis. The transfer algorithm and data analysis pipeline developed in Geneva is described in [31]. The acquired MiniGRAIL data is first copied from the acquisition PC to "To_transfer" folder on the NAS. Once the data is transferred it is moved to "Transferred" folder, so it is never deleted from MiniGRAIL storage. The transfer is done with command line shell script calling *rsync* utility [50]. We have measured an average transfer rate of $4.5\,MB/s$, which is much higher than the acquisition data rate of $600\,kB/s$.

Chapter 3

Preparing for the first scientific run

Introduction

In this chapter we summarize all the improvements we have made to the MiniGRAIL setup in the process of the preparation for a full 6-transducer scientific run. Every intermediate run we had, contributed to our experience and understanding of problems we might face during the course of the experiment. The major improvements are listed below, and explained in details in the rest of the chapter.

- We believed that a structural imperfection of the first MiniGRAIL sphere was limiting the mechanical quality factor of the modes, so it was replaced with a new one. The new sphere is also slightly bigger in diameter - $68\,cm$ instead of $65\,cm$, the maximum size that fits in the Dewar of MiniGRAIL setup. The old sphere was annealed at $400\,^oC$ on air, while the new one was annealed at a temperature of $800\,^oC$ in vacuum in order to decrease the concentration of internal defects that could lead to long thermal relaxation times at mK temperatures.

- New improved capacitive transducers were designed all coupled to a superconducting transformers and a double stage SQUID amplifiers.

- A complete data acquisition system was developed and installed. We have also developed some basic data processing software(see chapter 2). The stability of the detector's acquisition system was also studied.

- Based on the results of the previous experiments, we improved the magnetic shielding of the setup and installed radio frequency filters on the electric lines, going to the sphere from room temperature.

3.1   New transducers design

In order to increase the sensitivity, we have designed new transducers with a larger electrode area and smaller resonant mass. They were also designed in a way that greatly simplifies the polishing of a capacitor surface thus increasing the maximum electric field the transducer can hold.
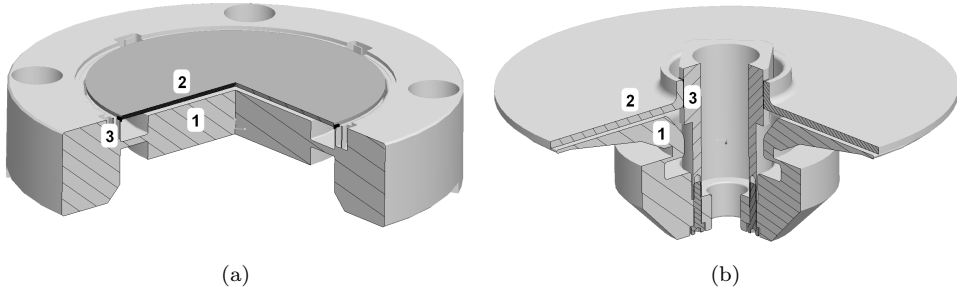

(a)   (b)

Figure 3.1: Transducers design - old(a) and new(b). The electrode(2) is glued with insulating epoxy to the support(3) forming a planar capacitor with a resonating mass(1).

In the old "closed membrane" [25] transducer design on figure 3.1(a) the resonating mass (1) is machined together with the electrode support (3) and is lower than the surrounding transducer body thus making the polishing of the resonator surface a complicated task. Also once the transducer is assembled it is not possible to open it again for cleaning without removing the epoxy and regluing the electrode again afterwards.

In the new design on figure 3.1(b) the electrode support is attached to the transducer body by means of 4 M3 screws and can be easily removed, so the capacitor surfaces can be polished very well. After the mass and the electrode are polished, the support is installed in place and the electrode is glued to it with Stycast 2850FT epoxy. A $15\,\mu m$ Kapton foil is used as a spacer to create the gap between the electrode and the resonating mass. It is also possible to disassemble the transducer to clean the electrodes and assemble it again without significant change in transducer capacitance or planarity. As can be seen from table 3.1 due to the smaller gap and much larger surface area the capacitance of the new transducers is almost a factor of 5 higher than of the old ones.

Since making a real transducer is a precise and time consuming work, before the actual machining we always evaluate the design by performing a Finite Element Analysis (FEA) study. On figure 3.2 the results of the resonator modal analysis are shown. The mechanical properties of the model are set to match $CuAl6\%$ and the bottom surface is set fixed. It is easy to see that the only mode that couples well to the radial motion of the sphere is the $2816\,Hz$ "umbrella" mode of the electrode.
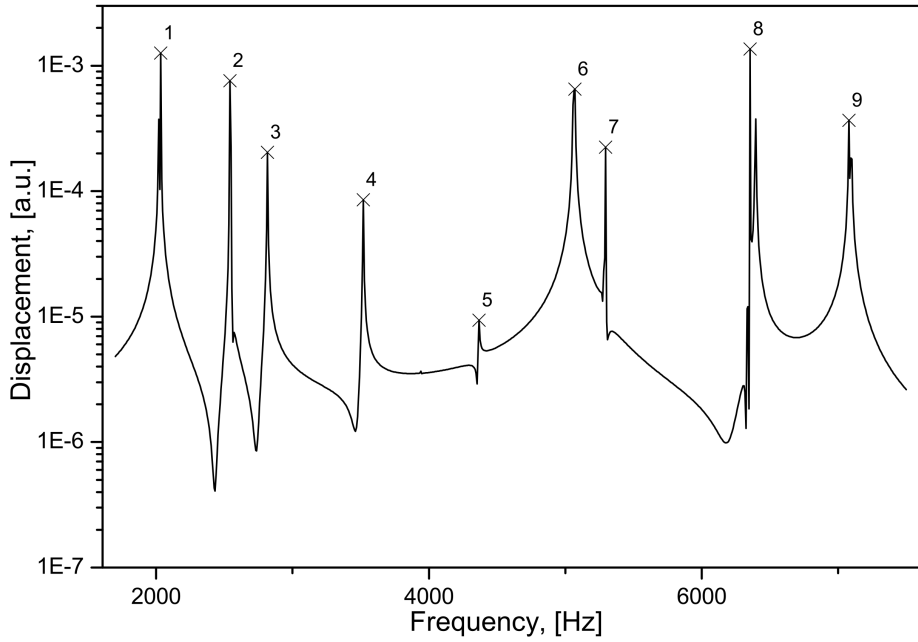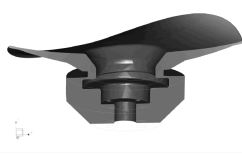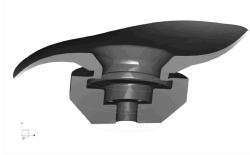
Figure 3.2: Resonator FEA simulation
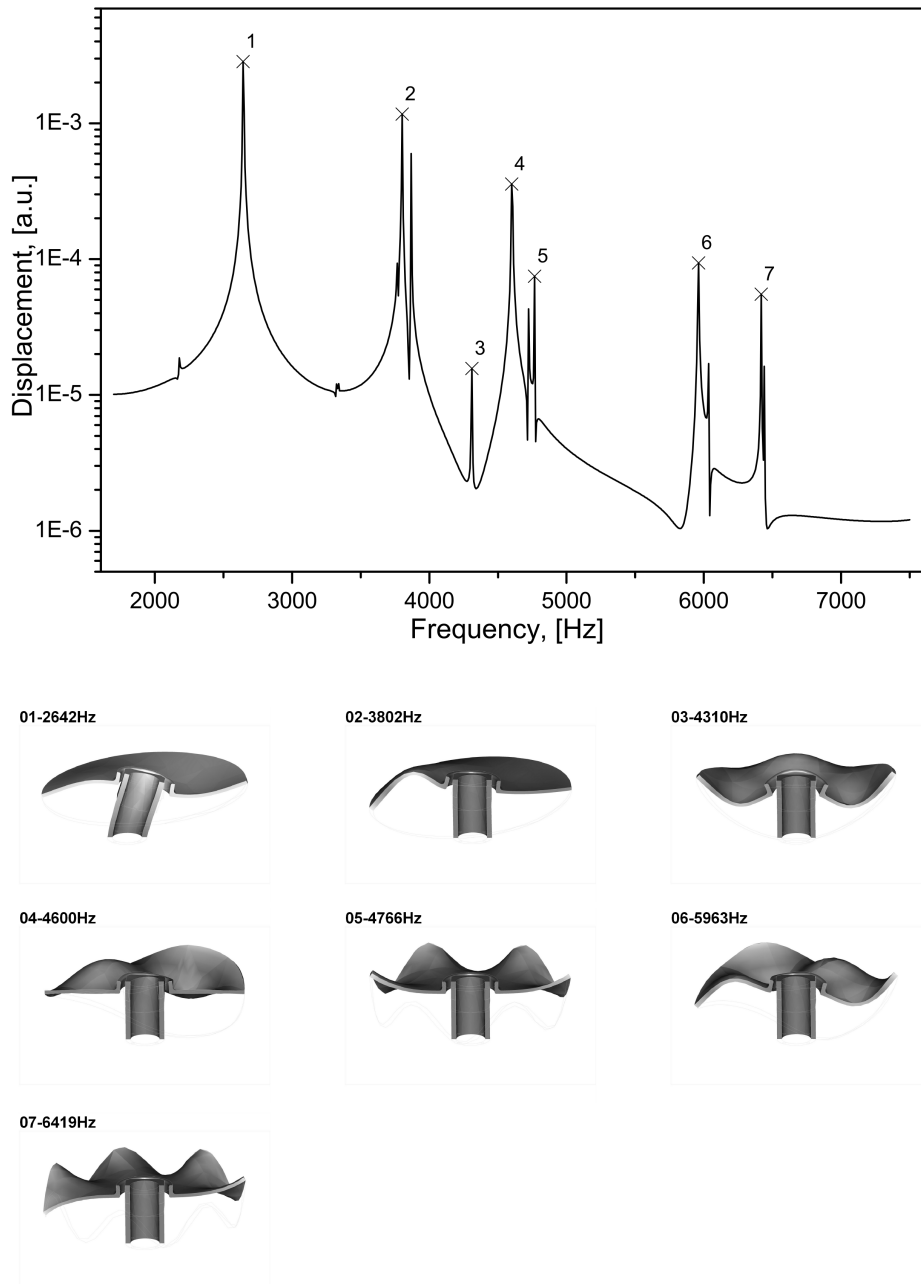
Figure 3.3: Electrode FEA simulation

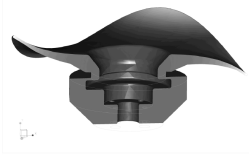| Parameter	old transducers	new transducer
mass, $[kg]$	$0.2 - 0.7$	~ 0.2
area, $[cm2]$	~ 25	100
gap, $[\mu m]$	$25 - 50$	15
C, $[nF]$	≤ 1	$4 - 5$

Table 3.1: A comparison of the properties of the old transducers, used in previous runs and the improved design (new transducer). The increased area and the smaller gap of the new transducer results in a capacitance of about a factor of 5 higher than that of the old transducers type.

This is also the only mode that significantly changes the average distance between the resonator and the electrode, thus modulating the transducer capacitance.

On a real transducer it is possible to tune the frequency of the "umbrella" mode by slightly varying the shape of the resonator.

We have also performed a study of the electrode assembly(see figure 3.3). We have found one mode that might lie in the bandwidth of MiniGRAIL - $2858\,Hz$ mode, but because it is a bending mode it should weakly couple to the radial motion of the sphere and since the electrode is glued to the support by means of low Q epoxy glue, the mechanical quality factor of the assembly should be low.

Figure 3.4: Mechanical quality factor of the "umbrella" mode of the transducer as a function of the temperature. The transducer was assembled with a gap of $\sim 25\,um$ and was charged to $180\,V$.
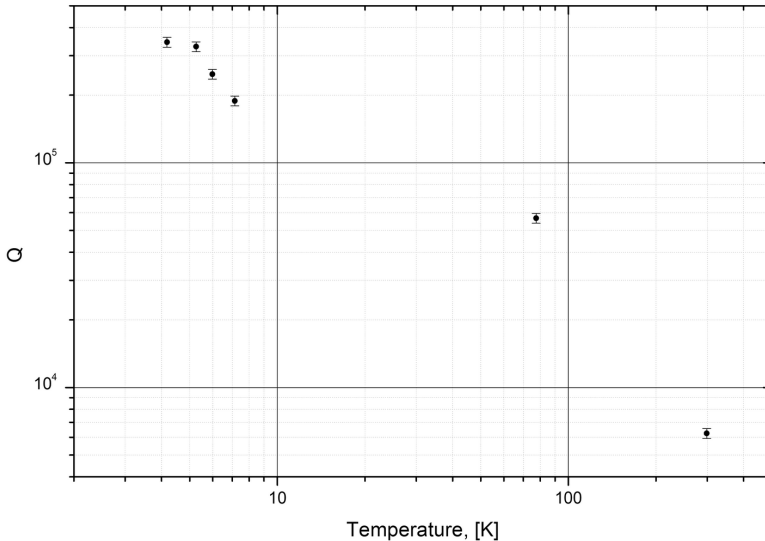
We have measured the mechanical quality factor of the assembled transducer down to the temperature of $4.2\,K$. During the test the transducer was suspended in high vacuum inside a $4K$ cryostat. The transducer was assembled with a gap of $\sim 25\,um$ and was charged to $180\,V$. We used a small piezoelectric actuator glued to the support of the transducer to excite the resonator and an amplifier connected to the transducer through the decoupling capacitor for read-out. The Q factor was calculated from the ring-down measurement.

The mechanical quality factor of the $2953.4\,Hz$ "umbrella" mode of the resonator as a function of temperature is shown on figure 3.4. At $4.2\,K$ the quality factor we have measured is $\sim 3 \times 10^5$, which is at least on a par with the previous transducers designs. We have also noticed that the Q factor decreases with the increase of the transducer bias voltage, yielding [51] the electric quality factor $Q_{el} \sim 15 - 20$. This value indicates high electric losses in the transducer. The origin of such losses is unclear, however for every transducer design we had, Q_{el} was always in the same range.

3.1.1   Transducers bias voltage stability

The stability of the transducers charge was one of the problems we encountered during the previous runs. Because of the high mechanical quality factor of the modes, it might take many hours to accurately acquire the data with enough resolution and signal to noise ratio to make the calibration. The electric field in a transducer gap introduces an attractive force between the electrode which reduces the mechanical spring constant of the resonator. A change of the resonance frequency of the mode due to changed spring constant can be expressed as $f_r^2 = f_0^2 + \alpha V_b^2$ [25], where V_b is the bias voltage of the transducer, and α is the coupling factor which expresses how well the transducer is coupled to the particular resonance mode. Thus if V_b drifts with time, it is not possible to acquire the modes accurately.
A capacitive transducer can lose the charge due to current leakage between the electrode and the resonating plate or through the voltage bias line connected to the transducer. The high resistance of Stycast epoxy, used to assemble the transducer, and high vacuum in the IVC prevent the current leakage between the plates. To prevent the discharging through the bias line we use magnetic reed switches (see fig. 3.5(a)). The switches are normally open, so they mechanically disconnect a transducer from the bias line[1].

The figure 3.5(b) shows the evolution of the resonant frequency of the modes during one week period of 8 September - 16 September 2005. The bias voltage was 192 V. As an example we have also plotted the data from 27 September which is acquired with a bias voltage of 204 V and shows a clear frequency shift. So, as we can see, no noticeable transducer discharge observed for one week of monitoring.

---

[1]When using reed switches at low temperatures one should pay attention that some switches might have an exchange gas inside which condenses on the electrode and freezes the switch open.
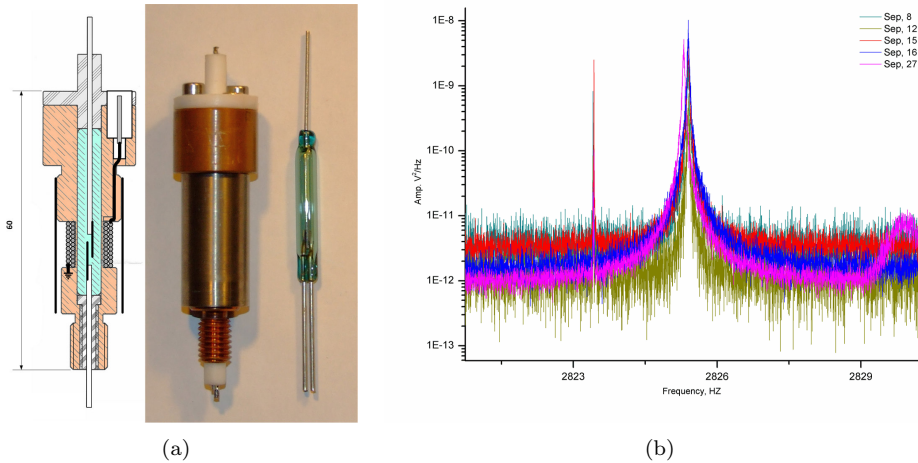
(a) (b)

Figure 3.5: Reed switch used to physically decouple the charging line from the transducer (a) and modes frequencies evolution with time (b). Transducer bias voltage was 192V for September 8 - September 16 and 204V for September 27 2005

3.2 New superconducting transformers

In order to efficiently couple the low impedance SQUID input coil to a high impedance capacitance transducer an impedance matching transformer has to be used. We have redesigned the superconducting matching transformer housing in order to fit six of them on the last mass of the vibration isolation system.

The design is similar to the one of the old transformer box reported in [25]. The housing(1) is made of lead-plated copper and has three separate compartments for the superconducting transformer(2),decoupling low loss Teflon capacitor(3) and double compartment for the SQUID modules(4). The transformer is placed inside an extra lead-plated copper box(5), wrapped in cryoperm foil, and placed inside the main box. A small transformer(6) is placed in-between the secondary coil of the matching transformer and the input coil of the SQUID. It is used to inject a calibration signal to the SQUID input in order to calibrate the SQUID amplifier sensitivity. The decoupling capacitor is needed to separate the SQUID input from a high DC bias voltage of the transducer. The design properties of the transformer box are summarized in table 3.2

3.2.1 Connecting input terminals of the SQUID

A common technique to connect the input terminals of the thin-film SQUID module to the PC-board is by means of the ultrasonic bonding. For bias and Fb lines it is possible to use the standard Al bonding wire. However for the input terminal of the SQUID a superconducting wire has to be used. We use a $50\mu m$ Nb wire annealed and

(a)   (b)
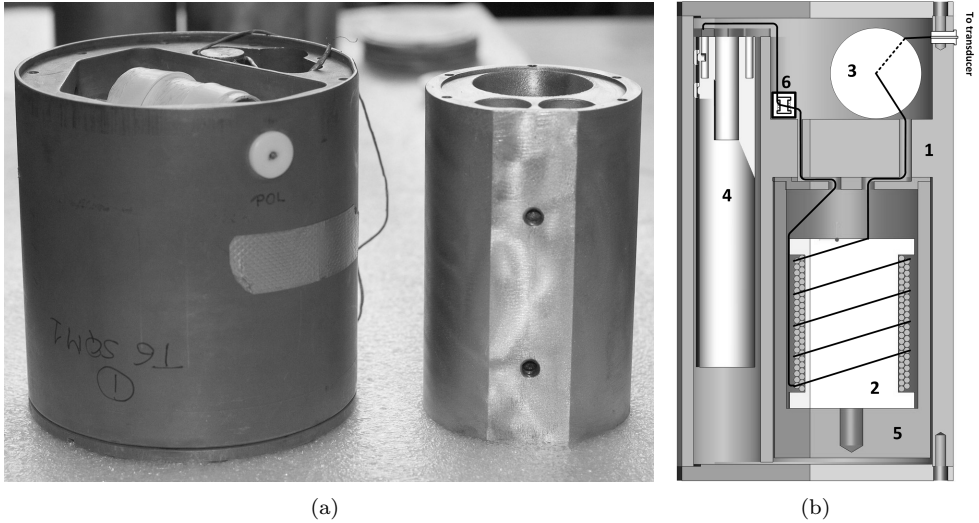
Figure   3.6:   New superconducting transformers, (a)-compared to the old design, (b)-schematics: 1-Lead-plated Cu housing, 2-Superconducting matching transformer, 3-decoupling capacitor, 4-SQUID module, 5-Transformer housing, 6-Calibration transformer

Primary Inductance, $[H]$	0.2
Secondary Inductance, $[\mu H]$	2
Coupling	0.85
Electric mode Q	$\geq 5 \times 10^4$
Calibration coil mutual inductance, $[nH]$	100
Decoupling Capacitor, $[nF]$	150/136

Table   3.2: Transformer box design parameters.

etched with 1:1 HF and HNO3 mixture to the thickness of $15 - 20\mu m$. The annealing is done in vacuum. The wire is heated to a temperature of $\simeq 2200^o C$ by sending a current through it for a time of about 5 min . As a result we get very plastic bonding wire with a critical current of the bonds about an order of magnitude higher than the dynamic range of the SQUID and a thermal noise much lower then the internal noise of the SQUID.[52]

3.3   Magnetic Shielding

In order to reduce the magnetic noise picked up by the SQUIDs, 50mK and Still flanges together with the corresponding radiation shields were lead-tin plated. To reduce the trapped magnetic field, the shields were also covered by a few layers of
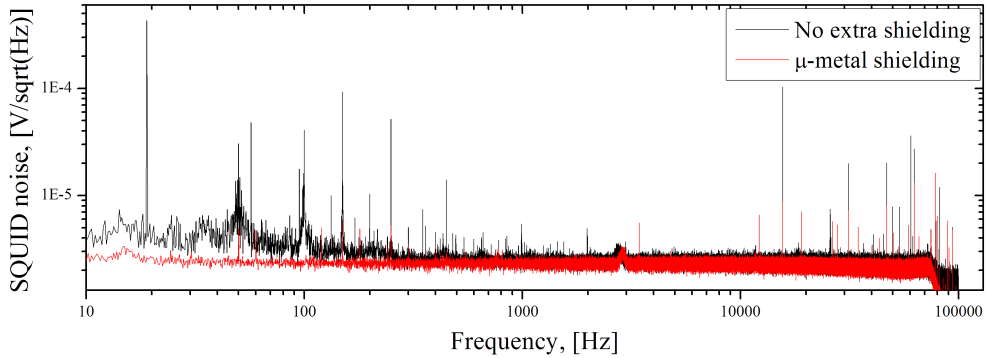
Figure 3.7: Effect of the magnetic shielding on the SQUID noise

high magnetic permeability μ-metal foil. The effect of the magnetic shielding on the SQUID noise measured on a dipstick is shown on figure 3.7.

3.4 RF filters

We have developed compact copper powder RF filters that will be installed on the calibration lines at low temperatures, so the RF noise picked up by the cables will not interfere with the SQUID operation. At frequencies below $1\,MHz$, we have measured

(a) RF filter

(b) Typical attenuation curve
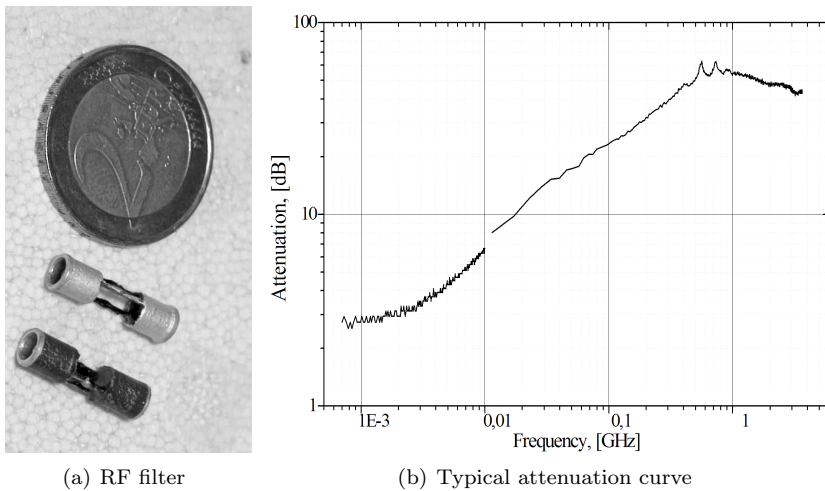
Figure 3.8: A design and attenuation curve of copper powder RF filters we have developed

the attenuation of less than $3\,dB$, which is acceptable in our case. Above the frequency of $500\,MHz$ the attenuation increases to $45 - 55\,dB$(see figure 3.8). We have found that it is possible to increase the attenuation up to $90-100\,dB$ by using a smaller gauge wire with thinner insulation, but the reliability and the yield drops to unacceptable values.

3.5 SQUID developments

3.5.1 Run 8 acquisition stability

Run8 was the first one where the sphere was operated for a relatively long time at millikelvin temperatures.It lasted for three month - from beginning of August 2005 till mid November 2005. The overview of the data acquisition activity is presented on figure 3.9
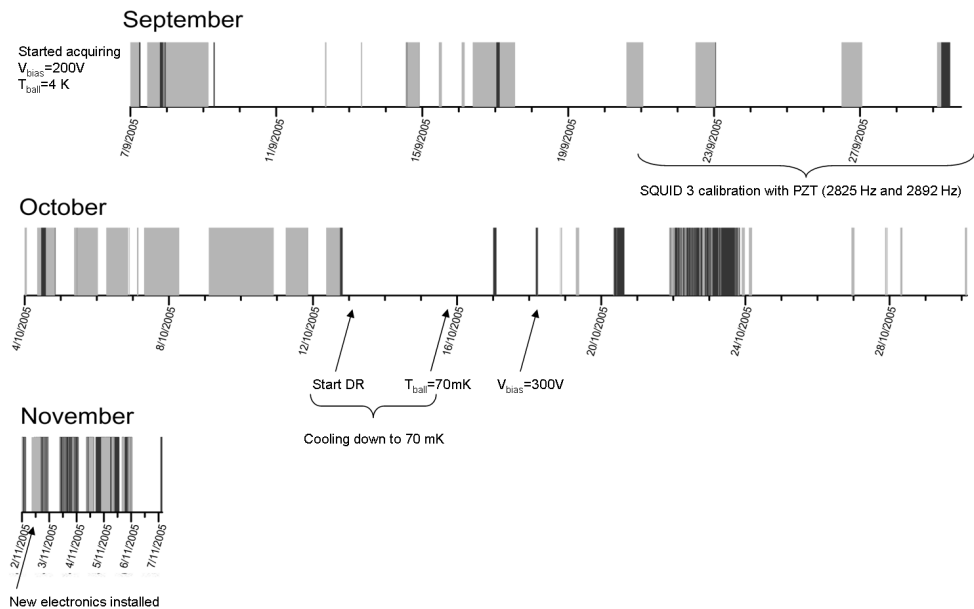
Figure 3.9: Run8 data acquisition overview. Gray regions show when the acquisition was running with light gray color meaning that the sphere modes were visible above the SQUID noise

The overview is made offline by analyzing the acquired data for the visibility of the normal modes of the sphere. The light gray color indicates that the modes are visible in the noise spectra and their SNR is above a threshold. The dark gray color indicates that the system was running and SQUIDs were locked, but the modes were

not visible. White color means that the acquisition was not running.

	September	October	November
Duty cycle, [%]	25	33	56
Good data, [%]	84	64	22

Table 3.3: MiniGRAIL duty cycle during run8

As we can see from the table 3.3 the duty cycle of MiniGRAIL during Run8 was not very big, especially in September. This is due to some non data acquisition works(like transducers calibration), which were conducted during the run. However, when the acquisition was running, the amount of good data was high enough during the first two months of operation but dropped dramatically in November, when the antenna was cooled to a temperature below 70 mK. We believe that the reason might be in the SQUID we used for the second stage. The steep flux-voltage transfer of the DROSes makes them a good choice for an amplifier SQUID[25, 48]. Because of the large gain direct readout electronics can be used, which simplifies the electronics design a lot. However, our experience has shown that the high flux-voltage gain of the DROS can also cause the stability problems, especially at low temperatures when the gain increases even further. This is believed to be a reason of a very low stability of MiniGRAIL acquisition below $4\,K$, described above.

Because of problems operating the DROSes at mK temperatures we decided to switch back to a conventional DC SQUID as an amplifier. The SQUIDs were developed by Low Temperature division of the Department of Applied Physics at the University of Twente and are fabricated at a foundry of IPHT Jena [53]. The $4.2\,K$ measurements were performed in Leiden and Twente universities. Millikelvin measurements were done in a dilution refrigerator at Leiden Cryogenics[54]

The SQUIDs are designed using the maximal line width resolution available by the process - $3\,\mu m$. The size of the Josephson junctions is $3.2 \times 3.5\,\mu m^2$ and the critical current density J_0 was $110\,A/cm^2$ and $120\,A/cm^2$. The critical current density tolerance across the single chip is $5\,\%$. The Josephson junctions are externally shunted by shunt resistors made of resistive $115\,nm$ PdAu film. The SQUID chip dimensions are $2.5 \times 2.5\,mm^2$. Two different SQUID layouts were made - flux transformer and parallel washer design SQUIDs. The design considerations, model, and the experimental results are explained in detail in [55]. Here we will only give a summary of the key parameters of the SQUIDs.

3.5.2 Flux transformer DC SQUID

The aim of the flux transformer design is to couple a low inductance SQUID loop($L_{SQ} \sim 10^2\,pH$) to a high inductance input coil($L_{inp} \approx 1.6\,\mu H$), used in MiniGRAIL read-out, by means of an intermediate transformer. To overcome resonance effects, a damping resistor, Rd is added in parallel to the SQUID loop. It has the same resistance as the

shunt resistors of the Josephson junctions ($5.7\,\Omega$). The schematics and the layout of the flux transformer SQUID are shown on the figure 3.10. The design parameters are summarized in the table 3.4
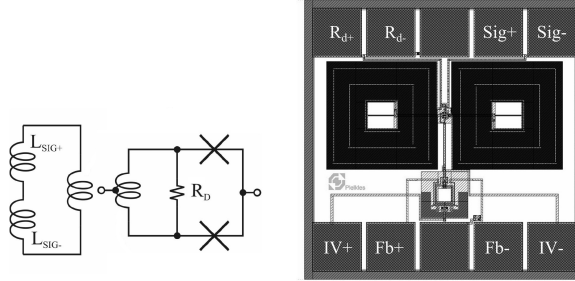
Figure 3.10: Twente Flux transformer SQUID schematics [a] and layout [b]

	$2I_0, uA$	R_{sh}, Ω	L_{sq}, pH	β_L	β_C	L_{sig}, uH	M_{sig}, nH
Design	22.6	5.7	170	1.8(1.1*)	0.7	1.6	10.4
Measured	24	5.0		1.9(1.2*)	0.6		8.7

* - at RF frequency

Table 3.4: FT SQUID design parameters

Using the theory for non hysteretic, uncoupled DC SQUIDs [26] we can estimate the best reachable sensitivity. For a temperature of $4.2\,K$ the calculated flux noise spectrum density is $S_\Phi = 0.68\,\mu\Phi0/\sqrt{Hz}$ corresponding to an energy resolution of $73\,\hbar$.
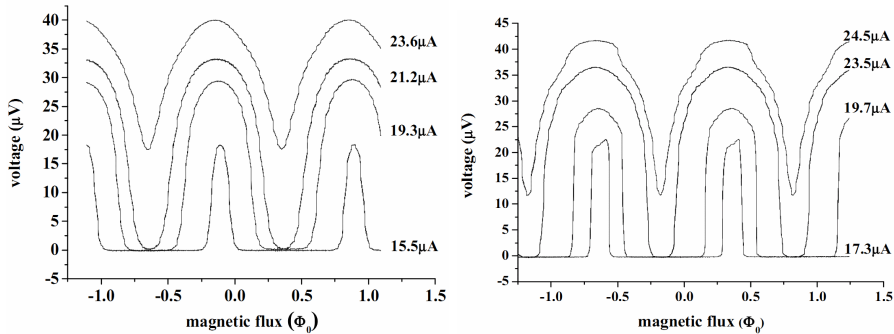
Figure 3.11: A flux-voltage characteristics of a FluxTransformer SQUID at 4.2 K (a) and 300 mK (b)

The measured flux-voltage characteristics of the SQUID at two different temperatures are shown on figure 3.11. At 4.2 K, we observed a maximum flux-voltage transfer of $110\,\mu V/\Phi 0$ - 2.5 times the value predicted by the theory [26]. At $0.3\,K$ it has increased to $\approx 800\,\mu V/\Phi 0$. The measured mutual inductance of the input coil is 8.7 nH instead of the design value of 10.9 nH. A minimum flux noise of $1.4\,u\Phi 0/\sqrt{Hz}$ was measured at 4.2 K in a two-stage setup with a DROS as second stage. Because of the steep transfer function at low temperatures we did not succeed in getting a two-stage setup working. In a single stage a flux noise of $2.8\,\mu\Phi 0/\sqrt{Hz}$ was achieved at temperatures below 1 K. By subtracting the flux noise related to the room temperature amplifier from the measured value, the rough estimation of the real flux noise below 1 K is $1.5 - 2\,\mu\Phi 0/\sqrt{Hz}$.

3.5.3 Parallel washer DC SQUID

Because of its symmetric layout and the reduced coupling between the feedback- and the signal-coils, this design was made similar to the one of a commercial Quantum Design SQUID [56].
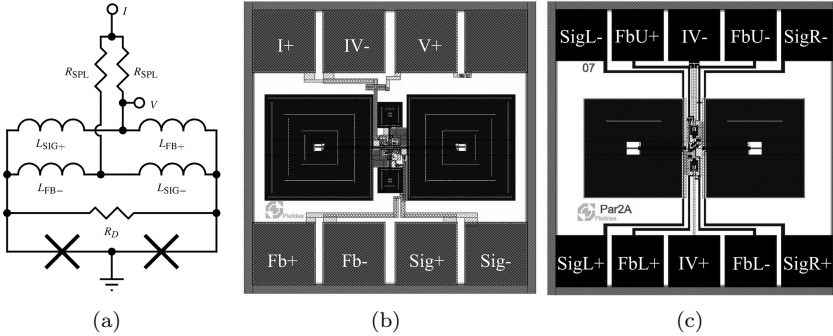
Figure 3.12: Parallel washer design SQUID schematics (a) and layout of first (b) and second (c) design steps

The layout and the schematic are shown on figure 3.12. The main differences from the original design are added cooling fins and the splitting of the bias current is done on-chip via the two parallel resistors R_{SPL}. The design parameters are listed in table 3.5.

We have measured the SQUID sensitivity with a dilution refrigerator in two-stage configuration. The Flux Transformer SQUID described above was used as an amplifier. The measured flux noise as a function of temperature is presented on figure 3.14

As we can see from the graph, the noise scaled almost linearly with the temperature down bath temperature of $600\,mK$. At $4.2\,K$ we measured a flux noise of $2.1\,\mu\Phi 0/\sqrt{Hz}$. Below the temperature of $200\,mK$, the measured flux noise was

	$2I_0, uA$	R_{sh}, Ω	L_{sq}, pH	L_{inp}, uH	M_{sig}, nH	β_L	β_C
Design	22.6	5.6	270	1.5	12.4	2.9(1.6*)	0.65
Measured	11	4.9			11.2	2.8(1.6*)	0.5

* - at RF frequency

Table 3.5: Parallel washer SQUID design parameters
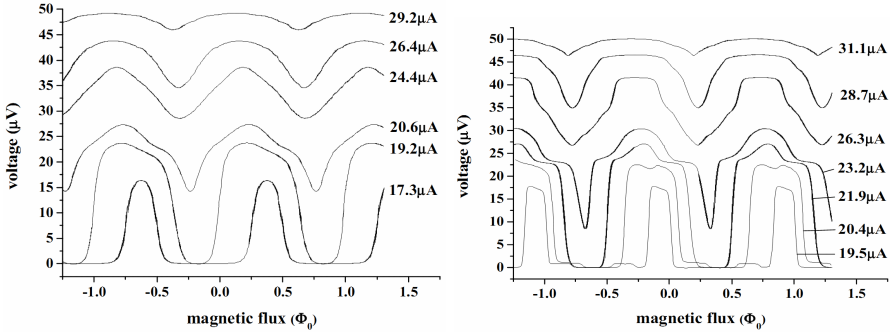
Figure 3.13: A flux-voltage characteristics of a parallel washer SQUID at 4.2 K (a) and 600 mK (b)
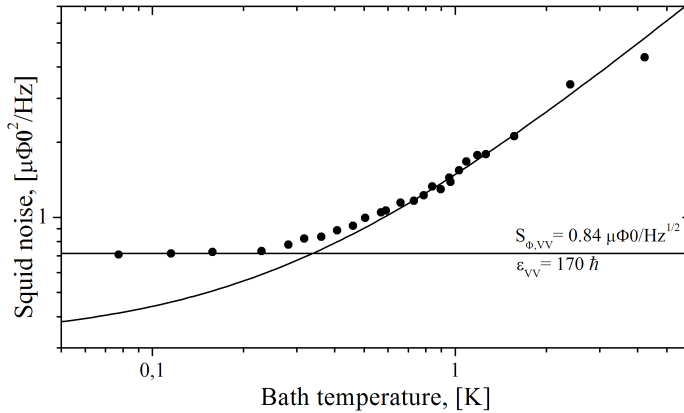
Figure 3.14: Flux noise of the parallel washer design SQUID as the function of temperature
.

$0.84\,\mu\Phi0/\sqrt{Hz}$ and did not improve further with temperature. This corresponds to an equivalent input noise current of $\sqrt{S_{\Phi,VV}}/M = 155\,fA/\sqrt{Hz}$. Using the measured value of M and the design value of L_{inp} the coupled energy resolution $\epsilon_{vv} = 170\,\bar{h}$.

The minimal effective temperature of about $400\,mK$ was reached is due to the

influence of hot electron effect in the shunt resistors. The power dissipated in the resistors was estimated from the voltage and the bias current at the working point of the SQUID($I_b \approx 30\,\mu A$, $V \approx 40\,\mu V$). Assuming that all the power dissipated only at the shunt resistors, $P = 0.6\,nW$ per resistor, This value and the minimal reached effective temperature agrees with the model described in [55]

3.5.4   SQUIDs performance at mK temperatures

As we know, the noise of the typical DC SQUIDs we use in our experiments is dominated by the Johnson noise in the shunt resistors[26]. While it sounds promising, as the noise goes down with temperature, in practice there is a limit where dissipated power and a reduced electron-phonon interaction in a shunt resistor prevents it from further cooling. One of the thermal resistance mechanisms that one should often consider at low temperatures is boundary (Kapitza) resistance. It appears due to the acoustic phonon mismatch on the interface of two materials [57]. The relation between the dissipated power P and the temperature is

$$P = kA_k(T_{ph}^4 - T_{bath}^4), \tag{3.1}$$

where T_{ph} is the temperature of phonons in a shunt resistor, T_{bath} is the temperature of the thermal bath, A_k is the interface area, and k is a materials constant. A second thermal resistance mechanism is related to the electron- phonon interaction in the resistor itself. We can write down a similar relation for electron and phonon systems temperature:

$$P = \Omega\Sigma(T_e^p - T_{ph}^p), \tag{3.2}$$

where Ω is the resistor volume and Σ is constant which depends on the strength of electron-phonon coupling. The theoretically predicted value of the exponent $p = 4-6$ depending on the metal type and the phonon dimensionality. Experimentally in many cases $p = 5$. As we can see from equation 3.2 the obvious way to reduce the temperature difference for the same dissipated power is to increase the volume Ω. Extensions to the shunt resistors that increases the volume without changing the electrical resistance are called cooling fins.

The experiments to measure the effective temperature of shunt resistors as a function of the dissipated power and cooling fin size were performed in a dilution a refrigerator in Leiden. The scheme of the experiment is shown on figure 3.15. The shunt resistor R_d is biased by a low-pass filtered($C_{LP} = 1\,\mu F$, $R_{LP} = 760\,k\Omega$) current source I_b. The power, dissipated on a resistor is $P = I_bV$, where V is the voltage drop across the resistor, measured by a room temperature voltmeter, connected in a four-terminal scheme. The temperature of the resistor is evaluated by measurement of its Johnson noise with a SQUID. A decoupling capacitor C_D is used to high pass filter the resistor noise, so the intrinsic noise of the SQUID can also be measured. The temperature of the thermal bath was calculated from the resistor noise with $I_b = 0\,A$.

The results for a shunt resistor without cooling fins are shown on figure 3.16(a). The electron system temperature was calculated from average the of PSD noise above
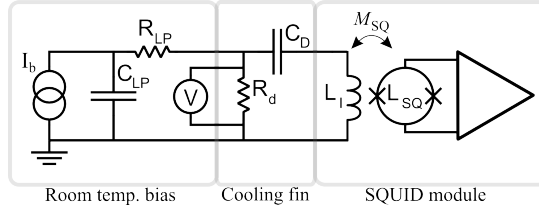
Figure 3.15: Scheme of the measurement setup. The shunt resistor R_d is biased by a current source I_b. The voltage drop across the resistor is measured by a room temperature voltmeter, connected in a four-terminal scheme. The temperature of the resistor is evaluated by measurement of its Johnson noise with a SQUID. A decoupling capacitor C_D is used to high pass filter the resistor noise, so the intrinsic noise of the SQUID can also be measured.

cutoff frequency of the decoupling capacitor C_D. For low power dissipation($P \leq 1\,nW$) the fitted exponent value $p = 5.05$ is in a good agreement with reported results for thin PdAu resistors [58]. At a higher power however, the experimental data deviates from a theoretical curve with $p = 5$. At a middle temperature range the data can be refitted with $p = 5$ and the effective volume, which only includes the part of the resistor not covered by superconducting Nb pads. At even higher temperature($> 1\,K$) the phonon system of the resistor can not be considered two dimensional, so higher dimensionality [59] and Kapitza resistance should be taken in to account [60].

The results of an identical experiment for a shunt resistor with cooling fins of tree different geometries are shown on figure 3.16(b). We can see that while the cooling fins help cooling the shunt resistors, at the power typically dissipated by the SQUID ($\approx 500\,pW$) the effect is negligible. From the theoretical and numerical studies presented in [55] one can conclude that the cooling fins are only effective at low temperature,low power conditions. At higher temperatures, limited by the SQUID dissipation, the cooling volume is restricted by the temperature dependent thermal relaxation length. In conclusion, in order to achieve the minimal working temperature one should maximize the volume of the dissipating part of the actual resistor. A possible solution is either bulk or implanted into silicon[61, 62] resistor. Another option is direct active cooling of the electron system.A recent work [63] has demonstrated a cooling power of $\approx 20\,pW$ per junction area of $0.3\,\mu m^2$ at $1\,K$. A resulting cooling power density is $\sim 65\,pW/\mu m^2$, comparable with the power dissipated by the SQUID.

3.5.5   Transformer boxes noise

Before mounting the assembled transformer boxes on the MiniGRAIL setup we have measured the temperature dependence of the SQUID noise. The measurements were done in vacuum in liquid He cryostat. By pumping on the helium bath we have reached the minimum temperature of $1.6\,K$. The input terminals of the primary coil of the transformer were shorted by a superconducting wire. The noise curves of

(a) Shunt resistor without cooling fins

(b) Shunt resistor with three different cooling fin geometries
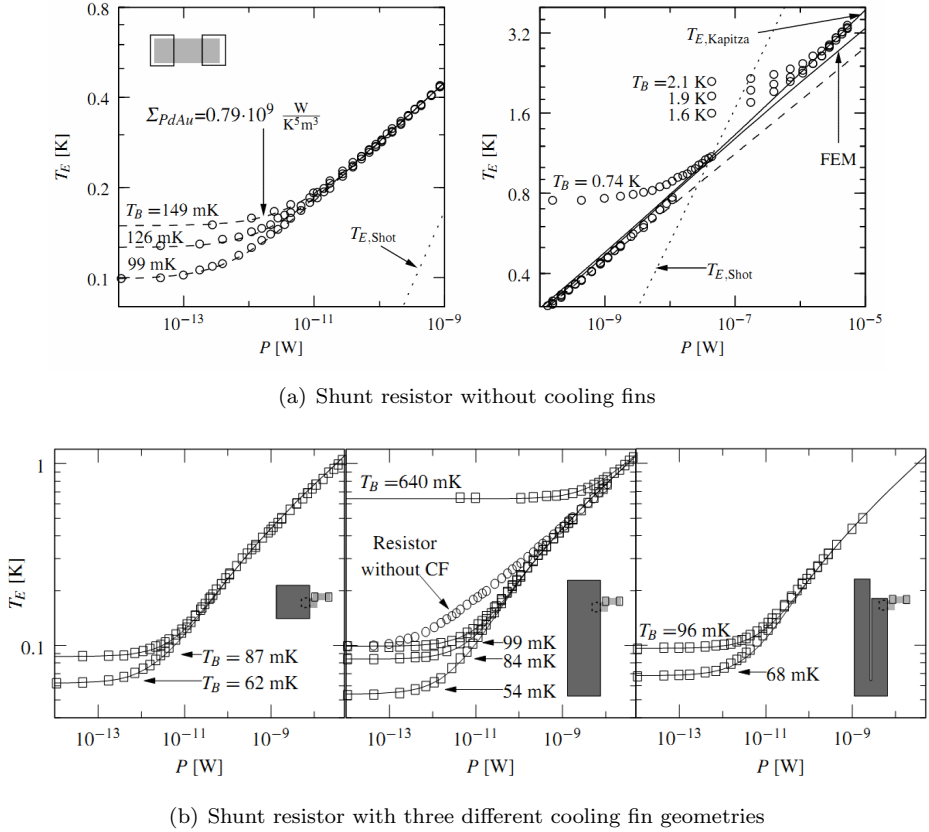
Figure 3.16: Temperature of the shunt resistor as a function of dissipated power [60].

two transformer boxes are shown on figure 3.17. Box#3 has a dual stage Quantum Design SQUID module, provided by the Auriga group, and Box#5 has a QD and flux transformer SQUID module made in Leiden. The noise curves of our other transformers were similar to Box#5.

3.5.6 Implementing a "cold" damping network

For a SQUID, strongly coupled to a high-Q resonator, the parasitic coupling from the SQUID to the input circuit can introduce a negative impedance which will overcome the dissipative terms of the input impedance and the resonator will be constantly pumped making the SQUID operation impossible. A special damping network can be implemented to stabilize the SQUID operation [64, 65]. Because the new MiniGRAIL SQUID electronics is fully differential, we modified the RC damping network that was

(a) Box#3

(b) Box#5
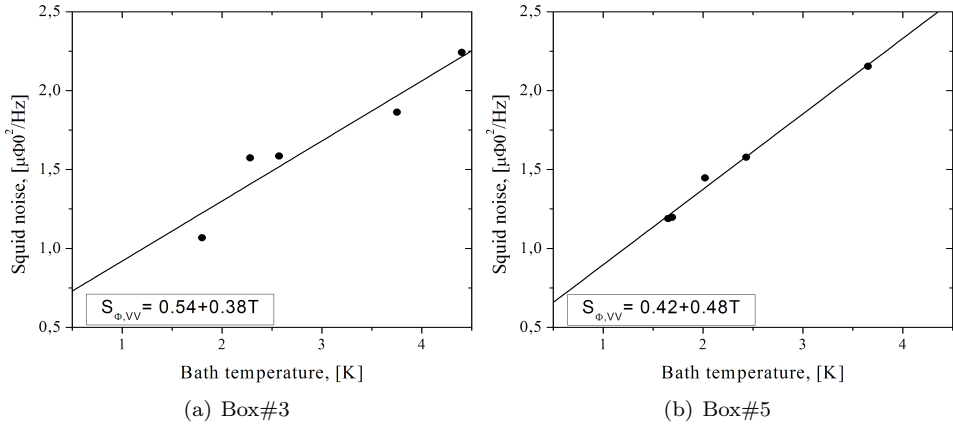
Figure 3.17: Flux noise of the two transformer boxes with shorted input. Box#3(a) has two Quantum Design DC SQUIDs and Box#5 has QD SQUID as a first stage and FT SQUID as an amplifier

used in the previous runs(see [25]).
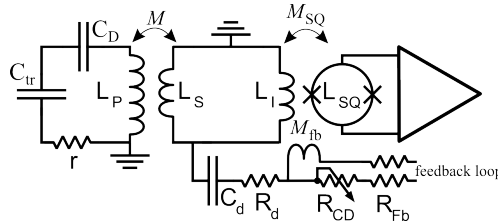
Figure 3.18: Schematics of a differential cold damping network.

The schematics of a modified damping network is shown on figure 3.18. $C_d = 10\,pF$, $R_d = 0.35\,M\Omega$. An extra resistor, R_{cd} creates an asymmetry in the Fb line, so that feedback coil in not at a zero potential anymore. So a small part of a Fb signal should leak to the ground through an RC line that introduces 90° phase shift in a signal. The cold damping network effect is equivalent to a series resistance r in the input circuit. We note that this additional resistance is the result of the feedback effect and therefore has no thermal noise associated with it. The effect of the cold damping network on the electrical mode Q factor and resonance frequency is given by [65]:

$$\Delta\left(\frac{1}{Q}\right) = \left(\frac{M}{L_t}\right)^2 \frac{L_i}{L_r} \frac{M_{SQ}}{M_{fb}} \frac{\omega_0 C_d}{1 + (\omega_0 R_d C_d)^2} R_{CD} \equiv \alpha R_{CD}$$

$$\Delta f_0 = \frac{f_0}{2}\left(\frac{M}{L_t}\right)^2 \frac{L_i}{L_r} \frac{M_{SQ}}{M_{fb}} \frac{(\omega_0 C_d)^2 R_d}{1 + (\omega_0 R_d C_d)^2} R_{CD} \equiv \beta R_{CD},$$

$$(3.3)$$

where $L_t = L_s + L_i$ is the total series inductance in the SQUID input circuit and $L_r = L_p - \frac{M^2}{L_t}$ is the reduced primary transformer inductance.

By changing the value of R_{cd} it is possible to reduce the quality factor of the electric mode to a reasonable value. The damping network was tested with the SQUID electronics during the short test cool-down of MiniGRAIL in 2008.

The change of the damping factor and the resonance frequency as a function of the value of the damping resistor, R_{cd} is shown on a figure 3.19

(a)

(b)
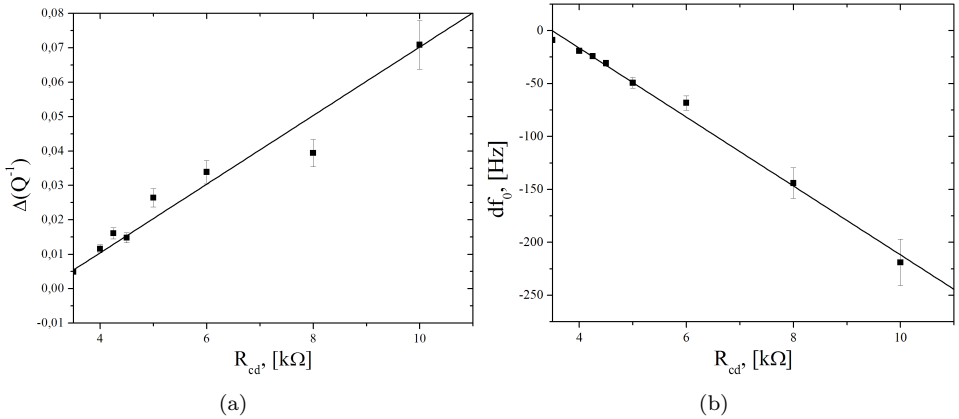
Figure 3.19: Effect of the cold damping on the electric mode quality factor (a) and resonance frequency (b)

3.6 Conclusions

In preparation to the big, 6 transducer run, we have tried to take into account and solve every problem we had during the previous cool-down:

- A multichannel acquisition system was developed and tested. It allows to store the acquired data together with the precise GPS timing information for later data analysis. An automatic SQUID reset electronics monitors the working point of the SQUID and resets the FLL integrator to relock the SQUID.

- Special effort was taken to improve the magnetic and RF shielding of the MiniGRAIL. This should improve the stability of the SQUID amplifiers.

- New transducers, with up to 5 times higher capacitance were developed. The new transducers can also be quickly disassembled and cleaned. This can be important, for operating 6 transducers simultaneously.

- Also new compact matching transformer boxes with the calibration coils were made.

- The DROSes were replaced with custom design DC SQUIDs which were tested in dilution refrigerator. The measured noise was good enough to use them as the second stage amplifiers, or even as the first stage(Parallel washer design SQUID)

Chapter 4

First calibration run of MiniGRAIL

Introduction

Because we have modified so many components of the system, as we described in the previous chapter, and due to the limited budget for liquid helium, we decided to do a short run aimed at testing a modified setup and verifying a calibration procedure we have developed. In this chapter we report the results of the calibration run of MiniGRAIL we performed in autumn 2010. For the first time we started the run with all 6 transducers mounted on the sphere. Each transducer was coupled to two stage DC SQUID amplifier. Five 2-stage SQUID modules consisted of commercial Quantum Design DC SQUID and custom design flux transformer SQUID for the second stage(see chapter 3). One module was a standard 2-stage Quantum Design module similar to the one used in Auriga experiment [66]. The parameters of transducers and impedance matching transformers are summarized in table 4.1

We have also mounted 7 mass-loaded PZT resonators(calibrators) for calibration purposes. Six calibrators are placed at the same polar angles as transducers but shifted by 60° in azimuthal angles. The seventh calibrator is placed at an arbitrary position and is used to verify the direction reconstruction algorithms. The picture of the sphere with transducers and calibrators mounted is shown on figure 1.10 in chapter 1.

During the run we have cooled the system down to a temperature of $\approx 1\,K$. Unfortunately, due to a failure of some the switches and transducers only transducers at position 4 and 6 were operable, so we could not conduct the complete calibration procedure as planned. However we believe that we were able to extract some useful information which we will discuss further in this chapter.

Transducer position	1	2	3	4	5	6
Transducer capacitance,[*] [nF]	3.9	3.0	4.9	3.4	4.5	4.6
Max V_{bias}, [V]	240	195	200	200	180	180
V_{bias} at 77 K, [V]	138	155	152	160	164	155
Transformer box	Tr1	Tr2	Tr3	Tr4	Tr5	Tr6
Primary Inductance, [H]	0.18	0.12	0.183	0.166	0.205	0.178
Secondary Inductance, [uH]	7	≈ 2	2.04	1.8	1.67	1.85
Coupling	0.49	0.85	0.85	0.6	0.86	0.84
SQUID gain, [$V/\Phi 0$]	0.16	0.16	0.13	0.79	0.18	0.16
Electric mode Q	-	-	-	-	6.3×10^4	6×10^4
Calibration mutual inductance, [nH]	300	128	n.a.	3	n.a.	n.a.
Decoupling Capacitor, [nF]	138.8	152.0	133.9	156.2	159.8	149.8

[*] measured at room temperature

Table 4.1: Properties of transducers and superconducting matching transformers

4.1 MiniGRAIL directional sensitivity with non-optimal transducer configuration

The first question we would like to answer is: how much does our experiment suffer from the reduction of the number of transducers?

In the case of an ideal sphere with degenerate quadrupole modes this would result a disastrous drop in directional sensitivity leaving the detector almost blind to some directions. However, on the real sphere the modes are split in frequency, so instead of being sensitive to the sum of modes amplitudes, defined by the sum of spherical harmonics at transducer position, the transducer sees each mode individually.

The force F_c applied by a calibrator to the sphere surface at position (ϕ_c, θ_c) will excite five quadrupolar modes of the sphere with amplitudes

$$\mathbf{a}_m(t) \propto \mathbf{Y}_m(\phi_c, \theta_c) F_c(t). \tag{4.1}$$

If the modes are degenerate, then for a set of J transducers the radial displacement $\mathbf{q}_j$ of a sphere surface at transducer position$(\phi_j, \theta_j)$is given by (see section 1.1.2 in chapter 1)

$$\mathbf{q}_j(t) = \alpha \mathbf{B}_{mj} \mathbf{a_m}(t) \tag{4.2}$$

By varying ϕ_c and θ_c we can map the sphere surface in terms of sensitivity of each transducer. Since all modes have the same frequency, we can expect that for some directions the amplitudes of the modes at the transducer j position might cancel each other. The resulting amplitude q_j would be very low, meaning that this particular transducer is not sensitive to that direction. We express the total direction sensitivity as root mean square of transducers sensitivities:

$$Q(\phi_c, \theta_c) = \sqrt{\frac{\sum\limits_j \mathbf{q}_j^2}{J}}. \tag{4.3}$$

For six transducers in MiniGRAIL arrangement the direction sensitivity is almost uniform (figure 4.1(a)). If we only take into account transducers 4 and 6, the averaging will produce a complicated pattern, with sensitivity dropping by more than an order of magnitude in some directions(figure 4.1(b))
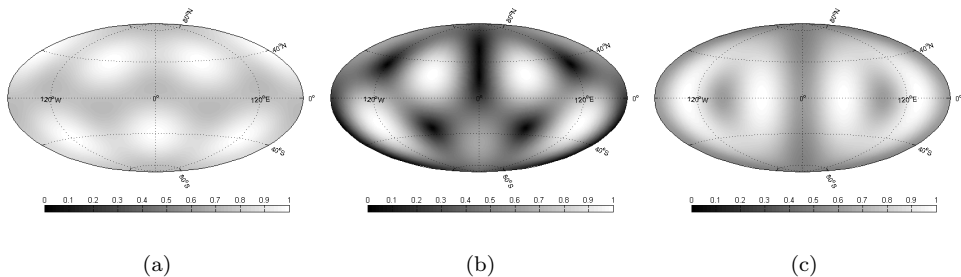

Figure 4.1: Directional sensitivity for full six(a) and for transducers #4 and #6 configuration for degenerate(b) and splitted(c) modes

If the modes are not degenerate then each transducer displacement amplitude q_j is split into a vector of five amplitudes $\mathbf{q}_{jm}$, which have different frequency and are seen by transducer independently. Again by doing an RMS averaging over m and then over j we can build the sensitivity map. The resulting pattern is much smoother, with the sensitivity only varying by about 50% (figure 4.1(c)). Another advantage of the non-degenerate modes is that each transducer has the information about all five quadrupole modes. In theory this allows direction reconstruction with less than five transducers. We will discuss it again in section 4.3.

In the analysis above we used a radial displacement of the sphere surface at the transducer position as the measure of sensitivity which is only valid for a wide band transducer like a piezo. It also does not take into account the noise which might significantly reduce the mode SNR. So real directional sensitivity degradation might be more significant.

4.2 Calibration

Here we describe the calibration procedure, we use to estimate the strain sensitivity of MiniGRAIL. First with the calibration transformer we do the energy calibration to measure the conversion factor between the energy stored in the mode and the current density at the SQUID input. Then we estimate the calibrators efficiency - by applying a known voltage to the calibrators we measure the energy deposited in the

modes. These two calibrations allow us to build the transfer function of the system and calculate the strain sensitivity of MiniGRAIL.

4.2.1   Energy calibration

Since in this run we have implemented calibration transformers, we do not need to use an extra calibrator as reported in [25], and are able to calibrate the read-out sensitivity directly. For better understanding it would be useful to show again a simplified version of capacitive transducer read out scheme on figure 4.2
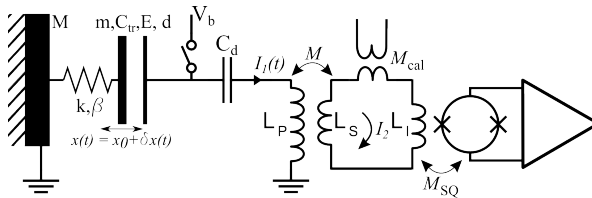
Figure 4.2: Capacitive transducer read-out scheme

If a charged transducer is excited from its equilibrium x_0, its position changes as $x(t) = x_0 + \delta x(t)$. The capacitance and the charge also changes as

$$\begin{cases} q(t) = q_0 + \delta q(t) \\ C_{tr}(t) = C_0 + \delta C_{tr}(t) \end{cases} \tag{4.4}$$

From the electrical point of view the transducer is just a parallel plate capacitor so the force between the electrode and the resonator is

$$F(t) = \frac{Eq}{2} \equiv \frac{q^2}{2\varepsilon_0 A} = \frac{1}{2\varepsilon_0 A}(q_0^2 + 2q_0\delta q(t) + \delta q^2(t)) \approx \frac{q_0^2}{2\varepsilon_0 A} + \frac{q_0\delta q(t)}{2\varepsilon_0 A}. \tag{4.5}$$

From the mechanical point of view the transducer is a harmonic oscillator driven by a force F. We can write down the equation of motion of transducer

$$m(\delta x''(t) + \beta\delta x'(t) + k\delta x) = F(t), \tag{4.6}$$

A standard solution in frequency domain is the Lorentzian shape

$$\delta x(-\omega^2 + \frac{i\omega\omega_0}{Q} + \omega_0^2) = \frac{F(\omega)}{m},$$

$$\delta x = \frac{E\delta q(\omega)}{m(-\omega^2 + \frac{i\omega\omega_0}{Q} + \omega_0^2)} \tag{4.7}$$

We can also write the expression for voltage across the transducer

$$V(t) = \frac{q(t)}{C(t)} = \frac{q_0 + \delta q(t)}{C_0 + \delta C(t)} \approx \frac{q_0}{C_0} - \frac{q_0 \delta C}{C_0^2} + \frac{\delta q}{C_0} = V_0 + \frac{\delta q}{C_0}(1 - \frac{q_0 \delta C}{C_0 \delta q}) \qquad (4.8)$$

given that $\frac{\delta C}{C_0} = -\frac{\delta d}{d_0} = \frac{\delta x}{d_0}$ and $\frac{q_0}{d_0} = E_0$, where d is the transducer gap, we get the final expression for the voltage

$$V(t) = V_0 + \frac{\delta q}{C_0}(1 - C_0 E_0 \delta x(t)) \qquad (4.9)$$

Considering the harmonic calibration current $I(t) = I_0 exp(i\omega t)$ and combining equations 4.7 and 4.9 we can write the expression for the transducer impedance

$$Z_{tr}(\omega) = \frac{1}{i\omega C_0}(1 - \frac{E_0^2 C_0}{m} \frac{1}{-\omega^2 + \frac{i\omega\omega_0}{Q} + \omega_0^2}) \equiv \frac{1}{i\omega C_0} \frac{-\omega^2 + \frac{i\omega\omega_0}{Q} + \omega_0^2 - \frac{E_0^2 C_0}{m}}{-\omega^2 + \frac{i\omega\omega_0}{Q} + \omega_0^2} \qquad (4.10)$$

The expression $\frac{E_0^2 C_0}{m}$ has a dimension of $[Hz^2]$ and is a resonance frequency shift due to electric field in a transducer. A new resonance frequency is $\omega_0'^2 = \omega_0^2 - \frac{E_0^2 C_0}{m}$. We define a coupling factor β^2 a the relative change in resonant frequency

$$\beta^2 = \frac{\omega_0^2 - \omega_0'^2}{\omega_0^2} \equiv \frac{E_0^2 C_0}{m\omega_0^2} \qquad (4.11)$$

The final expression for transducer impedance including the coupling becomes

$$Z_{tr}(\omega) = \frac{1}{i\omega C_0} \frac{-\omega^2 + i\frac{\omega\omega_0}{Q} + \omega_0^2(1 - \beta^2)}{-\omega^2 + i\frac{\omega\omega_0}{Q} + \omega_0^2} \qquad (4.12)$$

It can be shown that the function above has two resonance frequencies(corresponding to $Im(Z(w)) = 0$) where impedance is at it's minimum ω_{res} and maximum ω_{ares} with the ratio of $\frac{\omega_{ares}^2}{\omega_{res}^2} = 1 - \beta^2$. If we generate a constant flux $\Phi_{cal}(\omega) = const$ with the calibration coil, the current generated in the primary and secondary loops of a matching transformer is

$$\begin{cases} I_2(\omega) = \frac{(\Phi_{cal} + I_1(\omega)M)}{L_2} \\ I_1(\omega) = \frac{i\omega M I_2(\omega)}{Z_1(\omega)}, \end{cases} \qquad (4.13)$$

where $L_2 = L_s + L_i$ is the total inductance of the secondary loop and $Z_1(\omega) = Z_{tr}(\omega) + i\omega L_p$ is the impedance of the primary loop. We have neglected the impedance of the decoupling capacitor as it is much smaller then the impedance of the transducer and the primary coil. By combining both equations we get an expression for the current through the input coil of the SQUID

$$I_2(\omega) = \frac{\Phi_{cal}}{\left(L_2 - \frac{i\omega M^2}{Z_1(\omega)}\right)} = \frac{i\omega\Phi_{cal}}{i\omega L_2 + \frac{\omega^2 M^2}{Z_1(\omega)}} \equiv \frac{V_{cal}}{Z_m(\omega)}, \qquad (4.14)$$

where Z_m is the impedance of the measurement circuit as seen from the SQUID input.

It can be shown that the frequency dependence of admittance $Y_m(\omega) = 1/Z_m(\omega)$ can be described by a curve similar to equation (4.12)

$$Y_m(\omega) = A\frac{-\omega^2 + i\frac{\omega\omega_0}{Q} + \omega_0^2(1 - \beta'^2)}{-\omega^2 + i\frac{\omega\omega_0}{Q} + \omega_0^2}, \qquad (4.15)$$

We note that the coupling factor β'^2 is different form the one in equation (4.12). From equations (4.14) and (4.15) we see that for $\omega \ll \omega_0$, $Y_m \approx 1/i\omega L_2 \approx A(1-\beta^2)$. Given that β^2 is typically in the order of $10^{-6} - 10^{-5}$ we get the expression for A

$$A = \frac{1}{i\omega L_2} \qquad (4.16)$$

By sweeping the frequency of the calibration signal and fitting the measured current in the input coil of the SQUID with the equation (4.15) we can measure the equivalent impedance of all modes. As an example, the calibration curves of three most coupled modes for transducer 6 are shown on figure 4.3.
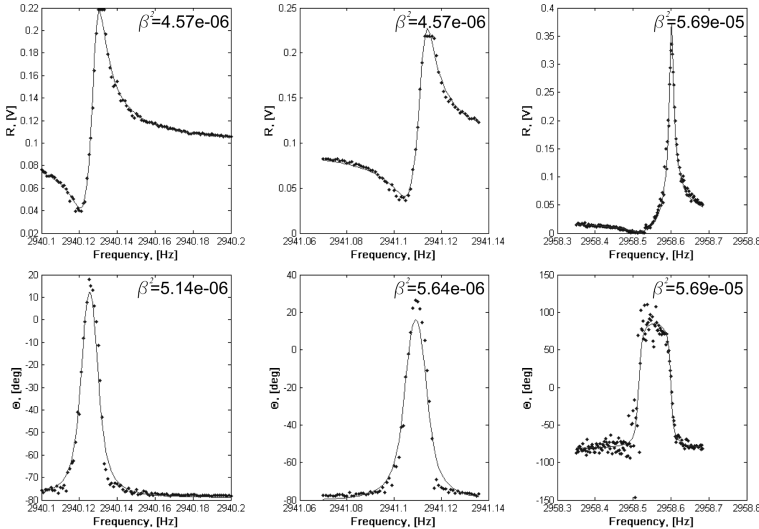

Figure 4.3: Calibration curves of the three most coupled modes

If the modes are only excited by the thermal noise, the current power spectral density around each resonant mode is [65, 67]

$$S_{I,m} = 4k_BT\frac{Q_a}{Q}\,\mathrm{Re}\,(Y_m(\omega)) + S_{vv}(\omega)|Y_m(\omega)|^2 + S_{ii}(\omega) + 2\,\mathrm{Re}\,(S_{iv}(\omega)Y_m^*(\omega))\,,\ (4.17)$$

where S_{vv} and S_{ii} are the power spectral densities of the back-action and additive noise of the SQUID amplifier. S_{iv} is the cross-correlation between these terms. $\frac{Q_a}{Q}$ is the ratio between the measured quality factor, affected by cold damping, and the intrinsic quality factor of the mode.

The contribution of different noise terms to a total noise power spectral density is shown on figure 4.4. The circuit parameters match the design parameters of MiniGRAIL read-out. The resonator and the SQUID temperatures are set to $100\,mK$ and $350\,mK$ respectively.
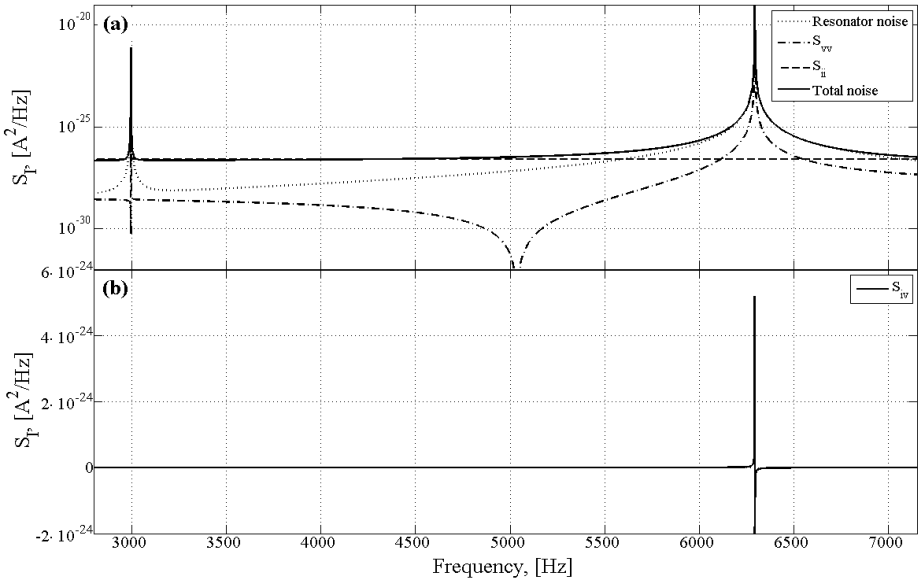
Figure 4.4: Current noise power spectral density at the SQUID input. The curves show the relative contribution of different noise terms from equation (4.17). The circuit parameters match the design parameters of MiniGRAIL read-out. The resonator and the SQUID temperatures are set to $100\,mK$ and $350\,mK$ respectively.

As we can see from the graph, close to the mechanical resonance the contributions of S_{vv}, S_{ii} and S_{iv} terms are small compared to the thermal noise of the transducer. Also, since we have the electrical mode decoupled from the mechanical ones, the cold damping effect is small and $\frac{Q_a}{Q} \approx 1$. As a result, the thermal noise is dominated by the first term in equation (4.17):

$$S_{I,m} = 4k_BT \operatorname{Re}(Y_m(\omega)) = 4k_BT \frac{\beta^2\omega_0^3}{L_2Q} \frac{1}{(\omega_0{}^2 - \omega^2)^2 + \frac{w^2 w_0^2}{Q^2}} \qquad (4.18)$$

The variance of the I_2 due to the thermal noise is given by the integral over the real part of the admittance, which in high Q approximation yields

$$\langle I_2^2 \rangle = 4k_BT \int \operatorname{Re}(Y_m(\omega))d\omega = \frac{k_BT}{L_2}\beta^2, \qquad (4.19)$$

The equivalent temperature of the modes calculated by comparing the measured energy in the resonant peak S_{II} to the expected thermal energy per Kelvin

$$T_{eq,m} = \frac{L_2}{k_B\beta^2} \int S_{II}(\omega)d\omega. \qquad (4.20)$$

Now we can monitor the energy and thus the equivalent temperature of the modes during the operation of MiniGRAIL by using a lock-in amplifier, tuned to the resonance frequency of the mode. But for thirteen modes of MiniGRAIL this would require a use of thirteen amplifiers, which is not realistic. Instead we use an offline software implementation of lock-in amplifier written in Matlab. To exclude the mutual contribution of the neighbouring modes, the data is first filtered with 4-th order Butterworth bandpass filter around the mode frequency and then fed to the lock-in amplifier function. The lock-in time constant was set to 1 s, resulting in 1 Hz integration bandwidth - more than enough for the high Q modes of MiniGRAIL. By repeating the procedure for each mode, we get a full information about the energy stored in the quadrupole modes of the sphere.

The effective temperature of the modes, averaged over one night of the acquisition is shown in the third column of table 4.2

Filtering noisy data

From the average temperature of the modes it is obvious that they are far from thermal noise level and are excited by some external vibrations. Further in this chapter we will try to analyze the cause of this excess noise, but for now we will concentrate on extracting some useful data from our noisy system. If the excitation is stationary there is little we can do. But if the excitation is a periodic or random delta-like signal, which we believe is the case, it acts on the sphere much like a calibration pulse or a gravitational wave. So, we can use standard filtering techniques, developed for resonant detectors [68, 69].

Because of the high mechanical quality factor of the modes, once they are excited it will take hundreds of seconds before the sphere comes to rest, even if the excitation signal is already gone. But because the source of the noise is no more active, the amplitudes of the modes will freely decay to the thermal noise level and any new energy deposited to the sphere will excite the modes again and can be detected. So we need to construct a "peak detection" filter which would emphasize the excitation peaks, but quickly damp the free decay of the sphere after that, effectively lowering

N$_{mode}$	Frequency, $[Hz]$	$\langle T_{eff} \rangle$, $[K]$[a]	$\langle T_{eff}^{filtered} \rangle$, $[K]$[b]	$\langle T_{eff}^{100s} \rangle$, $[K]$[c]
1	2922.45	18642	3095.6	235.9
2	2930.99	285	66.3	23.8
3	2940.11	334	125.6	103
4	2941.13	290	114.3	88.5
5	2958.57	194893	25035.5	753
6	2968.17	237	111.3	14.6
7	2985.42	16192	5598.2	2828.6
8	3007.75	529	206.8	67.4
9	3016.25	3116	531.2	128.2
10	3024.4	1363	805.3	131.9
11	3030.92	21020	3382.7	576.7
12	3043.33	900	998.2	143.3
13	3057.91	2025	674.1	115.1

a – whole night average

b – whole night average after ZOP filter

c – average of 10 most "quiet" $100\,s$ intervals

Table 4.2: Equivalent temperature of the normal modes measured over one night of acquisition.

the Q of the modes. The best solution would be to use an optimal matched filter. Building such a filter would require building a model which describes the spectrum of the normal modes of the sphere [23], which is in case of a complex spectra of real MiniGRAIL setup is hard and computationally extensive task. A simpler, though somewhat suboptimal way is well known for many years [68, 70] and is commonly referred as *zero-order prediction* (ZOP) filter.

Unlike the wideband matched filter, the ZOP filter is applied individually to each mode of the sphere. The ZOP algorithm consists of extracting both quadrature components $x(t)$ and $y(t)$ of the signal at the resonant frequency of the modes (in fact we already did it to estimate the temperature of the modes) and building a difference vector defined as

$$\Delta R_j = \sqrt{(x_j - x_{j-1})^2 + (y_j - y_{j-1})^2}, \tag{4.21}$$

where x_j and y_j are the jth sample of $x(t)$ and $y(t)$ respectively.

The idea of the filter is that for a short lock-in integration time τ_s, much shorter than the decay time of the mode $\tau_0 = \frac{Q}{\pi f_0}$, the variations of the output signal due to the noise are relatively small, while the burst signal will produce a sudden change in the data. The integration time, however has to be high enough not to overdamp the system. The optimal signal-to-noise ratio is achieved when the lock-in time constant is equal to [70]

$$\tau_s^{opt} = \tau_0 \sqrt{(e-1)\frac{S_{wb}}{V_{nb}}\tau_0}, \tag{4.22}$$

where τ_s is the sampling time, τ_0 is a decay time of the mode and $\frac{S_{wb}}{V_{nb}}$ is the ratio between wideband noise spectral density and narrowband noise.

If the condition $\tau_s \ll \tau_0$ is satisfied, the relation between the effective temperature of the mode after filtering and a variance of ΔR is given by the equation [68]

$$\langle (\Delta R)^2 \rangle = \frac{\beta^2}{L_2} k_B T \frac{\tau_s}{\tau_0} \tag{4.23}$$

As an example, the result of applying the described filter to the $2931\,Hz$ mode data is shown on figure 4.5. After the mode is excited to almost $10^4\,K$, it stays excited for more than $200\,s$. On a filtered data, the energy goes down in a few seconds, and the mode is again at the stationary noise level.
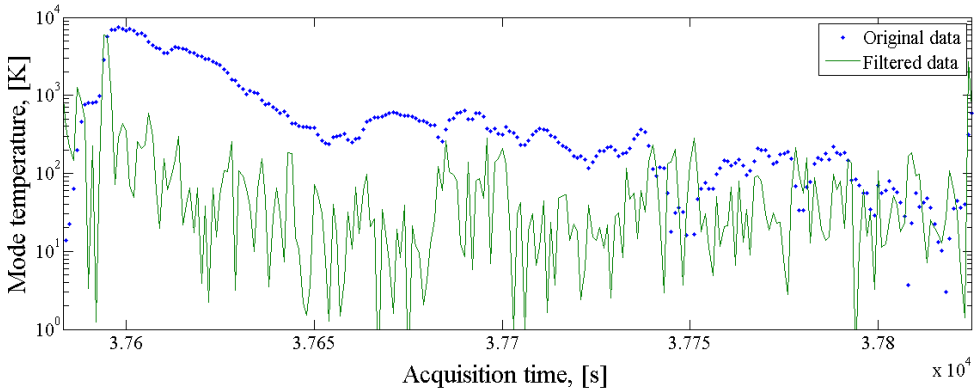
Figure 4.5: The "damping" effect of the zero-order prediction filter.

To look for a "quiet" periods of data we can use for sensitivity calculation, we have applied a running average with the window size of $100\,s$ to the filtered data. The window size is a compromise between the high resolution FFT spectra we need for the modes with a $Q \sim 10^5$, and the number of "quiet" spectra we can average. We have selected 10 regions of data with the average temperature below $30\,K$ (see figure 4.6)

The averaged spectra for two working transducers together with the temperature of the modes is shown on figure 4.7.

Note, that the temperature of even the coldest modes is higher than the ones in table 4.2 because the spectra are made from non filtered data.

Figure 4.6: Equivalent temperature of the "coldest" mode after filtering. Green circles indicate the regions where the average temperature of the mode is below $30\,K$ for at least $100\,s$.

4.2.2   Calibrator's efficiency estimation

Absolute calibrators efficiency

To measure the transfer function of the system we would like to know how much force F^{cal} does the piezo calibrator generate for a given applied voltage V^{cal} - the absolute sensitivity of the calibrators.
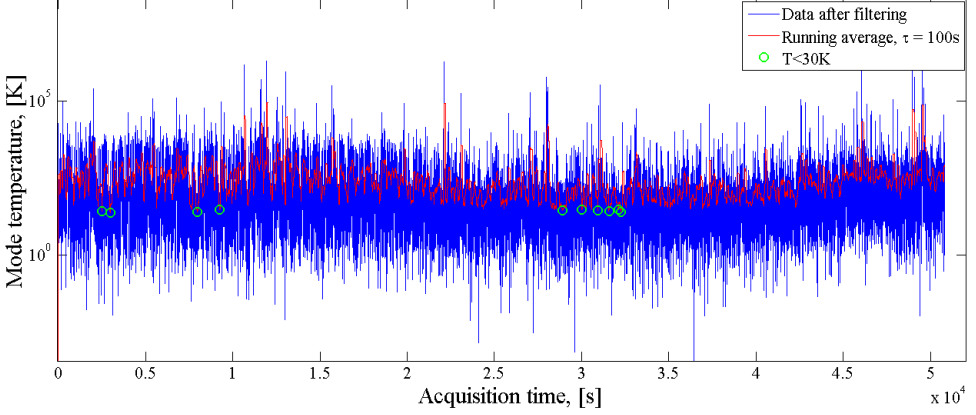
If we apply an impulsive force $F_j^{cal} = F_0 \delta(t)$ to the calibrator j then the force acting on m quadrupole modes is

$$\mathbf{f}_m = \alpha \mathbf{Y}_m(\phi_j, \theta_j) F_j^{cal} \tag{4.24}$$

The modes amplitude response is Lorentzian:

$$\mathbf{a}_m(\omega) = \frac{1}{M(-\omega^2 + i\frac{\omega\omega_0}{Q} + \omega_0^2)} \mathbf{f}_m, \tag{4.25}$$

where M is the mass of the sphere. The displacement of the sphere surface at the calibrator position due to all five modes is

$$q_j = \alpha \mathbf{Y}'_m \mathbf{a}_m \equiv \alpha^2 \mathbf{Y}_m(\phi_j, \theta_j) \mathbf{Y}'_m(\phi_j, \theta_j) \frac{1}{M(-\omega^2 + i\frac{\omega\omega_0}{Q} + \omega_0^2)} F_j^{cal}, \tag{4.26}$$

which corresponds to the equation of motion for a harmonic oscillator with an effective mass

$$M_{eff} = \frac{M}{\alpha^2 \mathbf{Y}_m(\phi_j, \theta_j) \mathbf{Y}'_m(\phi_j, \theta_j)} \tag{4.27}$$
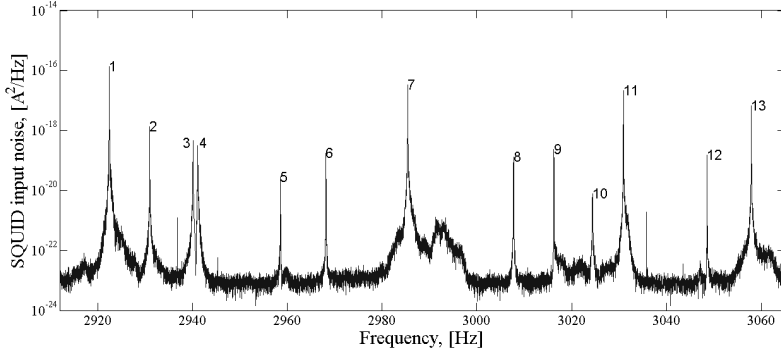
(a) Transducer 4
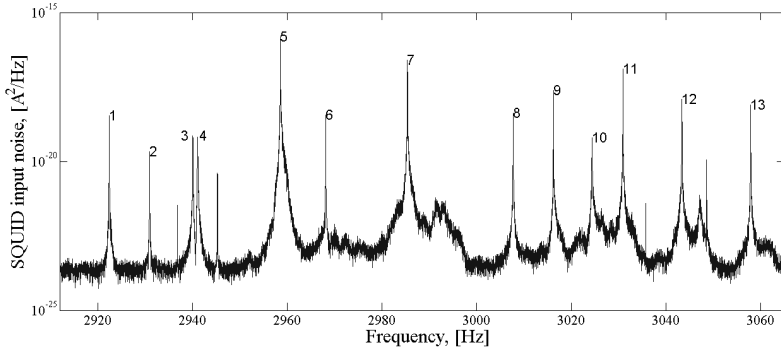
(b) Transducer 6

Mode	Frequency, [Hz]	Temperature, [K]
1	2922.45	5783.0594
2	2930.99	93.4974
3	2940.11	169.977
4	2941.13	235.9964
5	2958.57	15845.3661
6	2968.17	81.3254
7	2985.42	6607.2316
8	3007.75	146.6755
9	3016.25	981.8123
10	3024.4	646.4108
11	3030.92	8545.8511
12	3043.33	342.4096
13	3057.91	1129.668

(c) Effective temperature of the modes

Figure 4.7: The averaged spectra for Transducer 4 (a) and Transducer 6 (b). The averaging is done over 10 most "quiet" regions of data. (c) – the corresponding effective temperature of the modes.

For miniGRAIL $\alpha = 2.9$ and $\mathbf{Y}_m(\phi_j, \theta_j)\mathbf{Y}'_m(\phi_j, \theta_j) = 5/4\pi \approx 0.398$ resulting an effective mass, associated with the normal modes of the sphere to be $M_{eff} \approx 0.3M$

The energy transferred from the calibrator J to the quadrupole modes of the sphere is

$$E = \frac{(F_j^{cal})^2}{2M_{eff}} \tag{4.28}$$

Now we can excite each calibrator with a known voltage and, since we have also done the energy calibration in the previous section, measure the total energy stored in the normal modes of the sphere. From equation (4.28) we can calculate the generated force F_j^{cal} and estimate the efficiency of each calibrator.

The calculated efficiency is almost equal for all calibrators and lies in the order of $1 \times 10^{-2}\,N/V$. A rough estimate of a room temperature calibrator efficiency using a simple model of a mass-loaded spring gives $\sim 10^{-1}\,N/V$. Given that typically piezo crystal performance degrades at low temperatures by a factor of $4-5$, we found the calculated results to be reasonable.

Relative calibrators efficiency

The calibration procedure described above relies on the accuracy of the energy calibration of the modes, which depends on the transducer-mode coupling. We have performed another approach that allows to estimate the relative efficiency of the calibrators.

We assume that the linear combination of calibration excitations that does not produce any quadrupole excitation because is highly symmetric and thus should only excite the monopole mode of the sphere. If we have a set of J equivalent calibrators, then the combination of calibrators forces that excite only the monopole mode are given by

$$\mathbf{F}_j = \mathbf{B}_{mj}^{-1}\mathbf{F0}_m, \tag{4.29}$$

where $\mathbf{F0}_m = [1, 0, 0, 0, 0, 0]$ is the modes force vector, where the first unity amplitude represents the monopole mode and 5 zeros are the amplitude of quadrupole modes forces. Here and in the rest of this chapter we use 6×6 $\mathbf{B}$ matrix, which includes the monopole mode (see section 1.2.4 in chapter 1). Also we omitted the radial eigenfunction coefficient α, as it does not influence the result. Now if we apply the calculated $\mathbf{F}_j$ vector to the real calibrators transfer functions and multiply it by a pattern matrix $\mathbf{B}_{mj}$ the result will be non-zero forces, acting on quadrupole modes. Our task is then to find such a vector $\mathbf{F}'_j = \mathbf{F}_j\mathbf{e}_j$ for which the resulting modes excitation is $\mathbf{F0}_m$. Vector $\mathbf{e}_j$ is the inverse of relative calibrators efficiency ϵ_j. The result of such calculation for both working transducers is shown on figure 4.8. Calibrator 7 transfer function is given for comparison. The amplitudes of the quadrupole modes are clearly reduced by at least one order of magnitude.

We found that fitted efficiency comes in reasonable agreement between two transducers and is also consistent with rough room temperature estimation in section 4.2.3
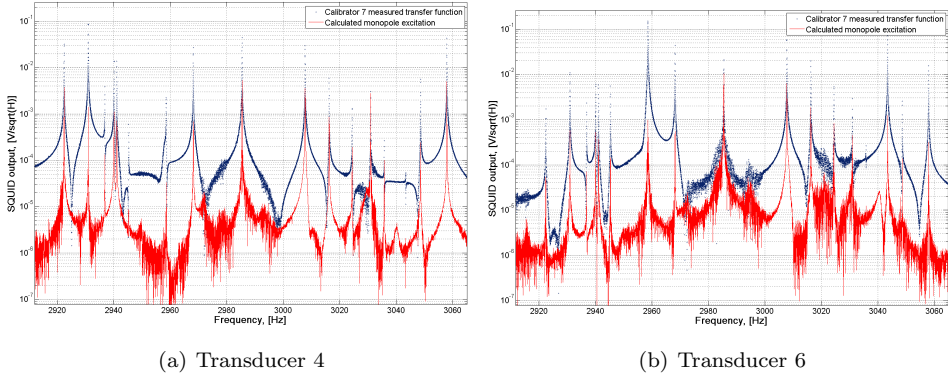
(a) Transducer 4

(b) Transducer 6

Figure 4.8: Monopole mode excitation compared to the Calibrator 7 transfer function

	Cal1	Cal2	Cal3	Cal4	Cal5	Cal6
Energy calibration	0.7861	0.8537	1.0	0.8226	0.9016	0.8921
Room temp Calibrator7 fit	0.63	0.60	1.0	0.60	0.80	0.61
Monopole mode fit Tr4	0.6043	0.5630	0.9660	0.6952	0.5657	0.5273
Monopole mode fit Tr6	0.5955	0.5692	1.1319	0.6304	0.5269	0.5017
Ratio Tr4/Tr6	0.9855	1.0110	1.1717	0.9068	0.9313	0.9514

Table 4.3: Calibrators efficiency ϵ calculated from fitting transfer functions of six calibrators to monopole excitation

(table 4.3). We have also noticed that the calibrators efficiency obtained from the energy calibration is more uniform than the one from the monopole mode fitting. We believe this is because the fitting procedure "automatically" compensates the non-ideality of the MiniGRAIL sphere which becomes more obvious further in this chapter.

4.2.3 Direction reconstruction

In this section we show the results of the direction reconstruction algorithms, described in chapter 1, applied to the real data of MiniGRAIL. We use the Calibrators 1-6 to measure the full transfer function of the system and a signal from Calibrator 7 simulating the candidate GW signal, coming from unknown direction. The direction reconstruction procedure is similar to calibrators efficiency estimation algorithm. If $Fq_7(\omega)$ is the force that Calibrator 7 applies to the sphere, the forces acting on the normal modes are

$$\mathbf{Fa}_m(w) = \epsilon_7 \mathbf{Y}_m(\phi_7, \theta_7) Fq_7(\omega), \tag{4.30}$$

where (ϕ_7, θ_7) is the position of Calibrator 7 which is not known and ϵ_7 is the efficiency of the Calibrator 7, which is just a scaling factor. The forces $\mathbf{Fq}_{1..6}(\omega)$ that Calibrators 1-6 have to apply to produce the same modes forces are given by

$$\mathbf{Fq}_j(\omega) = \mathbf{e}_j \mathbf{B}_{mj}^{-1} \mathbf{Fa}_7(\omega) = \epsilon_7 \mathbf{e}_j \mathbf{B}_{mj}^{-1} \mathbf{Y}_m(\phi_7, \theta_7) Fq_7(\omega) \equiv \lambda \mathbf{Y}_m(\phi_7, \theta_7) Fq_7(\omega), \tag{4.31}$$

where $\lambda = \epsilon_7 \mathbf{e}_j \mathbf{B}_{mj}^{-1}$ is a constant vector because $\mathbf{B}_{mj}$ depends only on Calibrators 1-6 positions, which is known and fixed, ϵ_7 and $\mathbf{e}_j$ we have calculated by fitting the monopole mode in section 4.2.2.

Now we can vary ϕ_7 and θ_7 until the error between measured $Fq_7^{meas}(w)$ and calculated $Fq_7^{calc}(w)$ force amplitudes is minimized. We calculate the fitting error as

$$\xi = \sum_\omega |\log(\frac{q_7^{meas}(\omega)}{q_7^{calc}(\omega)})|. \tag{4.32}$$

Here, we use a base 10 logarithm of the amplitudes relation to equalize the weight of the fitting error between the resonances and antiresonances.

Room temperature results

We have performed the first tests on the sphere with transducers at room temperature in normal atmospheric pressure. Because the transducers are damped by air, the quality factor of the modes was very low. However we could verify that all calibrators are working properly before closing the cryostat. The measurements were done with a transducer mounted on transducer position 4. Transducer was enclosed in a small vacuum cap and charged to $142\,V$. The transfer functions were acquired by frequency sweeping the excitation signal and measuring the response with a lock-in amplifier.

Because of the low quality factor of the modes we did not actually fit the Calibrator 7 transfer function. Instead we measured ϕ_7, θ_7 and used the calculated $\mathbf{Y}_m(\phi_7, \theta_7)$ to check the calibrators. In fact, we have found that 2 calibrators had an inverted polarity and fixed them before closing the Dewar. We have also roughly estimated the relative efficiency of the calibrators. These are the room temperature values listed in table 4.3.

Low temperature results

Cryogenic calibration was done at a temperature of $1\,K$. To save time we used an impulse calibration instead of frequency sweeping the calibration signal.

We have tried two fitting approaches which we will further refer as "Fit1" and "Fit2".

With a "Fit1" we used the equation (4.31) and fitted values of ϕ_7 and θ_7 . A result of the fitting is shown on figure 4.10 in red. We found that the agreement between the fitted curve and the measured data was reasonably good. The calculated Calibrator 7 position was consistent between two acquisition channels, but was more than $20\,\%$ off the measured values.
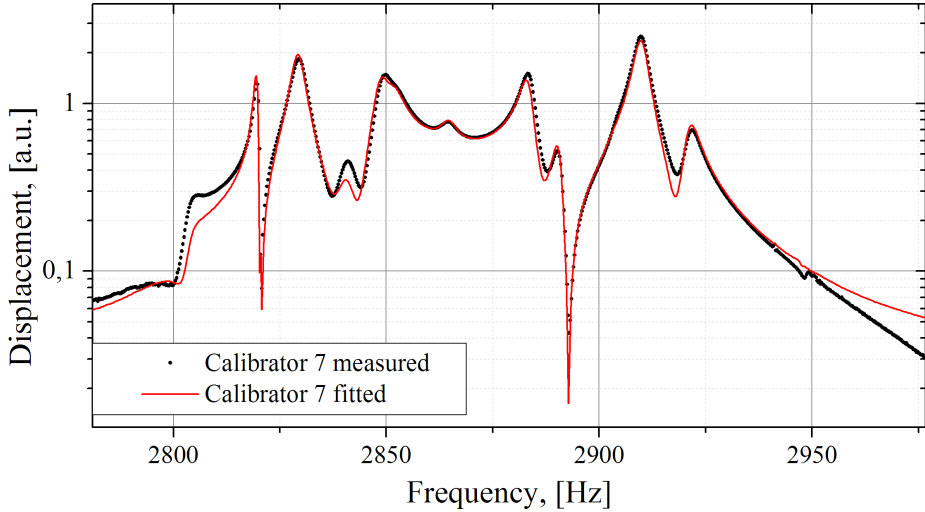
Figure 4.9: Room temperature fit of Calibrator 7 transfer function.

In another approach("Fit2") we have tried to find such a linear combination $\mathbf{a}_j$ of Calibrators 1-6 transfer functions that produces the best fit of the Calibrator 7 transfer function. The major difference of this approach is that $\mathbf{Fa}_j$ does not necessarily correspond to a real excitation applied to the sphere surface and in principle should not necessarily produce a physically meaningful result. On the other hand if the shape of the spherical harmonics of MiniGRAIL deviates from the theoretical shape for the ideal sphere we can still fit the data. The result of the second fit is shown on figure 4.10 in green. The fit is clearly better than the first one. We can still try to calculate Calibrator 7 position by converting the vector $\mathbf{a}_j$ to a mode channels $\mathbf{g}_m$ and calculating a detector response matrix. The eigenvectors of the response matrix show the orientation of the deformation ellipsoid, as described in section 1.2.1. Surprisingly, the values of ϕ_7 and θ_7 obtained from "Fit2" were much closer to the measured ones. The shape of the deformation ellipsoid, however was very distorted. For an ideal sphere the maximum radial deformation is at the location of the calibration impulse, and two radial deformations in the orthogonal directions have an opposite sign and half amplitude. The calculated deformation ellipsoid is very asymmetric - the deformations in orthogonal directions are not equal. However, their sum is equal to the main axis deformation, so the volume is preserved. We believe that the reason of such deviation is either in a structural imperfection of the sphere, like a non uniform density distribution, or in a non uniform stress induced by the sphere suspension. We also noticed that the frequency distribution of the normal modes of the uncoupled sphere is different from the theoretical ones calculated in [19]. As a simple solution we have tried to introduce an amplitude and angular distortion to the

	Measured	Fit1		Fit2	
		Ch4	Ch6	Ch4	Ch6
ϕ, $[deg]$	33	40.8	41.6	36.8	35.8
θ, $[deg]$	51	61.6	61.1	48.3	48.5

Table 4.4: Calculated Calibrator 7 position compared to the measured one. Fit1 is made by using an elastic model of an ideal sphere. Fit2 is done by fitting Calibrator 7 with a linear combination of Calibrators 1-6 transfer functions.

spherical harmonics in equation (1.4), but the results were not consistent anymore between the acquisition channels. The results of both fits are summarized in table 4.4

Effect of calibration signal jitter

To increase the signal to noise ratio, the transfer function of each calibrator was measured for 20 times and then averaged. During the averaging we noticed that the relative amplitudes of the peaks are changing. We have discovered that the problem was in the time stability of the calibration pulse. Originally we used a software triggered calibration - a LabView program starts the acquisition and after a time delay sends a command to the function generator to generate a calibration pulse.
Let's consider a frequency domain representation of a calibration signal. If we apply a discrete Fourier transform defined as

$$X_k = \sum_{n=0}^{N-1} x_n e^{-\frac{2\pi i}{N}kn} \qquad k = 0, \dots, N-1 \tag{4.33}$$

to the delta-like calibration signal with amplitude A and at sample index j, the corresponding frequency domain signal will be

$$X_k = A e^{-\frac{2\pi i}{N}kj} \qquad k = 0, \dots, N-1, \tag{4.34}$$

The amplitude and phase of the calibration signal in frequency domain are

$$R_k = |X_k| = A$$
$$\varphi_k = \arctan(\frac{\text{Im}(X_k)}{\text{Re}(X_k)}) = \arctan(\frac{\sin(\frac{2\pi kj}{N})}{\cos(\frac{2\pi kj}{N})}) = \frac{2\pi kj}{N} \tag{4.35}$$

The amplitude R_k is constant in frequency, just as we want for a calibration signal, but the phase is changing by 2π radians every $kj = N$. If the time and thus the index j of calibration pulse is not stable, the slope of the phase will vary from acquisition to acquisition.

To overcome this effect we have set up a hardware double triggered calibration - first trigger starts the ADC card acquisition and the second one triggers the function generator to send a calibration pulse. The time delay between two trigger signals is
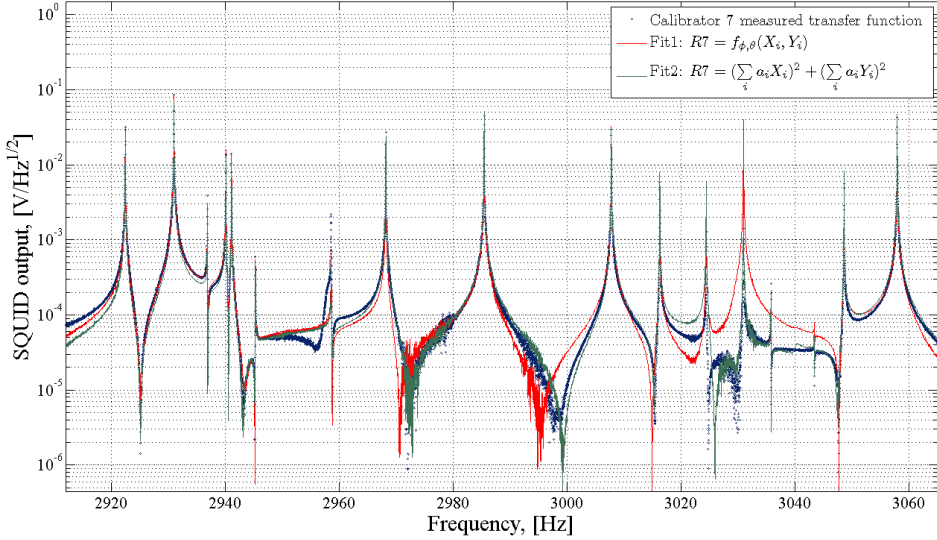
(a) Transducer 4
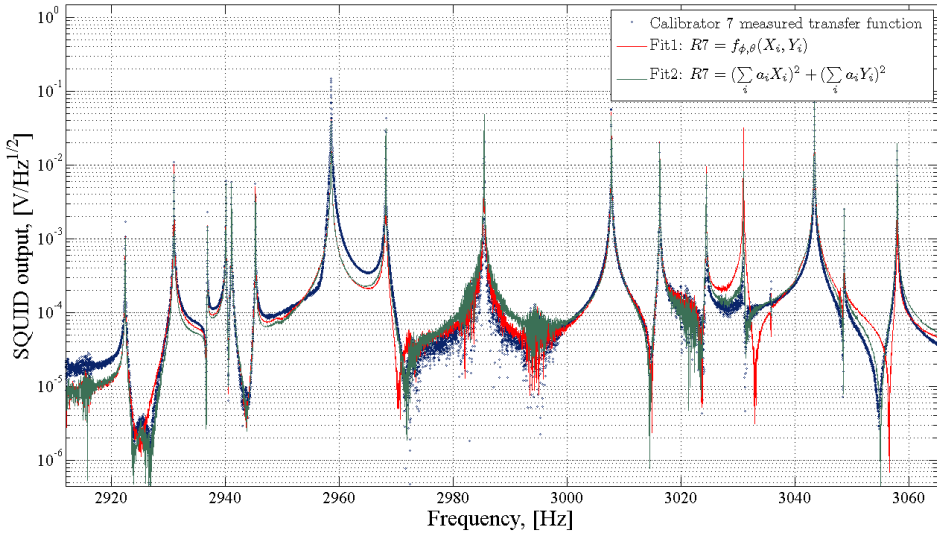
(b) Transducer 6

Figure 4.10: Calibrator 7 transfer function fit

Figure 4.11: Two quadrature components of a $2922.45\,Hz$ mode transfer function acquired multiple times with software(a) and hardware(b) triggering. Software triggering introduces a phase jitter making averaging impossible.

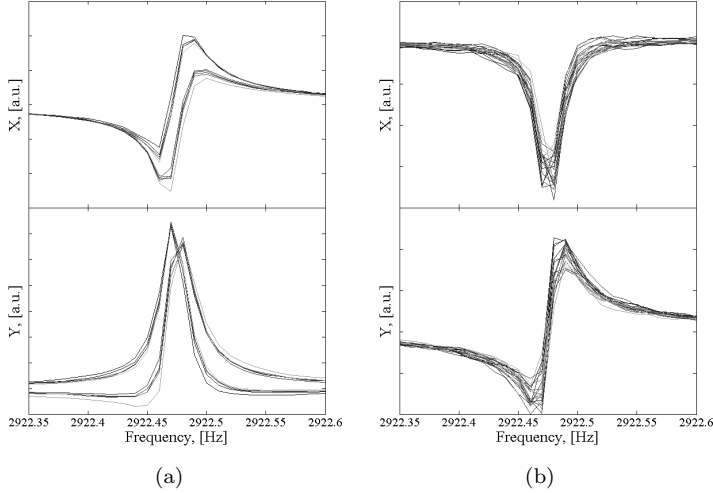also done with hardware timer. To further improve the stability we are also acquiring the calibration signal and subtracting its phase from the phase of the measured transfer function. The real and imaginary parts of the $2922.45\,Hz$ mode transfer function, measured with software and hardware triggering is shown on figure 4.11. On figure 4.11(a) the phase is clearly bistable, corresponding to values of j varying by 1.

4.3 Strain sensitivity

From chapter 1 we recall that the force induced by an incident gravitational wave to the sphere can be decomposed in five quadrupole components F_m:

$$F_m(t) = \frac{1}{2}R\chi M\ddot{h}_m(t), \tag{4.36}$$

or in frequency domain[28]:

$$F_m(\omega) = \frac{1}{2}\omega^2 M\chi R\, h_m(\omega) = \frac{1}{2}\omega^2 M\chi R\mathbf{T}_V \left[\begin{array}{c} h_+(\omega) \\ h_\times(\omega) \end{array} \right], \tag{4.37}$$

where R, M are the sphere radius and mass, $\chi = 0.327$ is an effective length and h_m are gravitational wave spherical amplitudes, related to two polarizations states of a gravitational wave by means of conversion matrix $\mathbf{T}_V$.

What we measure at the output of the detector is not the force, but the current density at the input coil of the SQUID amplifier. The five components of the force $F_m(\omega)$ are converted to six current outputs I_j by a rectangular 6×5 transfer matrix $\mathbf{Tf}_{jm}$. So to go back from measured currents to forces we need to inverse the $\mathbf{Tf}$ matrix. In case of at least 5 (or even 4 with some limitations[32]) transducers the system is fully determined so we can invert the transfer matrix and construct statistically independent mode channels to perform a coherent data analysis as described in chapter 1.

In our case, we only have 2 working transducers. Of course it is not possible to reconstruct 5 quadrupole amplitudes by measuring only at 2 positions of the sphere, so the system is underdetermined. In principle, since the modes are non-degenerate, we can see all the quadrupole modes individually in each transducer output spectrum (see figure 4.7). Since we have measured the transducer-mode coupling for each mode, we can calculate the amplitudes of the modes at the transducer position and thus do the direction estimation. In practice, however, we were not able to clearly identify the modes in the MiniGRAIL spectra.

What we can still do is to combine the transfer functions we have measured from 6 calibrators, to simulate the gravitational wave excitation of the sphere from any direction, defined by two polar angles β and γ:

$$Tf(\beta, \gamma) = \left(\mathbf{Tv}(\alpha, \beta, \gamma) \left[\begin{array}{c} h_+(\omega) \\ h_\times(\omega) \end{array} \right] \right)' \mathbf{B}(\beta_c, \gamma_c) \mathbf{Tf}_c(\omega), \quad (4.38)$$

where α is the polarization angle of gravitational wave which is not known beforehand. So for simplicity we set $\alpha \equiv 0$ and build the sky sensitivity map for every transducer by varying β and γ

$$S_{hh_j}(\omega, \beta, \gamma) = \frac{S_{I_j}(\omega)}{Tf(\omega, \beta, \gamma)}, \quad (4.39)$$

where S_{I_j} is the noise current power spectral density at the SQUID input. Close to the resonance the output noise is limited by the detector noise, and the outputs of the transducers are correlated. For that reason we can not sum the signal-to-noise ratios of the transducers. Instead we took the minimum of two transducers sensitivity, which is correct at the resonance, but a factor $\sqrt{N_{tr}}$ suboptimal at the regions where the transducers noise is not correlated.

The strain sensitivity curves from an optimal direction for "plus" and "cross" polarized gravitational wave are shown on figure 4.12. As expected from the high equivalent temperature of the modes, it is quite far from $4.2\,K$ thermally limited sensitivity(dashed line). The $4\,K$ sensitivity plot is made with exactly the same system properties, but with the energy of the modes set to thermal. The $20\,mK$ plot is done by setting the equivalent temperature of the modes to 20mK and increasing the coupling of the modes by a factor of 3 to match the design value of transducers bias field. Around the resonant peaks the best sensitivity of two transducers is taken, same as for measured curve. In the uncorrelated parts of the spectra, dominated by the SQUID additive noise, we took the sum of SNR of two transducers, resulting an

(a) h_+, $(\beta = 50^o \, \gamma = 180^o)$

(b) $h_\times$, $(\beta = 55^o \, \gamma = 120^o)$
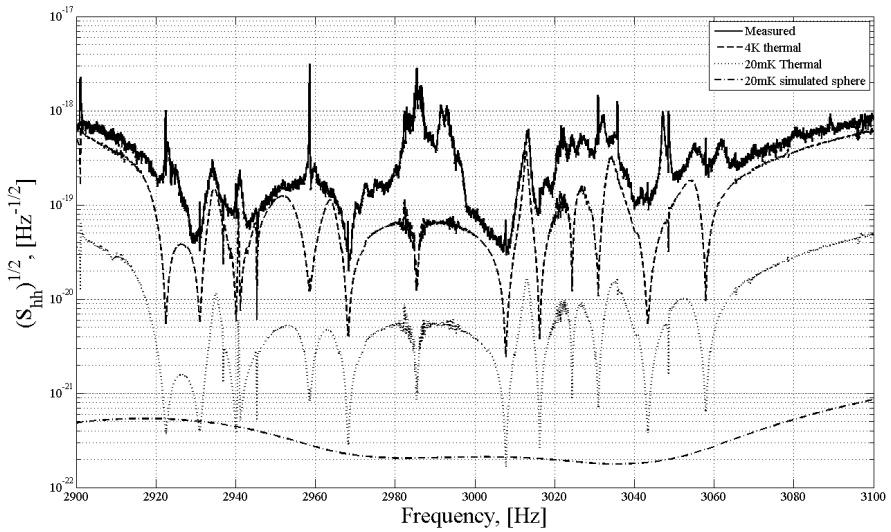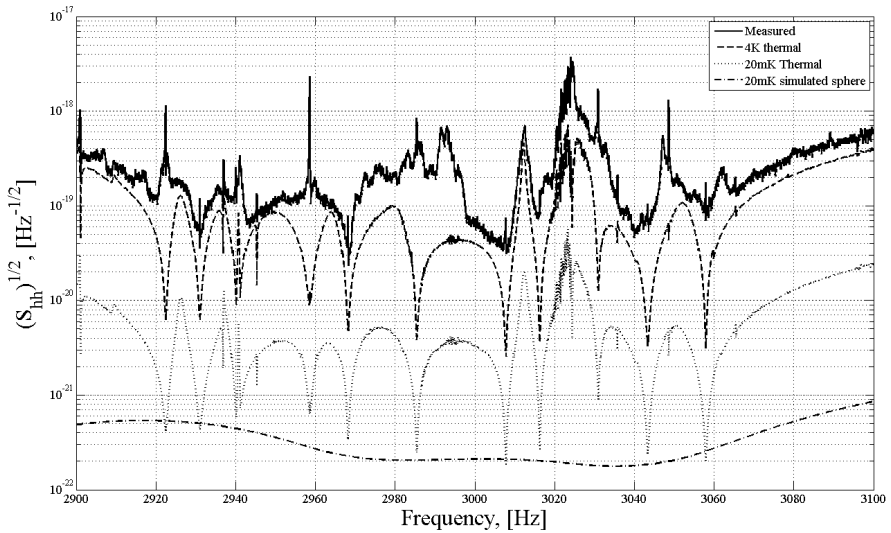
Figure 4.12: Best strain sensitivity from two transducers combined for "plus" (a) and "cross" (b) polarized gravitational wave. The sensitivity is calculated for best SNR direction for each polarization. The $4\,K$ and $20\,mK$ thermal strain sensitivities are made by generating a thermally limited noise spectra and 3 times increased coupling for $20mK$ data. Simulated data is taken from [32]

improved wideband sensitivity. The simulated curve is made by building a numeric model of the sphere with transducers and read-out circuit[32][1].

For both polarization states, the measured sensitivity curves were very similar with a best peak strain sensitivity of $3 \times 10^{-20}\,Hz^{-1/2}$ and a strain sensitivity of $1 \times 10^{-19}\,Hz^{-1/2}$ over a bandwidth of $42\,Hz$. That is about factor 2 worse than the 5 K nearly thermally limited sensitivity reported in [25]. For the $4.2\,K$ thermally limited noise spectra and current system parameters we would reach a peak strain sensitivity of $2.6 \times 10^{-21}\,Hz^{-1/2}$ even with only 2 working transducers. The peak sensitivity level for current configuration and thermodynamic temperature of the sphere of $20\,mK$ is about $2 \times 10^{-22}\,\mathrm{Hz}^{-1/2}$

In order to compare the sensitivity to other detectors we calculate the integral sensitivity parameter - the minimal detectable Fourier amplitude of gravitational wave burst which is defined as

$$H_0(\omega, \beta, \gamma) = \frac{1}{\sqrt{SNR}} = \frac{1}{\left(\int \frac{1}{S_{hh}(\omega,\beta,\gamma)} \frac{d\omega}{2\pi} \right)^{1/2}} \tag{4.40}$$

The measured sensitivity curve on figure 4.12 corresponds to a gravitational wave burst with a Fourier amplitude $H_0 = 8 \times 10^{-21}$ or an energy of $T_N = 2.3$ K. A calculated 20 mK sensitivity would yield $H_0 = 1 \times 10^{-22}$ and the pulse detection noise temperature[2] $T_N = 4.5 \times 10^{-4}$ K, which is about 1.5 times better than the one of Auriga [72], which is the most sensitive resonant detector at the moment.

A directional dependence of the integral sensitivity for both GW polarizations is shown on figure 4.13(a,b). The third plot on figure 4.13(c) shows the strain sensitivity to the calibration pulse. While having obviously no meaning in terms of gravitational waves sensitivity, it is given to compare the calculated sky sensitivity with a simple model described in section 4.1. The H_0 plot on figure 4.13 is somewhat different from the one on figure 4.1(c) because of influence of the modes coupling to the transducer, but it is clearly more uniform than the sensitivity plot with the degenerate modes on figure 4.1(b). It is also a good illustration that for a spherical detector a mechanical excitation of the sphere is not fully identical to gravitational waves excitation. We have discussed that in section 1.2.4 of chapter 1.

4.4   Conclusions

For the first time we have cooled MiniGRAIL down in a full 6-transducer configuration, capable of omnidirectional detection. During the run we have faced two serious

---

[1]A simulated 20 mK sensitivity plot on figure 4.12 is much smoother than the one estimated by us for two reasons. First, non working transducers do not contribute in sensitivity, instead they are extracting the energy from the system at their resonant frequency. They appear as antiresonances on the transfer function and as sharp dips on the sensitivity plot. Second, the value of the wideband SQUID noise in [32] is calculated by using a Clarke-Teshe model[26] and appears to be much lower than the noise achievable with a practical SQUID amplifier we use.

[2]The pulse detection noise temperature, T_N, is defined by $E = k_B T_N$, where E is the energy deposited to the sphere by a gravitational wave resulting in $SNR = 1$ [71]

(a) h_+ polarized GW. $H_0 = 8.4 \times 10^{21}$ (b) $h_\times$ polarized GW. $H_0 = 7.9 \times 10^{21}$

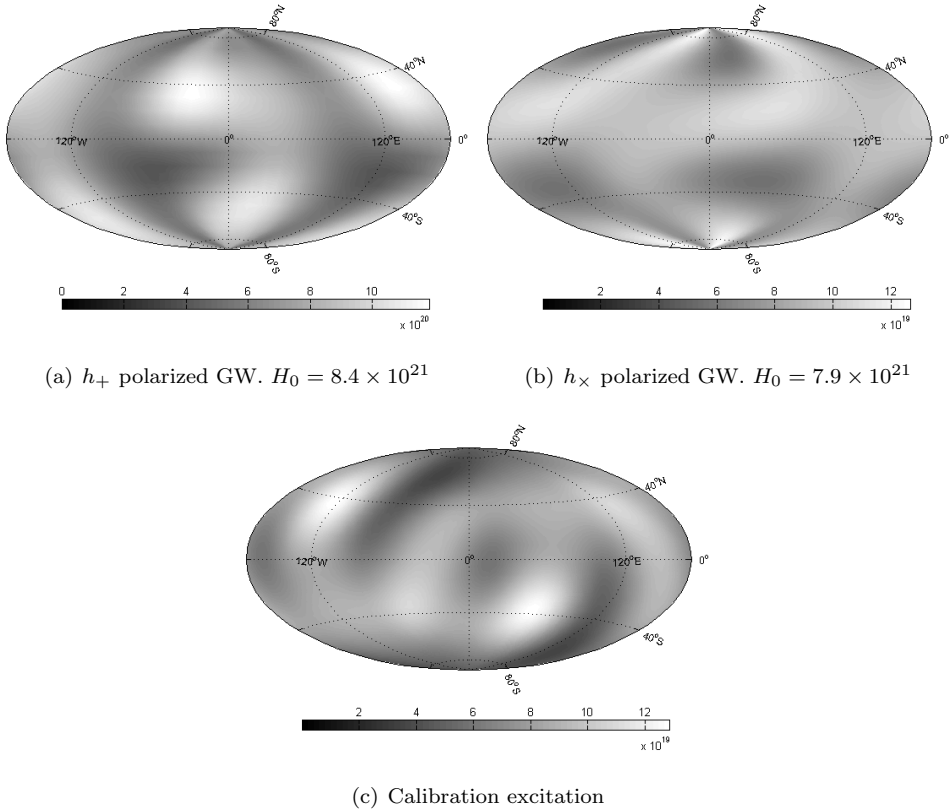

(c) Calibration excitation

Figure 4.13: The minimal detectable Fourier burst amplitude versus the direction for two polarizations of gravitational wave and calibration excitation

problems: Transducers failure and excess vibrational noise. We could measure the capacitance and charge transducers through a bias line up to the temperature of about $40\,K$, but failed to bias the transducers at $4.2\,K$. We have discovered that the reason was that the reed switches we have used contained exchange gas, which was not clearly indicated in a datasheet. Exchange gas would condense and freeze on the electrodes at low temperatures and block them. We could heat up the switches by sending a short high current pulse to the coil of the switch and restore the operation, but that would disturb and warm up MiniGRAIL as well. Another problem we have discovered is that the long and very soft shielded wires we used to connect the transducers to the charging lines (see figure 1.10) were attracted by the electrode's electric field and were touching the electrodes with the shield, shorting them to ground. These issues can be easily fixed before the next cool down. After finishing the current run and opening the cryostat we have discovered that all the transducers were still working.

Concerning the second problem, since we have already reached a thermal noise level in previous runs, there is obviously no fundamental problem with the suspension of the sphere. Before this run we have changed the old copper "jelly-fish" thermal links with new thicker ones to improve their thermal conductance at the cost of damping. Also since it is the first time we have cooled down MiniGRAIL with all 6 transducers and 7 calibrators, the amount of wires going to the sphere and the last mass have increased a lot. For the next cool down we are planning to add an extra vibration insulation stage for the cables, suspended from mixing chamber or $50\,mK$ plate.

The two problems, described above resulted that only two out of six transducers were operational and far from thermal noise. The data analysis pipeline of MiniGRAIL is based on the fact that a spherical detector is a multichannel detector. But since the transducers outputs are correlated around the resonance, we need to convert them to uncorrelated mode channels, which correspond to five spherical amplitudes of a gravitational wave. This means that to build a fully determined system we would need to have at least 5 working transducers. For the 2 transducers configuration we had in this run, the system is underdetermined and the data analysis capability is limited. However, all the calibration and direction reconstruction routines we have developed during this run are made as general as possible and do not depend on the number of transducers. This should allow us to make a calibration and estimate the strain sensitivity of MiniGRAIL within a few days in any future run. As for the current run, we were able to determine the "unknown" position of Calibrator 7 with the accuracy of about $10-20\%$, depending on the fitting algorithm. A more precise fitting, constrained to the elastic properties of the sphere gives a higher fitting error, clearly indicating that the behaviour of MiniGRAIL sphere is different from the model of an ideal sphere. the deformation ellipsoid shape, calculated from the best fit is asymmetric. While the fitted results are still reasonably good, we do not have a clear understanding of the reasons of inconsistency and need to perform more tests with more calibration impulse directions, to verify the consistency of the algorithms. Fortunately these tests can also be done at room temperature.

While the sensitivity was heavily affected by the vibrational noise, we have measured a best peak strain sensitivity of $3 \times 10^{-20}\,Hz^{-1/2}$ and a strain sensitivity of $1 \times 10^{-19}\,Hz^{-1/2}$ over a bandwidth of $42\,Hz$, which is factor 2 worse then the $5\,K$ nearly thermally limited sensitivity reported in [25]. This corresponds to a gravitational wave burst with a Fourier amplitude $H_0 = 8 \times 10^{-21}$ or an energy of $T_N = 2.3$ K.

The calculations show, that for the $4.2\,K$ thermally limited noise spectra and current system parameters we would reach a peak strain sensitivity of $2.6 \times 10^{-21}\,Hz^{-1/2}$ even with only 2 working transducers.

The ultimate sensitivity level for current configuration and thermodynamic temperature of the sphere of $20\,mK$ is about $2 \times 10^{-22}\,Hz^{-1/2}$, yielding $H_0 = 1 \times 10^{-22}$ and $T_N = 4.5 \times 10^{-4}$ K. This is about 1.5 times better than H_0 of Auriga [72]- the most sensitive resonant detector at the moment.

Unlike the mechanical part of MiniGRAIL, the electrical read-out part gave no problems. With improved magnetic shielding, redesigned 2-stage SQUIDs and a "cold damping" network, adapted for differential SQUID electronics, the acquisition system

was stable and robust.

Currently, we are planning to fix the issues mentioned above and perform a new run with hopefully all 6 transducers working before the end of 2011. After that the future of MiniGRAIL project is still unclear.

Chapter 5

SQUID detector for MRFM experiment

5.1 Introduction

In this chapter we present the first results of using the low noise SQUID amplifiers, we have developed for MiniGRAIL project, to detect a displacement of nanomechanical resonator used for magnetic resonance force microscopy (MRFM) experiment.

Currently, the most commonly used technique to detect the motion of ultrasensitive mechanical resonators is optical interferometry. Its applications range from Magnetic MRFM experiments [73], investigation of quantum effects in mechanical systems [74] and as we have already mentioned, gravitation wave experiments [5].

Unfortunately, despite the excellent sensitivity, the interferometric technique has a number of disadvantages:

- Optical detection becomes hard to implement when the size of the resonator is pushed to the nanoscale, because of the diffraction limit. For visible light wavelength one would in principle need a mirror of a few microns diameter, limiting the minimal width and the mass of a cantilever, while we are aiming to use cantilevers with diameters in order of a tenth of nm.

- When low or ultralow temperatures are required to reduce the thermal force noise, as for single spin MRFM, resonator heating due to light absorption is found to limit the effective cooling of the resonator [75]. This problem can be partially circumvented only by substantially reducing the input light power, at the price of reducing the displacement sensitivity.

- Excess heating caused by laser light might also be the cause of increased damping of the cantilever in a proximity of the sample surface, also called non-contact friction [76, 77, 78]. This effect is currently the limiting factor of MRFM sen-

sitivity. We hope that the fact that our force sensor allows operation at much lower temperatures can help to find ways to address this issue.

Other techniques have been recently demonstrated to be more compatible with ultralow temperatures. In particular, both Single Electron Transistors (SET) [79] and microwave cavities [80, 81, 82] have demonstrated outstanding displacement sensitivity for the detection of nanomechanical resonators at temperatures below 100 mK. So far, however, their implementation has been limited to systems where detector and resonator are tightly integrated, which is not practical for scanning probe applications like MRFM. Moreover, for microwave techniques the direct photon absorption still remains an issue at millikelvin temperatures, which again can only be mitigated by reducing the input power. Displacement sensors based on Quantum Point Contacts have also been demonstrated in an off-board setup [83], but so far their use has been limited to liquid helium temperature.

The SQUID-based technique we propose does not involve direct power dissipation in the resonator, and therefore is particularly suitable for ultralow temperature applications. Also, since the noise of the SQUID amplifier scales with temperature, the detection sensitivity should improve when going to ultralow temperatures. In practice however, due to reduced electron-phonon coupling (see section 3.5.4 in chapter 3), the SQUID noise saturates at $T = 250 - 500$ mK so the signal-to-noise ratio will not improve below that temperature.

5.2   MRFM

In a conventional magnetic resonance imaging (MRI) detection scheme, the sample is placed in a strong homogeneous magnetic field B_0 which results in Zeeman splitting between the nuclear spin states. The energy difference between the two states is

$$\Delta E = \gamma \hbar B_0 \ , \tag{5.1}$$

where γ is the ratio of magnetic dipole moment of a spin to its angular momentum, called "gyromagnetic ratio". If the sample is then exposed to a radio-frequency (rf) magnetic field with frequency that satisfies the condition

$$\omega = \frac{\Delta E}{\hbar} = \gamma B_0, \tag{5.2}$$

then the system absorbs energy from the rf radiation resulting in transitions between the nuclear spin states. From a classical point of view, the total nuclear magnetic moment of the sample starts changing its orientation. Once the rf field is turned off, any component of the total moment remaining perpendicular to the static field is left to precess about this field. The precession of this ensemble of nuclear magnetic moments produces a time-varying magnetic signal that can be detected with a pickup coil. The electric current induced in the coil is then amplified and converted into a signal that is proportional to the number of nuclear moments (or spins) in

the sample. In MRI this signal can be reconstructed into a 3D image of the sample using spatially varying B_0 field and Fourier transform techniques. While being a very powerful and widely used technique, Magnetic Resonance Imaging (MRI) has certain limitations. One of them is the minimal detectable number of spins resulting in a limit in volume resolution. Currently, the smallest volume element should contain $\approx 10^{12}$ nuclear spins [84, 85] or $\approx 10^6$ electron spins [86] for Nuclear Magnetic Resonance and Electron Spin Resonance microscopy respectively leading to a spacial resolution of a few microns.

By combining MRI with Probe Microscopy technology - MRFM technique is aimed for the ultimate MRI resolution improvement: detection of a single electron spin or even a single nuclear spin. So far a sensitivity, required to measure the single electron spin was already achieved by using an optical readout technique.[87]
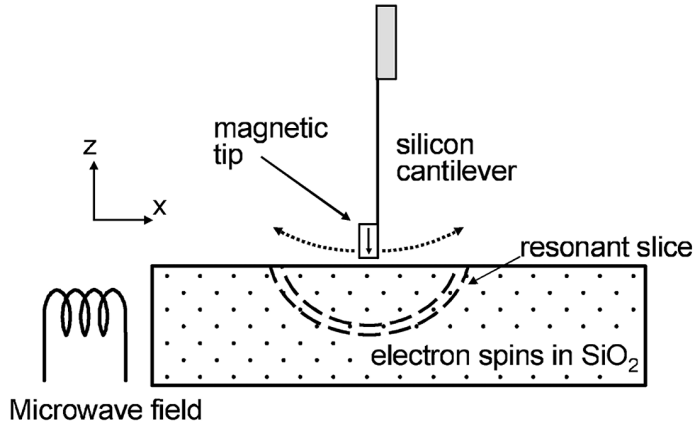

Figure 5.1: Scheme of MRFM experiment[88]

In an MRFM experiment, a magnetic particle mounted on the end of a cantilever generates a strong B_0 field gradient(in order of $10^5 - 10^6 \, T/m$). A microwave field excites the magnetic resonance in the region that satisfies the condition $B_0(x, y, z) = \omega/\gamma$, where ω is the frequency of the RF field. The resonant region is confined to a thin, approximately hemispherical "resonant slice" around the magnetic particle. The radio frequency signal is modulated so that the spins are cyclically inverted at the cantilevers mechanical resonance frequency, typically a few kHz. When modulated at resonance with the cantilever oscillation frequency, even the weak magnetic force induces detectable vibrations of the cantilever. By probing the resulting vibrational motion of the cantilever, it is in principle possible to detect spins with molecular or atomic resolution. By scanning the sample in 3D through this resonant region, a spatial map of the nuclear spin density can be made.

5.2.1   Sensitivity requirements

The interaction force between the tip and the spin is given by a dipole force which is proportional to the magnetic moment of the spin and the field gradient at the spin position. These forces are extremely small - the interaction force between a single electron spin and the magnetic tip is easily calculated to be as small as 10^{-17} N. For a single proton the force is even smaller- in the order of 10^{-20} N.

We can characterize the detection sensitivity of MRFM experiment in terms of a signal-to-noise ratio which is given by the ratio of the magnetic force due to the interaction with the spins to the force noise of the cantilever. For small volumes of spins, we measure statistical spin polarizations and the SNR is given by

$$SNR = N \frac{(\mu_N G)^2}{Sf\Delta f},$$ (5.3)

where N is the number of spins, μ_N is the magnetic moment, G is the B_0 field gradient, S_f is the force noise spectral density of the cantilever and Δf is the measurement bandwidth, determined by the spin relaxation rate.

From equation (5.3) we see that the sensitivity of the nanomechanical resonators, used for MRFM experiments is limited by their force noise. According to the fluctuation-dissipation theorem, the power spectrum of the force noise power spectral density, acting on the cantilever is given by

$$S_f = \frac{4K_B Tk}{Q\omega_0},$$ (5.4)

where k is the cantilever spring constant, $K_b T$ is the thermal energy, Q is the mechanical quality factor, and ω_0 is the resonance frequency. For a cantilever the ratio k/ω is given by [89]

$$\frac{k}{\omega_0} \propto \frac{t^2 w}{l},$$ (5.5)

where l, w, and t are its length, width and thickness.
Thus the force noise of the cantilever can be reduced by achieving low operation temperature, high quality factor and by increasing the length of the cantilever and reducing the cantilevers width and thickness.

5.3   Experimental setup

5.3.1   Dilution refrigerator

Since we are aiming for continuous measurement at very low temperatures (as low as 10 mK, or even below 1 mK for the future MRFM experiments), the only option is a dilution refrigerator. We are using a commercial pulse-tube dilution refrigerator from Leiden Cryogenics [54]. Using the 2-stage pulse-tube cooler instead of a liquid helium bath and 1K pot greatly simplifies the maintenance and operation of the cryostat.

However this comes to a price with increased cool-down time and vibrations that the pulse tube induces on the mixing chamber. While, for our system, cool-down time is comparable to the one of a normal dilution refrigerator, the higher vibration level can be a problem for a vibration sensitive experiment like MRFM. To reduce the effect of mechanical vibrations, we have made some modifications both to the cryogenic and room temperature part of the cryostat. A general view of our experimental setup is
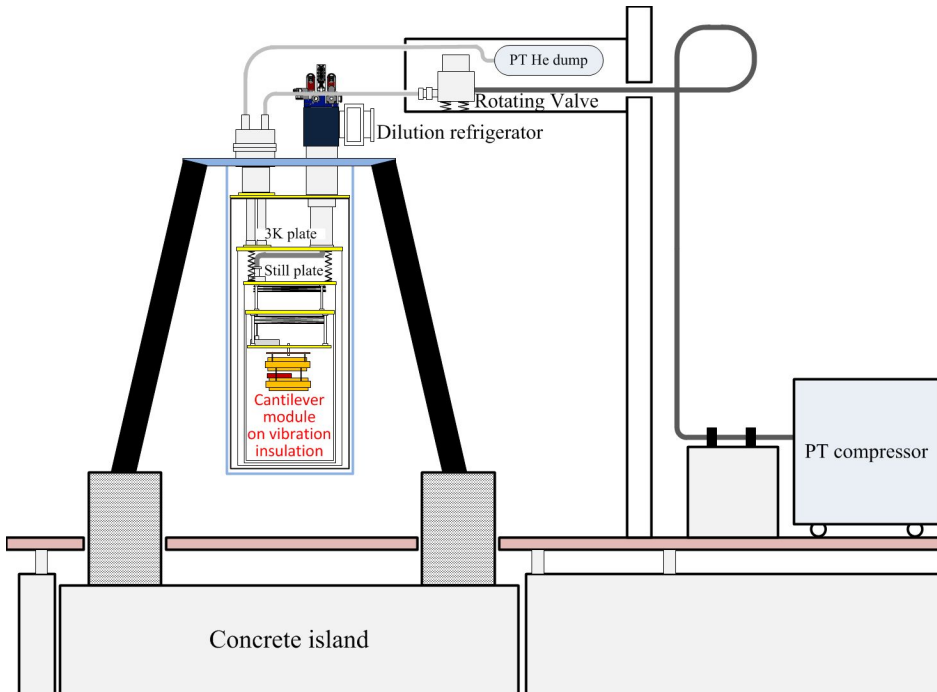

Figure 5.2: The scheme of the experimental setup. The cryostat is installed on a concrete island, which is mechanically decoupled from the rest of the laboratory building. The inner part of the cryostat, below the 3K plate, is suspended on a springs. Additional 2-stage mass-spring isolation system is installed below the mixing chamber.

shown on figure 5.2. Below we will describe the modifications we have made to each part.

Room temperature modifications

To decouple the cryostat from the environment noise, it is installed on a vibration-free concrete island which is very well insulated from the rest of the building and from other experimental setups. The legs supporting the Dewar are filled with sand in order to increase their stiffness and damping. But, as we have found, the major source of external noise are the vibrations of the pulse-tube compressor and periodic
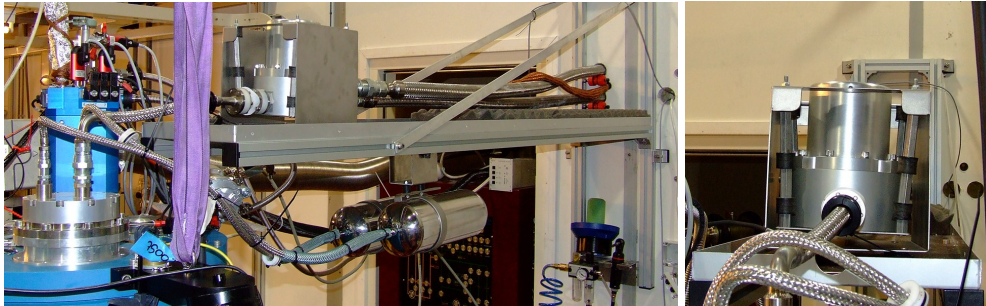
Figure 5.3: The rotating valve, suspended inside a box, attached to the wall of the laboratory. The periodic expansion of the tubes induces the motion of the valve, rather then pushing the PT head.

expansion of the flexible lines going from the compressor unit to rotating valve and from rotating valve to PT head. We have installed the compressor unit in the separate corridor behind the measurement hall and the long (20m) hoses, connecting it to the pulse-tube are attached to the concrete blocks. The rotating valve is freely suspended inside a box, attached to the wall (see figure 5.3), so that the expansion of the tubes induces the motion of the valve, rather then pushing the PT head. The box is also covered by acoustically insulating material in order to reduce the acoustic noise in the working space.

Cryogenic part modifications

Even if the vibrations from room temperature part of pulse-tube are damped, there is still some vibration coming from the cold part of a PT itself. The frequency ranges from the base frequency of the pulse-tube of 1.4 Hz up to few kHz. The low frequency vibrations are induced by periodic expansion and contraction of thin stainless steel PT walls due to He gas pressure oscillations inside PT. High frequency 'whistling' comes from He flowing in the cold head and flexible hoses [90] and upconversion of low frequency vibrations, shaking the cryostat.

To reduce the vibrations to an acceptable level we have replaced the rigid links between 3K Plate and still plate with a spring suspension with resonance frequency of $3-5$ Hz (figure 5.4(a)), depending on the suspended weight. Since the resonant frequency of the suspension is quite close to the pulse-tube frequency, we have also installed a magnetic damper to reduce the amplitude of vertical motion of the lower stage.

For further attenuation we have installed a vibration insulation consisting of 2 5 kg masses suspended on springs with a resonant frequency of 120 Hz. The total attenuation of the two masses system is calculated by Finite Element Analysis software to be above 100 dB in a frequency range 1-5 kHz. We measured an attenuation of
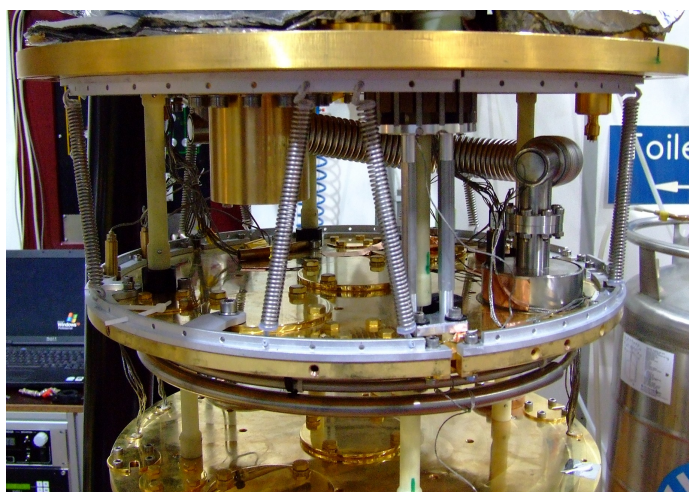
(a) 3K Plate - Still suspension
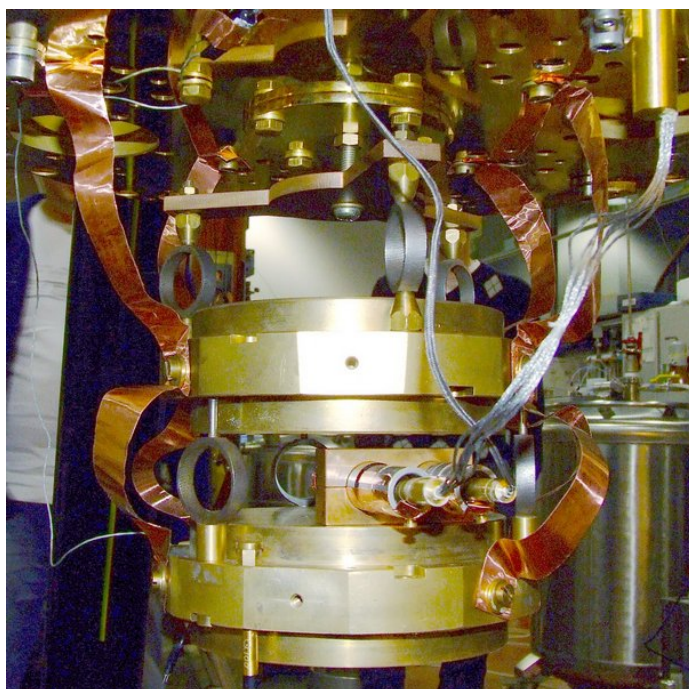
(b) Double mass-spring vibration insulation

Figure 5.4: Low temperature vibration insulation of the cryostat.

about 50 dB between the first mass and the mixing chamber, and a total attenuation of ≥ 60 dB in the frequency range of interest. (See figure 5.5).
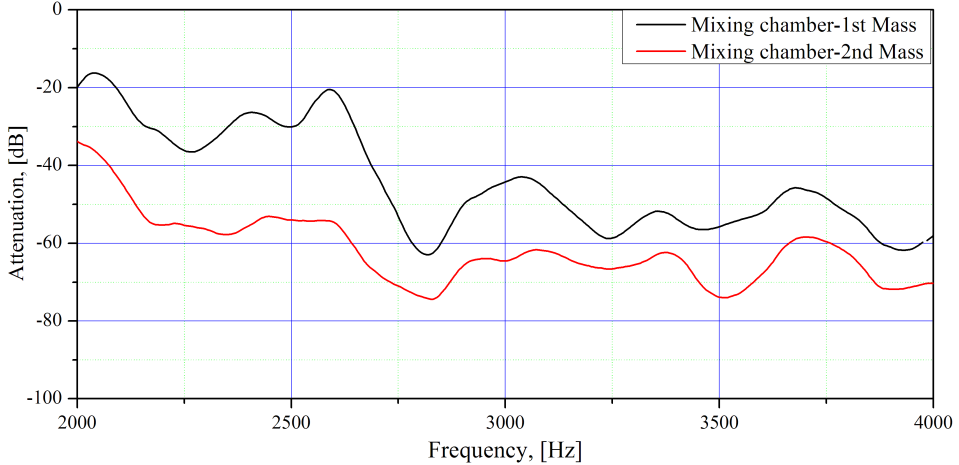

Figure 5.5: Mechanical attenuation between the mixing chamber and the two masses of vibration insulation measured at room temperature in air. The total attenuation of double mass system (red line) is above 60 dB in the frequency range of interest.

Since the experiment is now both mechanically and thermally decoupled from the mixing chamber, we need to provide a good thermal contact without degrading the vibration insulation. We used a soft commercial 20×0.2 mm Cu tape, attached with the screws to a mixing chamber and the masses (see figure 5.4(b)). With the mixing chamber being at a temperature of 8 mK the gradient between the mixing chamber and the second suspension mass was less then 3 mK.

The noise spectral densities at the SQUID output of the original and modified cryostat are shown on figure 5.6. As we see even when the pulse-tube is turned off, the vibration insulation system significantly improves the insulation of the cryostat from the environmental mechanical vibrations. With PT on we hardly see any additional vibrational noise above the frequency of ~ 100 Hz.

5.3.2 Cantilever chip

In our experiment, we have used two types of cantilevers.

The first one consisted of a $50 - 70$ μm 100 nm thick SiC nanowire, attached to a Si AFM chip by means of electron induced Pt deposition. While, with this type of cantilever it is possible to make the resonator with optimal length, diameter and potentially very high quality factor [91], the cantilevers we have produced did not show any improvement in damping factor compared to the second type of cantilevers. That, combined with the extreme fragility, made us concentrate on the second type.
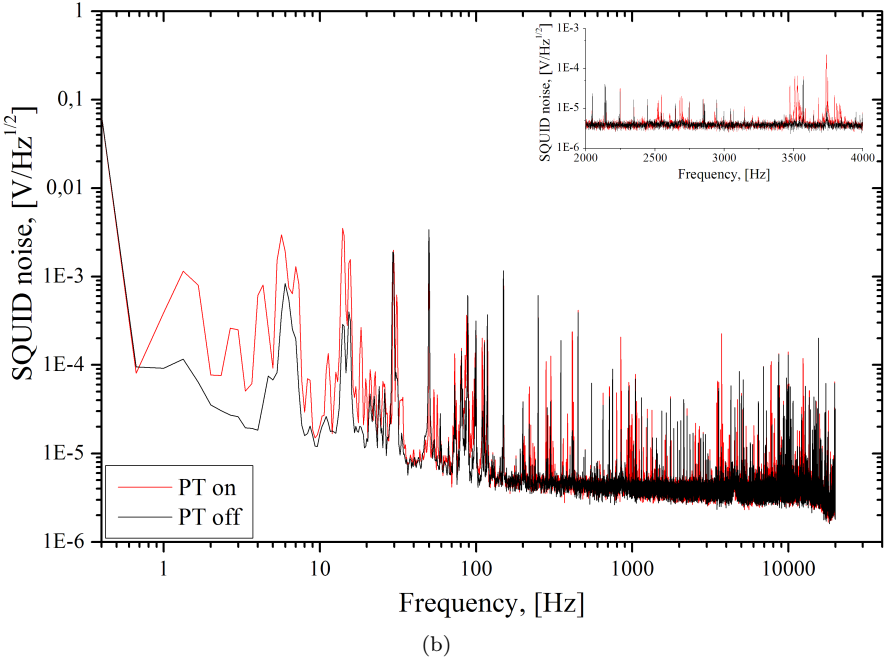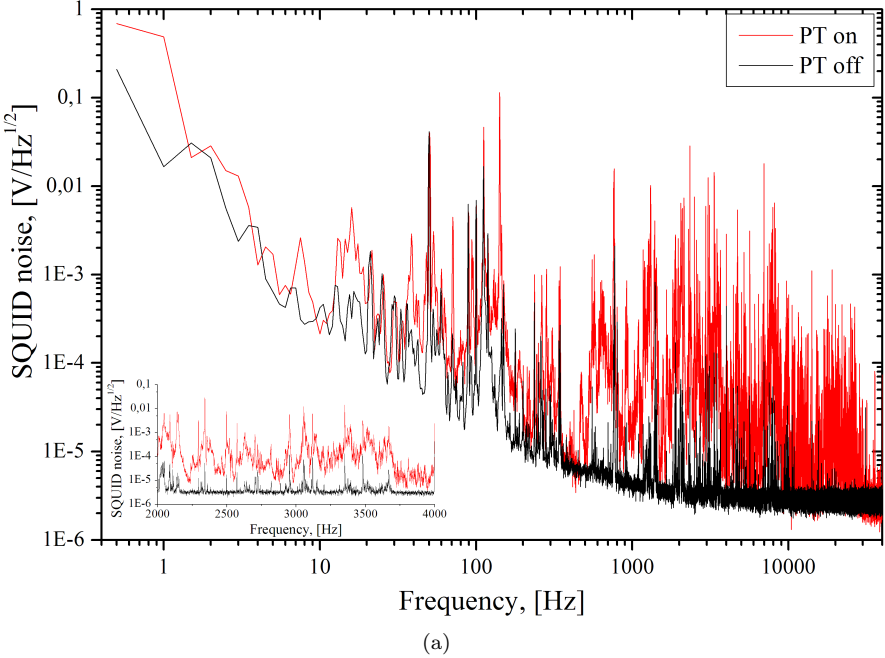
(a)

(b)

Figure 5.6: Vibrational spectral density measured by a SQUID on initial (a) and current (b) setup.
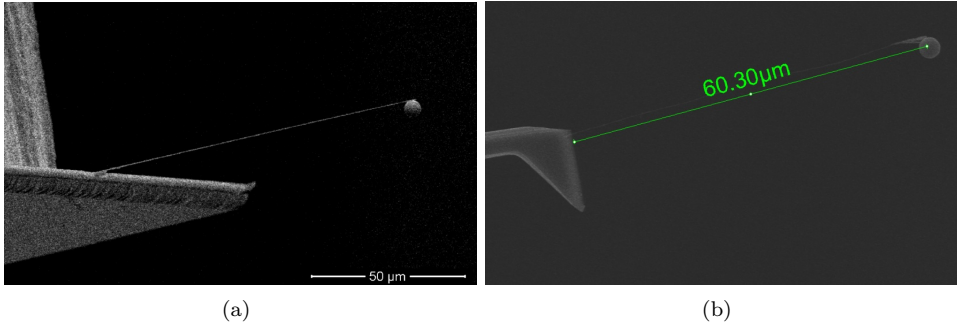
(a)   (b)

Figure 5.7: An electron microscopy image of the silicon resonator with a magnetic sphere attached to its end. (a)- the single crystal beam is 100 nm thick, 5 μm wide and 100 nm long. The 4.5 μm diameter magnetic sphere is made of a neodymium based alloy with remanence $B_r = 0.75$ T. The frequency of the lowest flexural mode of the resonator is 3084 Hz, with a quality factor of 3.8×10^4. (b) - An AFM chip with 60.3 micron long, 100 nm diameter SiC nanowire with 3.6 μm spherical magnet attached to its end.

The second type was a silicon resonator consisting of a 100 nm thick,5 μm wide and 100 μm long single crystal beam, fabricated as reported in [92].

For both types we attached a $4-5$ μm diameter magnetic sphere of a Neodymium based alloy (MQP-S-11-9-20001-070 from Magnequench) to the end of the resonator using a nano-manipulator inside an electron microscope [93], and magnetized it in a 3 T field at room temperature. The alloy has a nominal remanence field $B_r = 0.75$ T, and the estimated magnetic moment of the magnetized particle is $\mu = 2.8 \times 10^{-11}$ J/T.

Mechanical properties of two types of cantilevers are summarized in table 5.2

	Si beam	SiC nanowire
Length, [μm]	~ 100	$50 - 70$
Width [μm]	5	0.1
Thickness, [μm]	0.1	0.1
Spring constant, [N/m]	1.5×10^{-4}	$2 - 5 \times 10^{-5}$
Magnet diameter, [μm]	$4 - 5$	$4 - 5$
Resonant frequency, [kHz]	~ 3	$1.5 - 2$
Quality factor @ 4.2 K	3×10^4	1×10^4
Damping, [Nm/s]	$\sim 10^{-13}$	$\sim 10^{-13}$

Table 5.1: Summarized properties of cantilever and detection chain parameters

5.3.3   Cantilever module

The cantilever module is made similar to the SQUID modules used in MiniGRAIL project[25](see figure 5.8). The cantilever, pickup and calibration coils are mounted on the pc-board fixed on a lead-plated copper holder. Nb can with CryoPerm foil around it provide a magnetic shielding. The pickup coil is connected to a SQUID module with Nb braided twisted pair superconducting wire.

The resonator is placed at about 10 μm above the edge of the detection coil. The silicon chip supporting the resonator is held in position and thermally anchored to a copper holder by a brass spring. The detection coil has square geometry with 22 windings, a width of 670 μm and an estimated inductance of 0.6 μH. The coil is connected to the input coil of a two-stage SQUID amplifier, made of a commercial Quantum Design sensor SQUID and a flux transformer dc SQUID. The SQUID is operated with commercial direct readout electronics from Star Cryoelectronics. We have also placed a small piezo crystal inside the module to be able to excite the cantilever mechanically.
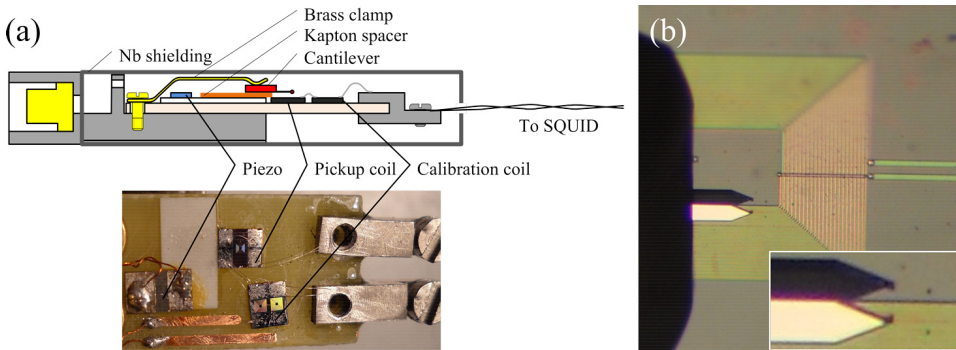
Figure 5.8: (a) - Cantilever module. (b) - Cantilever chip with a SiC nanowire resonator aligned above the inner edge of a detection coil. The small dark dot to the right of the AFM chip is the magnetic particle.

5.3.4   Detection scheme

The idea of the experiment is very simple and is shown on figure 5.9 A cantilever with a small magnetic particle, attached to its end, is placed at a close distance (20-50 um) from a superconducting pickup coil, coupled to a squid. The motion of a magnetic particle results in a change of magnetic flux in the coil and induces the current which is measured by the SQUID. The calibration coil is used to measure the coupling between the Cantilever and the pickup coil (see section 5.5).

Parameter	Value
Pickup coil inductance, L_p	600 nH
Pickup coil size (IDxOD)	$230x670$ μm
Pickup coil number of turns	2x22
Pickup coil linewidth	2 μm
Calibration coil inductance, L_cal	$18\,nH$
Calibration coil mutual inductance, M_{cal}	$15\,nH$
SQUID input coil inductance, L_i	1.6 μuH
SQUID input coil mutual inductance, M_i	$10\,nH$

Table 5.2: Summarized properties of cantilever and detection chain parameters
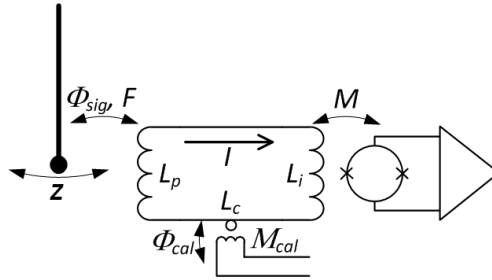
Figure 5.9: Scheme of cantilever motion detection using SQUID read out.

5.4   Optimizing the sensitivity

In order to optimize the coupling between the magnetic particle and a pickup coil we need to find a position where the motion of the magnetic particle with dipole moment **m** in a given direction(x, y, z) results in the maximum flux change ($\phi_x = \frac{\delta\phi}{\delta x}$, $\phi_y = \frac{\delta\phi}{\delta y}$, $\phi_z = \frac{\delta\phi}{\delta z}$) in the pickup coil.

We calculate the flux generated by the magnetic dipole in the coil by solving the inverse problem - by calculating the magnetic field **B** and its gradients $\boldsymbol{\Delta}B_x$, $\boldsymbol{\Delta}B_y$, $\boldsymbol{\Delta}B_z$ at the position of a magnetic particle, generated by current (I_c) in the pickup coil.

A magnetic dipole can be modelled as a small current loop, with Area **A** and a current i. Dipole moment of such a loop will be

$$\mathbf{m} = i\mathbf{A} \tag{5.6}$$

Magnetic flux (ϕ_c) induced in the pickup coil by a current loop and magnetic flux induced in the loop by a current in the coil (I_c) are:

$$\phi_c = iM \tag{5.7}$$
$$\phi_l = I_cM, \tag{5.8}$$

where M is the mutual inductance between the current loop and the pickup coil, then

$$\phi_c = \frac{i\phi_l}{I_c} = \frac{iA\frac{\phi_l}{A}}{I_c} = \mathbf{m}\frac{\mathbf{B}}{I_c},$$ (5.9)

where $\mathbf{B}$ is the magnetic field at dipole position.

For the current layout of the experiment the magnetic particle is magnetized in the direction of its motion, perpendicular to the coil plane, so we are only interested in the sensitivity in the z direction:

$$\phi_z = \mathbf{m}\frac{\frac{\partial B_z}{\partial z}}{I_c}.$$ (5.10)

The magnetic field B, generated by the pickup coil, can be calculated by using the Biot-Savart law:

$$\mathbf{B} = \frac{\mu_0}{4\pi}\int\frac{I_c d\mathbf{l}\times\mathbf{r}}{r^3},$$ (5.11)

where dl is a vector, whose magnitude is the length of the differential element of the wire, and whose direction is the direction of current, B is the net magnetic field, μ_0 is the magnetic constant, $\mathbf{r}$ is the full displacement vector from the wire element to the point at which the field is being computed.

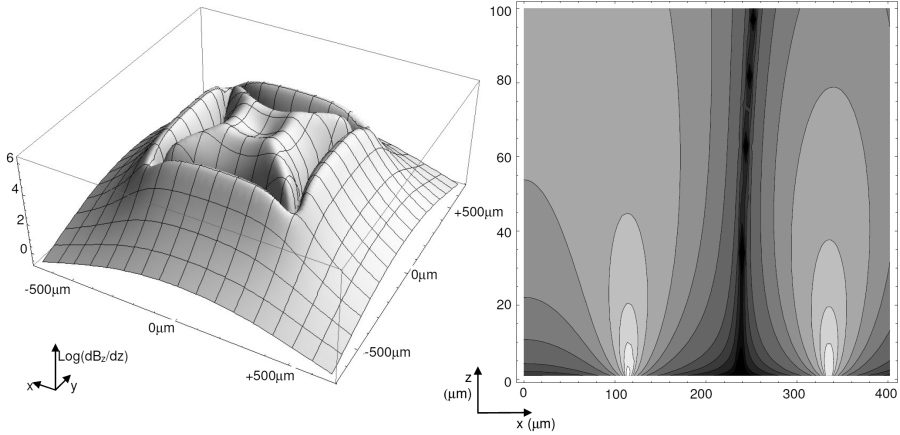**Figure** 5.10: Left: position sensitivity of pickup coil to the magnetic dipole located at 50 μm above the coil surface. Right: cross-section of the sensitivity plot with the y-plane. [94].

To simplify the calculations the pickup coil is approximated by a single loop, with uniform current density. The coil is placed in the (x,y) plane. The dipole is parallel to z axis.

The results of a calculation of the vertical gradient of the field $\frac{\partial B_z}{\partial z}$ versus the position of the cantilever above the coil is shown on figure 5.10. The vertical distance between the cantilever and the pick-up coil is set to 50 μm.

5.5   Measuring the Cantilever Coupling

5.5.1   Cantilever-SQUID calibration

In order to estimate the force noise of the cantilever we need to measure how effective does the cantilever motion converts to a current in the SQUID pickup coil. In other words, we have to measure ϕ_z from equation 5.10. We consider the same layout as in the previous sections: the pickup coil and the cantilever are placed parallel to the xy plane, and we detect the motion of the magnetic particle in z direction.

The calibration procedure is similar to the one ve have used to calibrate MiniGRAIL modes coupling in the previous chapter. We have inserted a small transformer between the detection and the SQUID input coil. The inductance of the secondary coil of the calibration transformer L_C is made small enough not to contribute to the total inductance of the detection loop. Since the magnetic flux through the superconducting loop is preserved, the injected calibration flux $\Phi_{cal}(\omega)$ will generate a change in the screening current I. The force, acting on the cantilever in the z direction from a magnetic field B, generated by the screening current in the pickup coil is given by

$$F = \mathbf{m}\nabla\mathbf{B_z} \equiv \phi_z I \tag{5.12}$$

We can write a set of equations describing the cantilever behaviour:

$$\begin{cases} \Phi_{cal} + \Phi_{sig} + L_{tot}I = 0 \\ (-\omega^2 + \frac{i\omega_0}{Q}\omega + \omega_o{}^2)z = \frac{F+F_{th}}{m} \approx \frac{F}{m} \end{cases} \tag{5.13}$$

The first equation represents the magnetic flux conservation in a superconducting loop. $L_{tot} \equiv L_p + L_i + L_c + L_{par}$ is the total inductance of the pickup loop including the unknown parasitic inductance L_{par}. Φ_{sig} is the flux that cantilever motion induces in the pickup coil. The second equation is the standard equation of motion of a driven harmonic oscillator. In principle, we should take into account both the force F due to the calibration current and a thermal noise force F_{th}, but we consider the calibration signal to be high enough to dominate in the system, and ignore any other force sources. Since $F = \phi_z I$ and $\Phi_{sig} = \phi_z z$ we can write the set of equations of motion in the following form

$$\begin{cases} \Phi_{cal} + \phi_z a + L_{tot}I = 0 \\ z = \frac{\phi_z I}{m(-\omega^2 + \frac{i\omega_0}{Q}\omega + \omega_o{}^2)}. \end{cases} \tag{5.14}$$

These equations can be solved for $z(\omega)$ and $I(\omega)$

$$\begin{cases} z(\omega) = -\dfrac{\phi_z \Phi_{cal}}{mL_{tot}(-\omega^2 + i\frac{\omega_0}{Q}\omega + \omega_0^2 + \frac{\phi_z^2}{mL_{tot}})} \\[3mm] I(\omega) = -\dfrac{\Phi_{cal}}{L_{tot}(1 + \frac{\phi_z^2}{mL_{tot}(-\omega^2 + i\frac{\omega_0}{Q}\omega + \omega_0^2)})} \end{cases} \tag{5.15}$$

where $I_{cal} = \frac{\Phi_{cal}}{L_{tot}}$ is the current in the input loop due to the calibration flux. From the first equation we see that the cantilever response to the calibration signal is Lorentzian with the coupling to the detection coil introducing frequency shift due to an additional magnetic spring constant. It can be easily shown that for high Q and a small relative change of the resonant frequency, the first equation corresponds to a harmonic oscillator with the resonant frequency of $\omega_0'^2 \equiv \omega_0^2 + \frac{\phi_z^2}{mL_{tot}}$ and a spring constant of $k' = k + \frac{\phi_z^2}{L_{tot}}$.

By further simplifying the second part of equation (5.15) we get an expression for frequency dependence of the current in the detection loop:

$$I(\omega) = -\frac{-\omega^2 + i\frac{\omega_0}{Q}\omega + \omega_0^2}{-\omega^2 + i\frac{\omega_0'}{Q}\omega + \omega_0'^2} I_{cal} \tag{5.16}$$

Similar to what we did in section 4.2.1, we can define a coupling factor β as

$$\beta^2 = \frac{\omega_0^2 - \omega_0'^2}{\omega_0'^2} \equiv \frac{\phi_z^2}{k'L_{tot}} \tag{5.17}$$

Since we can experimentally measure only a coupled resonant frequency ω', we write down the final expression for the current as

$$I(\omega) = -\frac{-\omega^2 + i\frac{\omega_0'}{Q}\omega + \omega_0'^2(1 - \beta^2)}{-\omega^2 + i\frac{\omega'_0}{Q}\omega + \omega_0'^2} I_{cal} \tag{5.18}$$

Now, we can determine the coupling factor β^2 and thus ϕ_z by accurately measuring the calibration transfer function $I(\omega)$ vs ϕ_{cal} with the lock-in amplifier and fitting with equation (5.18). An interesting point is that the factor β^2 affects only the shape of the transfer function, in particular it is related with the difference between resonance and antiresonance frequencies in equation (5.18). Thus, the estimation of β^2 is completely unaffected by any uncertainty on the absolute value of the calibration flux Φ_{cal}, the SQUID gain or the total loop inductance value L_{tot}. One can also show that $1 - \beta^2$ is the ratio of the values of the transfer function well below and well above the resonance frequency, and that, in the limit of small β^2 and high Q, the ratio between maximum and minimum of the module of the transfer function is given by $1 + \beta^2 Q$.

The calibration curves for the first two normal modes of the cantilever are shown on figure 5.11.
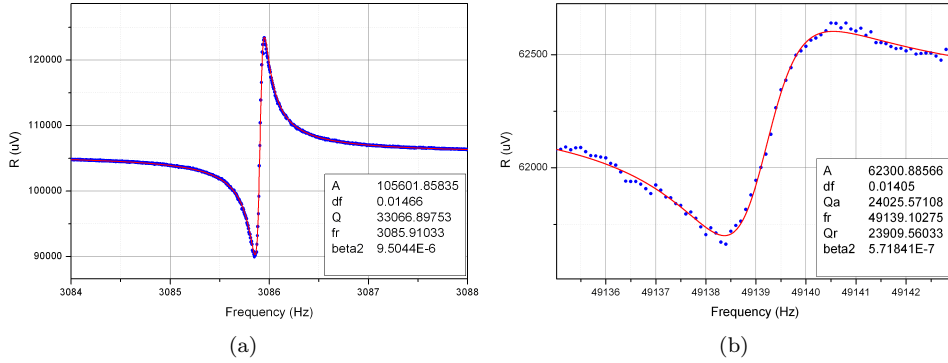
Figure 5.11: Calibration of cantilever-SQUID coupling for the first two fundamental modes of the cantilever.

5.5.2   Thermal Noise

After we have measured the coupling, we can estimate the equivalent temperature T_{eq} of the cantilever vibration mode. If it is only excited by the thermal noise then the cantilever displacement with the variance of

$$\langle z_{th}^2 \rangle = \frac{4K_B T_{eq}}{k'} \tag{5.19}$$

would result in a current in the detection loop which is given by

$$\langle I_{th}^2 \rangle = \frac{\phi_z^2}{L_{tot}^2}\langle z_{th}^2 \rangle = \frac{\phi_z^2 4K_B T_{eq}}{k' L_{tot}^2} = \beta^2 \frac{4K_B T_{eq}}{L_{tot}} \tag{5.20}$$

The voltage noise on the output of the SQUID is:

$$S_V = M^2 \langle I_{th}^2 \rangle V_\Phi^2 = 4K_b \frac{M^2}{L_{tot}}\beta^2 V_\Phi^2 T_{eq} \equiv A T_{eq}, \tag{5.21}$$

where V_F is the flux gain of the SQUID and $A \equiv 4K_b \frac{M^2}{L_{tot}}\beta^2 V_\Phi^2$ is a conversion factor from the equivalent temperature of the mode to a voltage at the output of the SQUID. The equivalent temperature of the cantilever mode is not necessarily equal to the thermodynamic temperature. It can be higher if the cantilever is excited by some other noise sources, like mechanical vibration.

   Note that the above expressions contain the total inductance L_{tot}, which is unknown. However, we can estimate the relation $\frac{M^2}{L_{tot}}$ by measuring the thermal noise spectrum of a resistor connected in series with L_{tot}. In our case we can use the resistance of Al bonding wires in the cantilever module. Above the superconducting transition temperature of Al ($T_c \approx 1.17$ K) the bonding wires generate thermal noise, with power spectral density given by:

$$S_{vv} = 4K_bTR \tag{5.22}$$

The impedance of the series RL circuit is $Z(\omega) = R + i\omega L$, so the noise at the output of the SQUID is:

$$S_{V_{out}}(\omega) = \frac{S_{vv}}{|Z|^2}M^2V_\Phi^2 = \frac{4K_bTRM^2V_\Phi^2}{(R^2 + \omega^2L_{tot}^2)} \equiv \frac{4K_bTM^2V_\Phi^2}{R(1 + \omega^2\frac{L_{tot}^2}{R^2})} \tag{5.23}$$

The noise spectra in equation (5.23) can be fitted with a simple function:

$$S_V(f) = \frac{S_0}{1 + \frac{f^2}{f_0^2}}, \tag{5.24}$$

where $S_0 = \frac{4K_bTM^2V_\Phi^2}{\Phi_0 R}$ is the thermal noise of the resistor and $f_0 = \frac{R}{2\pi L}$ - the cutoff frequency of RL lowpass filter.

We can get the expression for $\frac{M^2}{L_{tot}}$:

$$\frac{M^2}{L} = \frac{\pi\Phi_0 S_0 f_0}{2k_bTV_\Phi^2} \tag{5.25}$$

An example of a SQUID nose spectra at $T = 1246$ mK and the fit are shown on figure 5.12

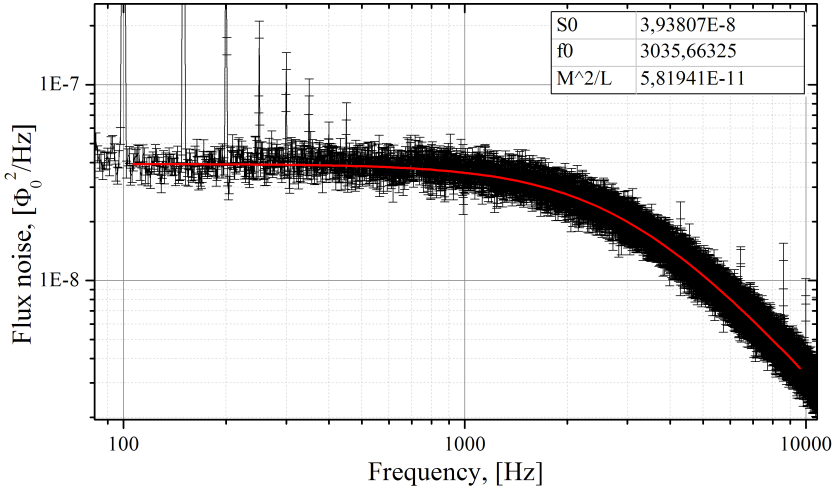| S0 | 3,93807E-8 |
| f0 | 3035,66325 |
| M^2/L | 5,81941E-11 |

Figure 5.12: Calibration of the SQUID input loop. T=1246 mK

5.6   Experimental results

We have performed a series of cooldowns (runs) in a dilution refrigerator. During these runs we were focused on reducing the vibration noise and improving the thermalization of the cantilever chip in order to improve the force sensitivity of the resonator. The cantilever and SQUID modules were placed on the second mass of vibration isolation stage. During the cooldown we have reached the minimal temperature of the mass of about 9 mK. The flux noise of our 2-stage SQUID amplifier scaled down with temperature to about 500 mK, reaching a constant level of $\sim 0.6 \ \mu\phi_0/\sqrt{\text{Hz}}$.

First, in order to determine the properties of the cantilever at low temperature, we have mechanically excited it with the small piezo oscillator in the cantilever module and measured the ringdown signal with the lock-in amplifier. We have found that we can also see the second vibrational mode of the resonator in the SQUID bandwidth.

Mode	$f_0, [Hz]$	Q	β
1.	3084	3.8×10^4	9.5×10^{-6}
2.	49150	2.3×10^4	5.7×10^{-7}

Table 5.3: Properties of first two cantilever modes at low temperature.

As we can see, the second mode has a coupling almost 20 times smaller then the first one because the cantilever position was optimized for the first mode only. However, its thermal noise was still visible in the SQUID noise spectra up to the lowest temperature.

After we have characterized the modes we have measured the effective temperature of the resonator by stabilizing the dilution refrigerator, recording its temperature with a calibrated thermometer and measuring the energy stored in the modes. The power spectral density of the SQUID output signal, featuring the Lorentzian peak due to the thermal motion of the resonator at two separate bath temperatures is shown in the right side of figure 5.13. The measured spectral density is very well fitted by a sum of the white noise of the SQUID and Lorentzian shape, indicating that the modes are likely excited by the wideband thermal noise rather than coupling to narrowband vibrational peaks.

The area of the Lorentzian peak is proportional to the mean resonator energy and can easily be converted to the effective temperature of the mode using the equation (5.21). The effective noise temperature T_N, plotted as a function of the thermal bath temperature T, is shown in the left side of figure 5.13. The difference between "Run6" and "Run8" data is in improved thermalization of the cantilever chip by means of a brass clamp. For "Run8" data a remarkable agreement between the resonator noise temperature and the bath temperature is observed at temperatures from 1 K down to about 30 mK. The noise temperature is then found to saturate at about 25 and 20 mK for the first and the second modes respectively, suggesting that some residual power dissipation, combined with the exceedingly small thermal conductance at millikelvin temperature, is limiting further cooling of the resonator.

(a) Fist mode, $f_0 = 3084$ Hz

(b) Second mode, $f_0 = 49150$ Hz
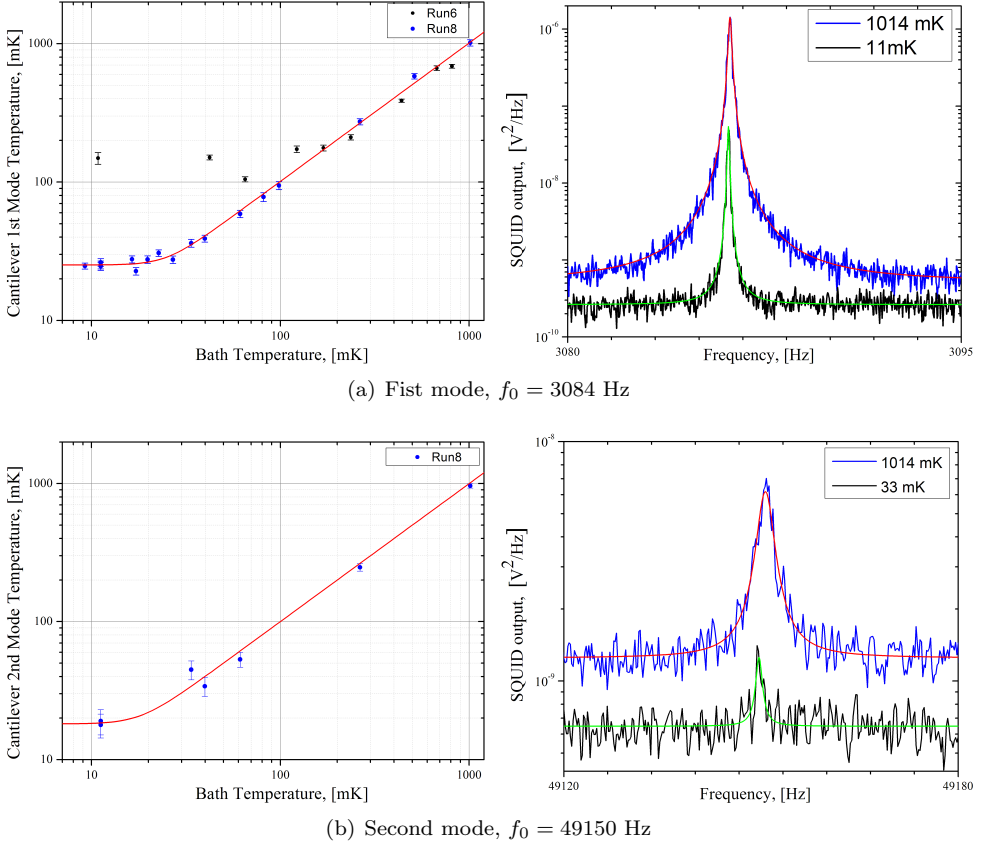
Figure 5.13: Left: effective temperature of first (a) and second (b) fundamental modes of the cantilever versus thermodynamic temperature.The continuous red line represents a fit to the data with a standard saturation curve, yielding a saturation temperature $T_{0_1} = 25 \pm 1$ mK for the first mode and $T_{0_2} = 18 \pm 3$ mK for the second one. Right: power spectral density of the SQUID output at two different bath temperatures, featuring the Lorentzian peak due to the resonator thermal motion.

The red line presents a fit to the data of the form $T_N = (T^n + T_0^n)^{1/n}$, where T_0 is the saturation temperature and the exponent n is determined [57] by the temperature dependence of the limiting thermal resistance which scales as $T^{-(n-1)}$. For the first mode the fit yields a saturation temperature $T_0 = 25 \pm 1$ mK, while the exponent $n = 5 \pm 2$ is consistent with a limiting thermal resistance due either to a boundary effect or to a 2D or 3D phonon gas [57]. For the second mode the fitted saturation temperature is $T_0 = 18 \pm 3.5$ mK, but the SNR was too low to produce any consistent result for the value of the exponent.

Assuming that the saturation is due to power dissipation in the silicon resonator, and using a simple 3D phonon model to estimate the thermal resistance through the resonator beam, we find that the residual power required to explain the observed saturation is of order 100 aW. Such power could be related with microwave dissipation in the magnetic sphere, due either to the Josephson radiation from the SQUID or to microwave thermal radiation from room temperature wiring. By means of a careful engineering of microwave filters, so far not implemented, it should be possible to suppress the residual power by several orders of magnitude, and to cool the resonator to even lower temperatures.

Regardless of the low-temperature noise saturation, the force noise amplitude spectral density can still be calculated using the fluctuation-dissipation formula $F_{min} \equiv \sqrt{S_F} = \sqrt{4k_B T_N \gamma}$, where $\gamma = k/(2\pi f_0 Q)$ is the damping constant of the resonator. In the saturation region, where $T_N = T_0$, we obtain a minimum force noise spectral density $F_{\min} = 0.51 \pm 0.03$ aN/$\sqrt{\text{Hz}}$, close to the best values ever reported in literature [81].

We can also estimate the displacement sensitivity of our detection scheme by converting the mean energy of the resonator $k_B T_N$ into mean displacement fluctuations $\langle x^2 \rangle = k_B T_N / k$. From this we infer that the experimental SQUID white noise corresponds to an equivalent displacement noise of 8 pm/$\sqrt{\text{Hz}}$. This figure is comparable with that of other techniques used with cryogenic micron-sized or nanomechanical resonators, like ultralow power interferometry [75] or quantum point contacts [83]. We note, however, that the displacement sensitivity can be greatly enhanced, by at least two orders of magnitude, by means of relatively straightforward improvements. The coupling between the magnetic particle and the detection coil can be substantially increased by reducing the size of the coil to a few microns. In this case, a possible issue could be the direct pick-up of magnetic noise due to magnetization fluctuations of the ferromagnetic particle. Furthermore, the SQUID noise can be improved at least by a factor of 2 by using either better conventional dc SQUIDs [95] or by implementing recently developed SQUID magnetometers based on non-dissipative inductive readout, exhibiting quantum limited sensitivity [96].

5.6.1   Conclusions and further experiment development

In conclusion, we have developed a SQUID-based technique suitable for detecting the displacement of a nanomechanical resonator at ultralow temperatures. By assembling a relatively simple experimental setup and cooling a silicon resonator to an effective temperature of 25 mK, we achieved a force noise spectral density of 0.51 ± 0.03 aN/$\sqrt{\text{Hz}}$. We believe that by substantially improving the experimental setup, in particular the electromagnetic shielding, the effective resonator temperature can be further reduced, possibly down to sub-millikelvin temperatures. The only fundamental limit appears to be the backaction noise of the SQUID amplifier. However, we estimate that this will not be an issue until temperatures as low as 100 μK are reached.

To illustrate the potential of the measured force sensitivity in application to

MRFM experiment, we calculate that a force of 0.03 aN is generated by a single proton spin flipping in a field gradient of 2×10^6 T/m (e.g. at 50 nm from a 1 μm diameter magnet with a magnetization of 0.75 T). While with a low force noise of only 0.1 aN/$\sqrt{\text{Hz}}$, a force from a single proton would in principle be detectable in an averaging time of less than 10 seconds, the current force sensitivities of MRFM are limited by non-contact friction. We hope that the fact that our force sensor allows operation at much lower temperatures can help to find ways to address this issue.

Our detection technique is also naturally suitable for detecting the motion of nanowire resonators, which pose even harder problems for interferometric detection due to their low reflectivity [97]. Force sensors based on ultrathin nanowires can in principle reach unprecedented force sensitivity. For example, single crystal SiC nanowires have demonstrated a damping factor as low as 4 fNm/s at room temperature [91], which would yield a force noise spectral density below 0.1 aN/$\sqrt{\text{Hz}}$ at 10 mK.

There is, however, an obvious limitation on the strength of magnetic fields used in the experiment to be lower than the critical field of the superconducting detection coil. For the thin film Nb coils we use, this means a maximal field of $\sim$ 200 mT can be applied. In fact this value is close to the magnetic field on the surface of the magnetic particle attached to the mechanical resonator. This, however, need not preclude the low field magnetic resonance imaging experiments. We also note that the SQUID itself is spatially separated from the detection coil and is not affected by the externally applied magnetic field.

The future development of this experiment is quite straightforward. A new detection coil with sensitivity optimized geometry and integrated rf line has been designed and made [98], allowing to generate an rf field for magnetic resonance experiments. A 3D scanning stage for spacial spin imaging is also being developed.

A first MRFM experiment, utilizing a SQUID detection scheme, a new detection coil and a vertical scanning stage is reported in [99]. We have found a clear evidence of cantilever coupling to paramagnetic spin system, located at $Si - SiO_2$ boundary of the detection coil substrate.

Bibliography

[1] Hulse, R. A. The discovery of the binary pulsar. *Rev. Mod. Phys.* **66**, 699–710 (1994).

[2] Taylor, J. H. Binary pulsars and relativistic gravity. *Rev. Mod. Phys.* **66**, 711–719 (1994).

[3] Weber, J. Gravitational radiation. *Phys. Rev. Lett.* **18**(13), 498–501, Mar (1967).

[4] Weber, J. Gravitational radiation experiments. *Phys. Rev. Lett.* **24**(6), 276–279, Feb (1970).

[5] Sigg, D. and the LIGO collaboration. Proc. of the 5th Edoardo Amaldi Conf. on Gravitational Waves (Pisa, Italy 5-12 July 2003). *Class. Quantum Grav.* **21**, S409–S416 (2004).

[6] Acernese, F. et al. Proc. of the 5th Edoardo Amaldi Conf. on Gravitational Waves (Pisa, Italy 5-12 July 2003). *Class. Quantum Grav.* **21**, S385–S394 (2004).

[7] Willke, B. et al. proc. of the 5th edoardo amaldi conf. on gravitational waves (pisa, italy 5-12 july 2003). *Class. Quantum Grav.* **21**, S417–S423 (2004).

[8] Takahashi, R. and the TAMA collaboration. Proc. of the 5th Edoardo Amaldi Conf. on Gravitational Waves (Pisa, Italy 5-12 July 2003). *Class. Quantum Grav.* **21**, S403–S408 (2004).

[9] Conti, L. and the AURIGA collaboration. The AURIGA second scientific run and the dual detector of gravitational waves. *Nucl. Instrum. Methods* **A 518**, 236–239 (2004).

[10] Aguiar, O. D. et al. proc. of the 5th edoardo amaldi conf. on gravitational waves (pisa, italy 5-12 july 2003). *Class. Quantum Grav.* **21**, S457–S463 (2004).

[11] de Waard, A. et al. proc. of the 5th edoardo amaldi conf. on gravitational waves (pisa, italy 5-12 july 2003). *Class. Quantum Grav.* **21**, S465–S471 (2004).

[12] Coccia, E. Proc. of the International Conference on Gravitational Waves: Sources and Detectors, 201. World Scientific, Singapore (1996).

[13] Johnson, W. W. and Merkowitz, S. M. Truncated icosahedral gravitational wave antenna. *Phys. Rev. Lett.* **70**, 2367 (1993).

[14] Forward, R. L. Multidirectional, multipolarization antennas for scalar and tensor gravitational radiation. *Gen. Relat. Gravit.* **2**(2), 149 (1971).

[15] Jr, R. M. M., Magalhaes, N. S., Aguiar, O. D., and Frajuca, C. Response of spherical gravitational wave antenna modes to high-energy cosmic ray particles. *Class. Quantum Grav.* **19**(7), 1955 (2002).

[16] Maggiore, M. *Gravitational Waves: Theory and experiments*. Gravitational Waves. Oxford University Press, (2007).

[17] Hartle, J. *Gravity: An Introduction to Einstein's General Relativity*. Addison-Wesley, Boston, (2003).

[18] Thorne, K. S. Gravitational radiation. In *Three Hundred Years of Gravitation*, 330–458. S.W. Hawking and W. Israel, Cambridge University Press,Cambridge (1987).

[19] Merkowitz, S. M. *Truncated icosahedral gravitational wave antenna*. PhD thesis, Louisiana State University, Louisiana, USA, (1995).

[20] Merkowitz, S. M. and Johnson, W. W. Spherical gravitational wave antennas and the truncated icosahedral arrangement. *Phys. Rev. D* **51**, 2546 (1995).

[21] Merkowitz, S. M. Techniques for detecting gravitational waves with a spherical antenna. *Phys. Rev. D* **56**, 7513 (1997).

[22] Merkowitz, S. M. Solution to the inverse problem for a noisy spherical gravitational wave antenna. *Phys. Rev. D* **58**, 062002–1 (1998).

[23] Gottardi, L. Complete model of a spherical gravitational wave detector with capacitive transducers: Calibration and sensitivity optimization. *Phys. Rev. D* **75**(2), 022002, Jan (2007).

[24] Misner, C. W., Thorne, K. S., and Wheeler, J. *Gravitation*. W. H. Freeman, San Francisco, (1973).

[25] Gottardi, L. *Transducers and low noise two-stage SQUID amplifiers for the spherical gravitational wave antenna MiniGRAIL*. PhD thesis, Leiden University, (2004).

[26] Tesche, C. D. and Clarke, J. DC SQUID: Noise and optimization. *J. Low Temp. Phys.* **29**, 301 (1977).

[27] Lobo, J. A. and Serrano, M. A. *Europhys. Lett.* **35**, 253 (1996).

[28] Dubath, F., Extermann, J., and Gottardi, L. On the sensitivity of a hollow sphere as a multi-modal resonant gravitational wave detector. *Class. Quantum Grav.* **24**(9), 2231 (2007).

[29] Stevenson, T. R. Limits on the sensitivity of spherical gravitational wave detectors and on the accuracy of reconstructed signals. *Phys. Rev. D* **56**(2), 564–587, Jul (1997).

[30] Zhou, C. Z. and Michelson, P. F. Spherical resonant-mass gravitational wave detectors. *Phys. Rev. D* **51**, 2517 (1995).

[31] Costa, C. F. D. S. *Data Analysis Pipeline For The Spherical Gravitational Wave Antenna MiniGRAIL*. PhD thesis, University of Geneva, (2010).

[32] Foffa, S. and Sturani, R. The coherent detection method of gravitational wave bursts for spherical antennas. *Class. Quantum Grav.* **26**(10), 105013 (2009).

[33] Pro/ENGINEER, http://www.ptc.com/.

[34] MATLAB, http://www.mathworks.com/products/matlab/.

[35] de Waard, A. *Minigrail. The first spherical gravitational wave antenna.* PhD thesis, Leiden University, Leiden, The Netherlands, (2003).

[36] de Waard, A., Frossati, G., Zendri, J. P., Coccia, E., and Fafone, V. New technique to measure the mechanical quality factor of metals using spherical samples. *Physica B* **280**, 535 (2000).

[37] Gottardi, L., de Waard, A., and Frossati, G. Two-stage SQUID systems and transducers development for MiniGRAIL. *Class. Quantum Grav.* **21**, S1191–S1196 (2004).

[38] Frossati, G. et al. present status of miniGRAIL. In *Proceedings of the 10th Marcell Grossmann Meeting on General relativity.* Rio de Janeiro, Brazil (2003).

[39] Benzaim, Y. *Mechanical attenuation system for MiniGRAIL.* graduation thesis, Universiteit Leiden, unpublished, (2004).

[40] Foffa, S. and Sturani, R. Event trigger generator for resonant spherical detectors of gravitational waves. *Class. Quantum Grav.* **25**(18), 184036 (10pp) (2008).

[41] National Instruments LabView, http://www.ni.com/labview/.

[42] STAR Cryoelectronics, 25-A Bisbee Court,Santa Fe, NM 87508-1412.

[43] http://www.hisparc.nl.

[44] Josephson, B. D. Possible new effects in superconductive tunneling. *Phys. Lett.* **1**, 251–253 (1962).

[45] Chesca, B., Kleiner, R., and Koelle, D. Squid theory. In *The SQUID Handbook*. J. Clarke and A.I. Braginski Eds., Wiley-VCH,Weinheim, Germany.

[46] Ketchen, M. B. dc SQUIDs 1980: The state of the art. *IEEE Trans. Magn.* **17**, 387 (1981).

[47] Jin, I., Amar, A., Stevenson, T. R., Wellstood, F. C., Morse, A., and Johnson, W. W. A 35 $\hbar$ two-stage SQUID system for gravity wave detection. *IEEE Trans. Appl. Supercond.* **7**, 2742–2746 (1997).

[48] Podt, M. *Wideband low-noise integrated SQUID systems*. PhD thesis, University of Twente, Enschede, The Netherlands, (2003).

[49] Schreier, R. and Temes, G. *Understanding delta-sigma data converters*. IEEE Press, (2005).

[50] http://rsync.samba.org.

[51] Paik, H. J. Superconducting tunable-diaphragm transducer for sensitive acceleration measurements. *J. Appl. Phys.* **47**, 1168 (1976).

[52] Jaszczuk, W., ter Brake, H. J. M., Flokstra, J., Veldhuis, D., Stammis, R., and Rogalla, H. Bonding of a niobium wire to a niobium thin film. *Meas. Sci. Technol.* **2**(11), 1121–1122 (1991).

[53] IPHT Jena e.V., Department of Quantum Electronics, Postfach 100239, 07702 Jena, Germany.

[54] Leiden Cryogenics B.V., Galgewater 21, 2311 VZ Leiden, The Netherlands.

[55] Pleikies, J. *Strongly coupled, low noise DC-SQUID amplifiers*. PhD thesis, University of Twente, Enschede, (2009).

[56] Quantum Design, 11578 Sorrento Valley Road, Suite 30, San Diego, CA 92121.

[57] Pobell, F. *Matter and Methods at Low Temperatures*. Springer, Berlin, 3rd ed. edition, (2002).

[58] Kanskar, M. and Wybourne, M. N. Crossover between dissipative and nondissipative electron transport in metal wires. *Phys. Rev. Lett.* **73**(15), 2123–2126, Oct (1994).

[59] Zhong, Y. L. and Lin, J. J. Observation of a linear mean-free-path dependence of the electron-phonon scattering rate in thick AuPd films. *Phys. Rev. Lett.* **80**(3), 588–591, Jan (1998).

[60] Pleikies, J., Usenko, O., Stolz, R., Fritzsch, L., Frossati, G., and Flokstra, J. Hot-electron effect in PdAu thin-film resistors with attached cooling fins. *Supercond. Sci. Tech.* **22**(11), 114007 (2009).

[61] Frossati, G. *PhD Thesis*. PhD thesis, University of Grenoble, Grenoble, France, (1978).

[62] Buraschi, M. I., Pignatel, G. U., and Sanguinetti, S. Low-temperature conductivity behaviour of ion implanted silicon bolometers. *J. Phys.: Condens. Matter* **2**(50), 10011 (1990).

[63] Quaranta, O., Spathis, P., Beltram, F., and Giazotto, F. Cooling electrons from 1 to 0.4 k with v-based nanorefrigerators. *Appl. Phys. Lett.* **98**(3), 032501 (2011).

[64] Stevenson, T. R. and Haucke, H. J. Behavior of a dc squid tightly coupled to a high- Q resonant transducer. In *Proc. of the 1st Edoardo Amaldi Conf. on Gravitational Waves*, 390. World Scientific, Singapore (1995).

[65] Vinante, A. *Optimization of a two-stage dc SQUID for resonant gravitational wave detectors*. PhD thesis, University of Trento, Trento, Italy, (2002).

[66] Falferi, P., Bonaldi, M., Cerdonio, M., Vinante, A., Mezzena, R., Prodi, G. A., and Vitale, S. $27\hbar$ squid amplifier operating with high-q resonant input load. *Appl. Phys. Lett.* **88**(6), 062505 (2006).

[67] Baggio, L., Bignotto, M., Bonaldi, M., Cerdonio, M., Conti, L., Falferi, P., Liguori, N., Marin, A., Mezzena, R., Ortolan, A., Poggi, S., Prodi, G. A., Salemi, F., Soranzo, G., Taffarello, L., Vedovato, G., Vinante, A., Vitale, S., and Zendri, J. P. 3-mode detection for widening the bandwidth of resonant gravitational wave detectors. *Phys. Rev. Lett.* **94**(24), 241101, Jun (2005).

[68] Giffard, R. P. Ultimate sensitivity limit of a resonant gravitational wave antenna using a linear motion detector. *Phys. Rev. D* **14**, 2478 (1976).

[69] Baggio, L., Cerdonio, M., Ortolan, A., Vedovato, G., Taffarello, L., Zendri, J.-P., Bonaldi, M., Falferi, P., Martinucci, V., Mezzena, R., Prodi, G. A., and Vitale, S. χ^2 testing of optimal filters for gravitational wave signals: An experimental implementation. *Phys. Rev. D* **61**(10), 102001, Apr (2000).

[70] Bonifazi, P., Ferrari, V., Frasca, S., Pallottino, G. V., and Pizzella, G. Data Analysis Algorithms for gravitational wave experiments. *Il Nuovo Cimento* **1C-6**, 465 (1978).

[71] Michelson, P. F. and Taber, R. C. Sensitivity analysis of a resonant mass gravitational wave antenna with resonant transducer. *J. Appl. Phys.* **52**, 4313 (1981).

[72] Vinante, A. and the AURIGA Collaboration. Present performance and future upgrades of the auriga capacitive readout. *Class. Quantum Grav.* **23**(8), S103 (2006).

[73] Degen, C. L., Poggio, M., Mamin, H. J., Rettner, C. T., and Rugar, D. Nanoscale magnetic resonance imaging. *Proceedings of the National Academy of Sciences* **106**(5), 1313–1317 (2009).

[74] Kleckner, D., Pikovski, I., Jeffrey, E., Ament, L., Eliel, E., van den Brink, J., and Bouwmeester, D. Creating and verifying a quantum superposition in a micro-optomechanical system. *New J. Phys.* **10**(9), 095020 (2008).

[75] Mamin, H. J. and Rugar, D. Sub-attonewton force detection at millikelvin temperatures. *Appl. Phys. Lett.* **79**(20), 3358–3360 (2001).

[76] Stipe, B. C., Mamin, H. J., Stowe, T. D., Kenny, T. W., and Rugar, D. Noncontact friction and force fluctuations between closely spaced bodies. *Phys. Rev. Lett.* **87**(9), 096801, Aug (2001).

[77] Kuehn, S., Loring, R. F., and Marohn, J. A. Dielectric fluctuations and the origins of noncontact friction. *Phys. Rev. Lett.* **96**(15), 156103 (2006).

[78] Kuehn, S., Marohn, J. A., and Loring, R. F. Noncontact dielectric friction. *J. Phys. Chem. B* **110**(30), 14525–14528 (2006).

[79] LaHaye, M. D., Buu, O., Camarota, B., and Schwab, K. C. Approaching the quantum limit of a nanomechanical resonator. *Science* **304**(5667), 74–77 (2004).

[80] Regal, C. A., Teufel, J. D., and Lehnert, K. W. Measuring nanomechanical motion with a microwave cavity interferometer. *Nat. Phys.* **4**(7), 555–560, July (2008).

[81] Teufel, J., Donner, T., Castellanos-Beltran, M., Harlow, J., and Lehnert, K. Nanomechanical motion measured with an imprecision below that at the standard quantum limit. *Nat. Nanotechnol.* **4**(12), 820–823 (2009).

[82] Rocheleau, T., Ndukum, T., Macklin, C., Hertzberg, J., Clerk, A., and Schwab, K. Preparation and detection of a mechanical resonator near the ground state of motion. *Nature* **463**(7277), 72–75 (2009).

[83] Poggio, M., Jura, M., Degen, C., Topinka, M., Mamin, H., Goldhaber-Gordon, D., and Rugar, D. An off-board quantum point contact as a sensitive detector of cantilever motion. *Nat. Phys.* **4**(8), 635–638 (2008).

[84] Ciobanu, L., Seeber, D. A., and Pennington, C. H. 3d mr microscopy with resolution 3.7 μm by 3.3 μm by 3.3 μm. *Journal of Magnetic Resonance* **158**(1-2), 178 – 182 (2002).

[85] Tyszka, J. M., Fraser, S. E., and Jacobs, R. E. Magnetic resonance microscopy: recent advances and applications. *Curr. Opin. Biotech.* **16**(1), 93 – 99 (2005). Analytical biotechnology.

[86] Blank, A., Suhovoy, E., Halevy, R., Shtirberg, L., and Harneit, W. Esr imaging in solid phase down to sub-micron resolution: methodology and applications. *Phys. Chem. Chem. Phys.* **11**, 6689–6699 (2009).

[87] Rugar, D., Budakian, R., Mamin, H. J., and Chui, B. W. Single spin detection by magnetic resonance force microscopy. *Nature* **430**, 329–332, July (2004).

[88] Mamin, H. J., Budakian, R., Chui, B. W., and Rugar, D. Detection and manipulation of statistical polarization in small spin ensembles. *Phys. Rev. Lett.* **91**(20), 207604, Nov (2003).

[89] Gysin, U., Rast, S., Ruff, P., Meyer, E., Lee, D. W., Vettiger, P., and Gerber, C. Temperature dependence of the force sensitivity of silicon cantilevers. *Phys. Rev. B* **69**, 045403, Jan (2004).

[90] Uhlig, K. 3he/4he dilution refrigerator with pulse-tube refrigerator precooling. *Cryogenics* **42**(2), 73 – 77 (2002).

[91] Perisanu, S., Vincent, P., Ayari, A., Choueib, M., Purcell, S., Bechelany, M., and Cornu, D. High q factor for mechanical resonances of batch-fabricated sic nanowires. *Appl. Phys. Lett.* **90**, 043113 (2007).

[92] Chui, B., Hishinuma, Y., Budakian, R., Mamin, H., Kenny, T., and Rugar, D. Mass-loaded cantilevers with suppressed higher-order modes for magnetic resonance force microscopy. In *TRANSDUCERS, Solid-State Sensors, Actuators and Microsystems, 12th International Conference on, 2003*, volume 2, 1120–1123. IEEE, (2003).

[93] Heeres, E., Katan, A., van Es, M., Beker, A., Hesselberth, M., van Der Zalm, D., and Oosterkamp, T. A compact multipurpose nanomanipulator for use inside a scanning electron microscope. *Rev. Sci. Instrum.* **81**, 023704 (2010).

[94] Heemskerk, P. *Cantilever Displacement Detection with a SQUID.* graduation thesis, Universiteit Leiden, unpublished, (2009).

[95] Falferi, P., Bonaldi, M., Cerdonio, M., Mezzena, R., Prodi, G., Vinante, A., and Vitale, S. 10 [h-bar] superconducting quantum interference device amplifier for acoustic gravitational wave detectors. *Appl. Phys. Lett.* **93**(17), 172506–172506 (2008).

[96] Vijay, R., Devoret, M., and Siddiqi, I. Invited review article: The josephson bifurcation amplifier. *Rev. Sci. Instrum.* **80**, 111101 (2009).

[97] Nichol, J., Hemesath, E., Lauhon, L., and Budakian, R. Displacement detection of silicon nanowires by polarization-enhanced fiber-optic interferometry. *Appl. Phys. Lett.* **93**(19), 193110–193110 (2008).

[98] Schinkelshoek, L. graduation thesis, Universiteit Leiden, unpublished, (2011).

[99] Vinante, A., Wijts, G., Schinkelshoek, L., Usenko, O., and Oosterkamp, T. Magnetic resonance force microscopy of paramagnetic electron spins at millikelvin-temperatures. *Nat. Commun.* **2**, 572– (2011).

Samenvatting

De zwakte van de zwaartekracht maakt de detectie van gravitatiegolven een van de meest uitdagende taken van de experimentele fysica. Terwijl deze golven bijna een eeuw geleden werden voorspeld door de algemene relativiteitstheorie van Einstein, zijn ze nog niet direct gemeten, ondanks de dramatische verbetering van de detector gevoeligheid. Tot nu toe werd alleen indirect bewijs van het bestaan van gravitatiegolven gevonden door waarneming van de binaire pulsar $PSR\,1913+16$ door Hulse en Taylor [1, 2]. De mate van vertraging van de rotatie van de pulsar komt exact overeen met de door de algemene relativiteitstheorie voorspelde waarde ten gevolge van emissie van gravitatiegolven.

Maar de zwakte van de interactie met de materie maakt de gravitatiegolven juist erg interessant voor astrofysici. Nauwelijks geabsorbeerd door materie laten ze de fysici kijken naar gebeurtenissen, die niet waarneembaar zijn met behulp van detectoren van elektromagnetische golven.

De geschiedenis van gravitatiegolf-detectoren telt meer dan 45 jaar van ontwikkeling. De eerste antenne werd gebouwd door Joseph Weber in 1965 [3]. Het was een anderhalf ton zware cilindrische staaf van aluminium, opgehangen in vacuum. Deze staaf had een mechanische resonantiefrequentie van $1,6\,kHz$. In 1968 bouwde hij een tweede detector om coïncidentie-metingen te kunnen doen. Door het gebruik van piezo-elektrische transducers heeft hij een vervormingsgevoeligheid $\frac{\Delta h}{h}$ van ongeveer 10^{-16} kunnen bereiken. Hoewel hij de meting van een coïncidentie-signaal tussen twee detectoren heeft gemeld [4], was de amplitude van dat signaal ver boven het verwachte niveau voor de gravitatiegolven, en werd deze door de resultaten van andere groepen ook niet bevestigd.

De huidige generatie van detectoren is ongeveer zes ordes van grootte gevoeliger, maar is desondanks nog steeds niet in staat om de detectie van een gravitatiegolf signaal te melden.

Alle op dit moment bestaande gravitatiegolfdetectoren zijn gebaseerd op twee principes:

Het eerste type zijn zogenoemde interferometrische detectoren: LIGO, bestaande uit twee interferometers - LIGO Hanford en LIGO Livingston (USA) [5], VIRGO in Cascina (Italië) [6], GEO600 in Hannover (Duitsland) [7] en TAMA300 in Japan [8].

Een ander type is de resonante detector waaronder: (i) cilindrische detectoren: AURIGA in Legnaro (Italië) [9], NAUTILUS in Frascati (Italië) en (ii) twee bolvormige

detectoren: Mario Schenberg in Brazilie [10] en MiniGRAIL [11] in Leiden.

In dit werk richten we ons alleen op het laatste type van detectoren, en op MiniGRAIL in het bijzonder.

Alle resonante detectoren zijn op soortgelijke wijze ontworpen. Het gevoelige deel van zo een resonante detector is een cilindervormige of bolvormige massa met hoge mechanische kwaliteitsfactor (in de orde van 10^6). Deze is mechanisch goed geisoleerd van geluidsbronnen in de omgeving (seismische, akoestische, elektrische, enz.). De inwendige thermische ruis van de detector wordt omlaag gebracht door bij lage temperaturen te werken. Een gravitatiegolf die door zo een detector heen gaat, drijft de quadrupool resonante modi van de resonerende massa aan. Om deze beweging te kunnen detecteren, is aan de grote massa een tweede, veel lichtere, mechanische oscillator (transducer) bevestigd. De resonantie frequentie van de transducer wordt aangepast aan die van de te detecteren trillingmodus van de detector massa. Deze transducer is dan elektrisch gekoppeld met een extern uitlees circuit.

Een bolvormige gravitatie golf detector heeft veel onderscheidende functies. Een aantal van hen deelt hij met de staafvormige antennes (prijs, compactheid, onderhoudskosten, detectie principe), maar sommige zijn echt uniek: in tegenstelling tot de staafvormige detectoren, is de bol even gevoelig voor een gravitatiegolf vanuit welke richting dan ook. Het is ook mogelijk de polarisatie van de gravitatiegolf te bepalen. Om dezelfde hoeveelheid informatie te kunnen verkrijgen met behulp van staafvormige detectoren, moet men 5 identieke staven bouwen. Een ander voordeel van de bolvormige detector is dat, bij gelijke meetfrequentie, de bol een grotere doorsnede heeft. Een overzicht van de eigenschappen van sferische gravitatiegolfdetectoren is te vinden in [12].

Toch zijn er een aantal praktische problemen bij het gebruik van bolvormige detectoren. Omnidirectionele operatie vereist het gebruik van meerdere transducers, wat de betrouwbaarheid van de detector vermindert. De kalibratie en data analyse van de bolvormige antenne is ook gecompliceerder. Om dit probleem op te lossen hebben Johnson en Merkowitz een speciale configuratie - *"truncated icosahedral gravitational wave antenna"*(TIGA) voorgesteld. De zes transducers zijn geplaatst op de 6 vijfhoekige vlakken van een afgeknot icosahedron. Door de hoge symmetrie konden ze een eenvoudige algoritme voor reconstructie van het gravitatiegolf signaal van de vaste combinaties van transducer-uitgangen ontwikkelen.

Dit proefschrift is gericht op het bouwen van een volledig data-acquisitie systeem, en de voorbereiding van MiniGRAIL voor een meeting, met 6 transducers bij een temperatuur in het milliKelvin gebied. Het proefschrift is als volgt opgebouwd:

In hoofdstuk 1 geven we een algemene inleiding in de fysica van gravitatiegolven, en de principes van gravitatiegolf-detectie. Het overzicht is gericht op de eigenschappen van resonante bolvormige detectoren en de MiniGRAIL opstelling in het bijzonder. Hoofdstuk 2 gaat over de ontwikkeling van het MiniGRAIL data-acquisitie systeem. Hoofdstuk 3 beschrijft verbeteringen in de opstelling die gemaakt zijn op basis van de resultaten van voorgaande experimenten. In hoofdstuk 4 worden de resultaten van de eerste kalibratie-run van MiniGRAIL gepresenteerd. Een toepassing van een gevoelige tweetraps SQUID versterker, ontwikkeld voor MiniGRAIL, in een magnetische reso-

nantie kracht-microscopie (MRFM) experiment wordt beschreven in hoofdstuk 5.

List of Publications

1. A. Vinante, G. Wijts, L. Schinkelshoek, O. Usenko, T. Oosterkamp, "Magnetic Resonance Force Microscopy of paramagnetic electron spins at millikelvintemperatures", *Nat. Commun.*, vol. 2, p. 572, 2011.

2. O. Usenko, A. Vinante, G. Wijts, T.H. Oosterkamp, "A superconducting quantum interference device based read-out of a subattonewton force sensor operating at millikelvin temperatures", *Appl. Phys. Lett.*, vol. 98, p. 133105, 2011.

3. J. Pleikies, O. Usenko, R. Stolz, L. Fritzsch, G. Frossati, J. Flokstra, "Hot-electron effect in PdAu thin-film resistors with attached cooling fins", *Supercond. Sci. Technol.*, vol. 22, p. 114007, 2009.

4. J. Pleikies, O. Usenko, G. Frossati, J. Flokstra, "SQUID current amplifiers for sub-kelvin operation temperatures", *Cryogenics*, vol. 49, pp. 669-671, 2009.

5. J. Pleikies, O. Usenko, G. Frossati, J. Flokstra, "Optimization of a Low-Tc DC SQUID Amplifier With Tightly Coupled Input Coils", *IEEE Trans. Appl. Supercond.*, vol. 19, pp. 199-205, 2009.

6. J. Pleikies, O. Usenko, J. Flokstra, "Numerical studies on dc-SQUID sensors with tightly coupled input coil", *J. Phys.: Conf. Ser.*, vol. 97, p. 012254, 2008.

7. J. Pleikies, O. Usenko, KH Kuit, J. Flokstra, A. De Waard, G. Frossati, "SQUID developments for the gravitational wave antenna MiniGRAIL", *IEEE Trans. Appl. Supercond.*, vol. 17, pp. 764-767, 2007.

8. L. Gottardi, A. De Waard, O. Usenko, G. Frossati, M. Podt, J. Flokstra, M. Bassan, V. Fafone, Y. Minenkov, A. Rocchi, "Sensitivity of the spherical gravitational wave detector MiniGRAIL operating at 5 K", *Phys. Rev. D*, vol. 76, p. 102005, 2007.

9. A. De Waard, M. Bassan, Y. Benzaim, V. Fafone, J. Flokstra, G. Frossati, L. Gottardi, CT Herbschleb, A. Karbalai-Sadegh, K. Kuit, others, "Preparing for science run 1 of MiniGRAIL", *Class. Quantum Grav.*, vol. 23, pp. S79-S84, 2006.

10. R. Ackermann, Y. Benzaim, G. Frossati, L. Gottardi, A. Karbalai-Sadegh, W. Reincke, A. Shumack, O. Usenko, A. de Waard, J. Flokstra, M. Podt, M. Bassan, E. Coccia, V. Fafone, Y. Minenkov, A. Moleti, G. V. Pallottino, A. Rocchi, M. Visco, "Present Status of MiniGRAIL", *Proceedings of the 10th Marcel Grossmann Meeting on General Relativity*, pp. 1149-1168, 2005.

Curriculum Vitae

Oleksandr Usenko was born is Kharkiv, Ukraine (former Soviet Union) in 1980. After attending the Lyceum of Physics and Mathematics #27 from 1992 to 1997, he studied Physics at the Department of Physics and Technology of the National Technical University "Kharkiv Polytechnic Institute". He did his bachelor research project under the supervision of dr. N. Diakonenko entitled "Study of amorphous films of complex chalcogenide compounds". After that he did a master research internship in the Department of Thermal Properties of Molecular Crystals at the Institute for Low Temperature Physics and Engineering, under supervision of dr. B. Gorodilov. The title of his graduation thesis was: Phonon-rotational interaction in solid argon with nitrogen admixture. On July 1st, 2003 he graduated "cum laude" in physics with specialization in material science.

From September 2003 to September 2004 he worked on the development of a data acquisition system for gravitational wave detector MiniGRAIL at the Kammerlingh Onnes Laboratory of Leiden University, The Netherlands, in the group of Prof. Giorgio Frossati.

In September 2004 he started his PhD project in the Kamerlingh Onnes Laboratory of Leiden University, The Netherlands, under supervision of Prof. Giorgio Frossati. The work concerned the development of a low-noise SQUID-based multi-channel acquisition system that would allow full-featured operation of MiniGRAIL. He also participated in the development of the SQUID detection of the displacement of a nanomechanical resonator used for a magnetic resonance force microscopy experiment under supervision of Prof. Tjerk Oosterkamp.